

# CFD Analysis of Unsteady Hydrodynamic Loading on Horizontal Axis Tidal Turbine (HATT) Blades

By

Xue Wang

A thesis presented in fulfilment of the requirements for the degree of  
Doctor of Philosophy

Department of Naval Architecture, Ocean and Marine Engineering  
University of Strathclyde  
Glasgow, UK

November 2015



This thesis is the result of the author's original research. It has been composed by the author and has not been previously submitted for examination which has led to the award of a degree.

The copyright of this thesis belongs to the author under the terms of the United Kingdom Copyright Acts as qualified by University of Strathclyde Regulation 3.50. Due acknowledge must always be made of the use of any material contained in, or derived from, this thesis.

Signed:

Date:



# Abstract

---

Horizontal Axis Tidal Turbines (HATTs) can experience amplified, time varying hydrodynamic loads during operation due to dynamic stall. Elevated hydrodynamic loads impose high structural loads on turbine blades, thus appreciably shortening machine service life. An improved characterization of the unsteady hydrodynamic loads on tidal turbine blades is therefore necessary to enable more reliable predictions of their fatigue life and to avoid premature failures. This thesis reports on a Computational Fluid Dynamics (CFD) analysis of the unsteady blade loading of a scale-model HATT taking dynamic stall into account. Numerical simulations are performed both in two-dimensional (2-D) and three-dimensional (3-D) using the commercial CFD solver ANSYS Fluent.

After a brief description of the theories and methods involved, the behaviour of flow at low Reynolds number around a NACA-0012 aerofoil pitching in a sinusoidal pattern that induces dynamic stall is studied firstly to validate the numerical method and the choice of turbulence models. Then full 3-D computations of a rotating scale-model HATT rotor are presented for steady and periodic unsteady inflow situations, respectively. The reliability of the 3-D numerical method is evaluated by comparing the blade loads, especially the out-of-plane blade-root bending moment (defined as being about an axis normal to the rotor axis), with measurement data obtained from experimental tests conducted at the University of Strathclyde's Kelvin Hydrodynamics Laboratory towing tank. Analyses in the steady velocity study are documented for a broad range of rotor speeds and flow velocities. Furthermore, investigations of 3-D flow separation and scale effects on blade loads are also performed.

The periodic unsteady velocity study aims to examine the out-of-plane blade-root bending moment response to harmonic axial motion, deemed representative of the free-stream velocity perturbations induced by the unsteady flow. Parametric tests on oscillatory frequencies and amplitudes are carried out in order to analyse the HATT

blade hydrodynamic behaviour under different flow patterns. Detailed flow field data is analysed to understand 3-D dynamic stall from a modelling perspective.

It is concluded that the results by the present study provide significant insights into the flow physics occurring around the HATT rotor blades under various flow conditions. The CFD method can be used for designing more advanced HATT rotors, it also can be used to fine tune the computationally faster lower order Blade Element Momentum (BEM) methods for parametric design studies where experimental data is not available, particularly at the challenging rotor operating conditions involving flow separation and dynamically varying hydrodynamic behaviours.

# Acknowledgement

---

I would like to firstly express my greatest thanks to my supervisor, Professor Sandy Day for his always kindest instructions, understandings, encouragement and support during the past five years, together with the Department's financial support nurturing this research to fruition, even though there is still a long way from his expectations to making contributions to humankind. I also would like to express my greatest gratitude to Professor Atilla Incecik and Professor Chengi Kuo for their ongoing support and motivation.

I would also thank Professor Shan Huang and Dr Mahdi Khorasanchi for their kindest help throughout my study. Sincere thanks also go to Professor Jian Deng in ZheJiang University of China for his instruction and support.

I am grateful to all of my colleagues at NAOME for interesting discussions, for answering my questions and for broadening my mind. In particular I would like to mention my fellow PhD students Wei Jin, ZhiLiang Gao, ZhengQiang Xu and Li Xu,. I would also mention JianXin Hu, ZhiMing Yuan and others. It has been a pleasure working at the department.

My last but most special thanks are for my parents, my brother and my husband, for their always devoted love that built and light up my life.





# Table of Contents

---

Abstract .....	I
Acknowledgement.....	III
Table of Contents .....	V
List of Figures .....	IX
List of Tables.....	XIII
Nomenclatures.....	XV
Chapter 1 Introduction .....	1
1.1 Tidal Energy Technologies.....	1
1.2 Unsteady Blade loading of HATT.....	7
1.3 Current Research on HATT Blade Loading .....	8
1.3.1 Experimental Studies.....	9
1.3.2 Numerical Simulations .....	11
1.4 Aims and Objectives.....	14
1.5 Thesis Outline.....	15
Chapter 2 Theory.....	17
2.1 HATT Blade Hydrodynamics.....	17
2.1.1 Reynolds Number.....	17
2.1.2 Froude Number .....	18
2.1.3 Hydrodynamic Performance of Blade Elements .....	19
2.1.4 Hydrodynamic Performance of Blade .....	23
2.1.5 Scaling Effects.....	28
2.2 Dynamic Stall .....	31
2.2.1 Boundary Layer Separation.....	31
2.2.2 Static Stall .....	34
2.2.3 Dynamic Stall.....	37
2.3 CFD Turbulence Modelling.....	40
2.3.1 Introduction of CFD .....	40
2.3.2 The Governing Equations of Fluid Flow.....	42
2.3.3 Turbulence Approach.....	44

2.3.4 Near-Wall Treatments .....	49
2.3.5 Numerical Solver.....	53
2.4 Summary.....	58
Chapter 3 Case Study of 2-D Dynamic Stall .....	59
3.1 Introduction .....	59
3.2 Description of the Test Case.....	62
3.3 Numerical Methods .....	63
3.4 Results .....	68
3.4.1 Lift and Drag Force Predictions .....	68
3.4.2 Flow structure of Dynamic Stall .....	73
3.5 Summary.....	79
Chapter 4 CFD Methodology for HATT Blade Hydrodynamics Modelling.....	81
4.1 Model Turbine and Experimental Setup.....	81
4.2 Coordinates and Geometry .....	85
4.3 Computational Domain.....	87
4.4 Boundary Conditions .....	89
4.5 Grid Generation .....	90
4.6 CFD Solver Setup.....	95
4.7 Summary.....	97
Chapter 5 Methodology Validation.....	99
5.1 Grid Refinement Study .....	99
5.2 Time Step Investigation.....	105
5.3 Turbulence Models .....	106
5.4 Summary.....	107
Chapter 6 Steady Flow Study.....	109
6.1 Performance Characteristics .....	109
6.2 Investigation of Blade Stall .....	113
6.3 Investigation of Scaling Effects.....	115
6.4 Summary.....	120
Chapter 7 Periodic Unsteady Flow Study .....	121
7.1 Sensitivity to Time-Varying Velocity .....	121
7.1.1 Effect of Varying the Amplitude of Oscillation.....	122
7.1.2 Effect of Varying the Oscillatory Amplitude .....	129

7.2 Dynamic Stall Characteristics Investigation.....	134
7.2.1 Dynamic Stall Near Wall .....	134
7.2.2 Vortex Structure .....	136
7.3 Summary.....	138
Chapter 8 Conclusions and Future Work.....	141
8.1 Conclusions .....	141
8.2 Future Work.....	143
References .....	145



# List of Figures

---

Figure 1-1 Global renewables-based power capacity additions by type and share of total capacity additions (IEA, 2015) .....	1
Figure 1-2 (a) Tidal barrage at La Rance, France (b) Tidal barrage at Sihwa Lake, South Korea (Photo: IRENA (2014)).....	3
Figure 2-2 Lift/Drag ratio and coefficients vs. angles of attack ( <a href="http://www.free-online-private-pilot-ground-school.com/Aerodynamics_in_flight.html">http://www.free-online-private-pilot-ground-school.com/Aerodynamics in flight.html</a> ) .....	21
Figure 2-3 Polar curve illustrates the dependency of lift and drag on Reynolds number of a NACA 0018 airfoil (Whelan and Stallard, 2011).....	22
Figure 2-4 Power coefficient and tip-speed ratio for a variety of wind turbine configurations (Hau, 2006) .....	24
Figure 2-5 Edgewise and Flap-wise Direction at a Rotor Blade Element .....	27
Figure 2-6 Velocity distributions in a boundary layer of thickness $\delta$ close to the surface of a body ( $u_\infty$ is free stream velocity, $u$ is local velocity) (Schlichting and Gersten, 2000).....	32
Figure 2-7 Boundary layer separation on a solid surface (Sturm et al., 2012) .....	33
Figure 2-8 Reynolds number effects on laminar boundary layer subject to adverse pressure gradient (Miley, 1982). .....	34
Figure 2-9 boundary layer separation and stall on an airfoil .....	35
Figure 2-10 Three types of airfoil stall (Crimi, 1973) .....	36
Figure 2-11 Dynamic stall stages from Leishman (2000).....	38
Figure 2-12 Subdivisions of the Near-Wall Region (Fluent12.1, 2010).....	51
Figure 2-13 Near-Wall Treatments in FLUENT (Fluent 12.1, 2010).....	52
Figure 3-1 The profile of the NACA0012 Airfoil.....	63
Figure 3-2 The C-type Computational Domain (here 20c means 20 times of the chord length) .....	64
Figure 3-3 Grids distribution of the C-type grid used for URANS (a) around the airfoil (b) around leading edge (b) around the trailing edge .....	65
Figure 3-4 History of the lift coefficient for the pitching NACA0012 airofil .....	69

Figure 3-5 Comparison of the lift coefficient hysteresis loops of the pitching NACA0012 airfoil between current and previous results using various models .....	70
Figure 3-6 Comparison of the drag coefficient hysteresis loops of the pitching NACA0012 airfoil between current and previous results using various models .....	71
Figure 3-7 Pressure field superimposed on the instantaneous streamlines computed using the SST k- $\omega$ model .....	76
Figure 3-8 Pressure field superimposed on the instantaneous streamlines computed using the Transition SST model .....	77
Figure 3-9 Pressure field superimposed on the instantaneous streamlines computed using the SST k- $\omega$ based DDES model .....	78
Figure 4-1 Turbine used in experiments by Milne et al. (2013) .....	82
Figure 4-2 Schematic of the turbine and experimental test configuration .....	83
Figure 4-3 The turbine as installed, with the main and auxiliary carriages visible ...	83
Figure 4-4 Original geometry of the turbine rotor .....	86
Figure 4-5 Adjusted geometry of the turbine rotor .....	87
Figure 4-6 Computational domain for the CFD analysis .....	89
Figure 4-7 Boundary conditions and domain extents .....	90
Figure 4-8 (a) Inner-domain blocking using ANSYS ICEM (b) blocks edges around the blade .....	93
Figure 4-9 Outer-domain blocking and structured grids using ANSYS ICEM .....	94
Figure 4-10 Structured surface grid around the blade using ANSYS ICEM (a) grids around the computational geometry (b) boundary layer grids (c) grids at the blade tip (d) grids at the blade root .....	94
Figure 4-11 Wall $y^+$ calculated by ANSYS Fluent from an unsteady inflow case of the model turbine .....	95
Figure 5-1 Blade in-plane bending moment coefficient $C_{M_x}$ for steady inflow case .....	102
Figure 5-2 Blade out-of-plane bending moment coefficient $C_{M_y}$ for steady inflow case .....	102
Figure 5-3 Non-dimensional time history of the out-of-plane bending moment $C_{M_y}$ for oscillatory inflow case (operating condition: $n = 73$ rpm , $U = 0.78$ m/s , $f = 0.5$ Hz, $\mu = 0.2$ ) .....	104

Figure 5-4 Out-of-plane bending moment coefficient $C_{My}$ as a function of instantaneous tip-speed ratio for oscillatory inflow case (operating condition: $n = 73$ rpm, $U = 0.78$ m/s, $f = 0.5$ Hz, $\mu = 0.2$ ).....	104
Figure 5-5 Non-dimensional time history of the out-of-plane bending moment coefficient $C_{My}$ for oscillatory inflow case (operating condition: $n = 73$ rpm , $U = 0.78$ m/s, $f = 0.5$ Hz, $\mu = 0.2$ ) .....	106
Figure 6-1 Power coefficients as a function of tip-speed ratio for steady inflow case .....	111
Figure 6-2 Thrust coefficients as a function of tip-speed ratio for steady inflow case .....	111
Figure 6-3 In-plane bending moment coefficients as a function of tip-speed ratio for steady inflow case .....	112
Figure 6-4 Out-of-plane bending moment coefficients as a function of tip-speed ratio for steady inflow case.....	112
Figure 6-5 Visualization of the surface limiting streamlines for steady flow cases	114
Figure 6-6 Wall $y^+$ calculated by ANSYS Fluent from a steady inflow case of the full scale turbine.....	116
Figure 6-7 Power coefficients as a function of tip-speed ratio for different turbine scales .....	117
Figure 6-8 Thrust coefficients as a function of tip-speed ratio for different turbine scales .....	118
Figure 6-9 In-plane bending moment coefficients as a function of tip-speed ratio for different turbine scales .....	118
Figure 6-10 Out-of-plane bending moment coefficients as a function of tip-speed ratio for different turbine scales .....	119
Figure 6-11 Comparison of surface limiting streamlines between 5% and full scale turbine blade at the suction side .....	119
Figure 7-1 Time histories of the velocity, acceleration, and out-of-plane bending moment coefficient ( $\lambda = 3.6$ , $n = 73$ rpm, $U = 0.78$ m/s, $f = 0.5$ Hz, $\mu = 0.2$ )..	125
Figure 7-2 Time histories of the velocity, acceleration, and out-of-plane bending moment coefficient ( $\lambda = 3.6$ , $n = 73$ rpm, $U = 0.78$ m/s, $f = 0.64$ Hz, $\mu = 0.2$ )	126
Figure 7-3 Time histories of the velocity, acceleration, and out-of-plane bending moment coefficient ( $\lambda = 3.6$ , $n = 73$ rpm, $U = 0.78$ m/s, $f = 0.89$ Hz, $\mu = 0.2$ )	127

Figure 7-4 Comparison of the out-of-plane bending moment at different oscillatory frequencies .....	128
Figure 7-5 Comparison of the out-of-plane bending moment coefficients as a function of instantaneous tip-speed ratio at different oscillatory frequencies .....	128
Figure 7-6 Time histories of the velocity, acceleration, and out-of-plane bending moment coefficient ( $\lambda = 3.6$ , $n = 84$ rpm, $U = 0.89$ m/s, $f = 0.5$ Hz, $\mu = 0.1$ )..	130
Figure 7-7 Time histories of the velocity, acceleration, and out-of-plane bending moment coefficient ( $\lambda = 3.6$ , $n = 84$ rpm, $U = 0.89$ m/s, $f = 0.5$ Hz, $\mu = 0.2$ )..	131
Figure 7-8 Time histories of the velocity, acceleration, and out-of-plane bending moment coefficient ( $\lambda = 3.6$ , $n = 84$ rpm, $U = 0.89$ m/s, $f = 0.5$ Hz, $\mu = 0.3$ )..	132
Figure 7-9 Comparison of the out-of-plane bending moment at different current numbers .....	133
Figure 7-10 The selected flow visualization points for the case of $f=0.5$ , $\lambda=3.6$ , $\mu=0.2$ , $U=0.78$ m/s, $n=73$ rpm .....	133
Figure 7-11 Visualization of the limiting streamlines during one oscillating cycle	135
Figure 7-12 Iso-surface of Q-criterion during one oscillating cycle.....	137



# List of Tables

---

Table 3-1 Computational conditions .....	66
Table 3-2 Details of the CPU time required for 2-D calculations.....	67
Table 3-3 Occurrence of Lift Stall .....	72
Table 4-1 Computational Conditions .....	96
Table 5-1 Operating conditions with steady inflow .....	101
Table 5-2 The relative difference of $C_{Mx}$ to the experimental results.....	101
Table 5-3 The relative difference of $C_{My}$ to the experimental results.....	101
Table 5-4 The results from the time step study .....	105
Table 6-1 Chord based Reynolds number prediction at 0.75R using geometric scaling .....	115



# Nomenclatures

---

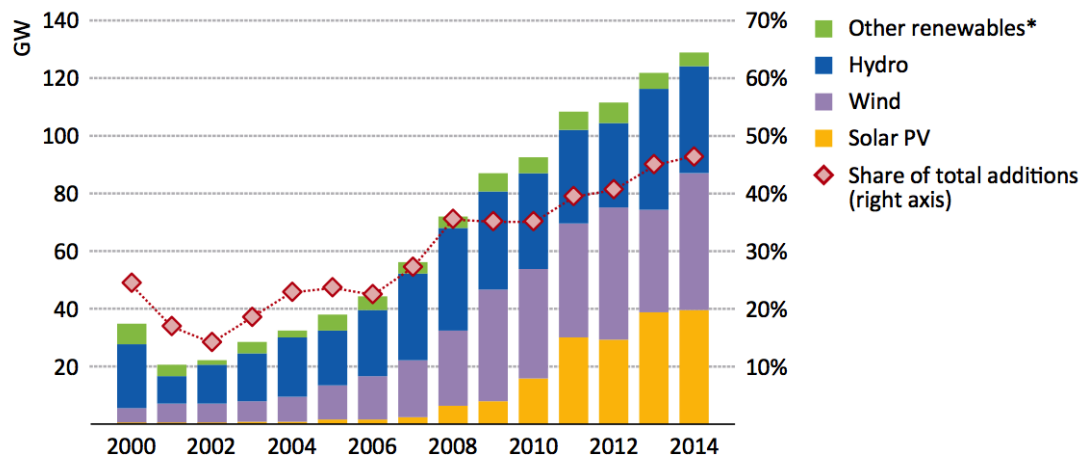
$C_{M_x}$	-	Blade root in-plane bending moment coefficient
$C_{M_y}$	-	Blade root out-of-plane bending moment coefficient
$c_D$	-	Drag Coefficient
$c_L$	-	Lift Coefficient
$C_P$	-	Power coefficient
$C_T$	-	Thrust coefficient
$F_D$	N	Drag force per unit span
$F_L$	N	Lift force per unit span
$l_\eta$	m	Length scale of the smallest eddies of turbulence
$M_x$	Nm	In-plane bending moment on a turbine blade
$M_y$	Nm	Out-of-plane bending moment on a turbine blade
$t_\eta$	$t$	Velocity scale of the smallest eddies of turbulence
$v_\eta$	m/s	Time scale of the smallest eddies of turbulence
$A$	$m^2$	Frontal area of the rotor
$c$	m	Chord length of a blade element
$E(k)$		Energy spectrum
$f$	$s^{-1}$	Frequency of rotation
$g$	$m/s^2$	Gravitational constant
$k$	-	Turbulence wavenumber
$L$	m	Characteristic linear dimension of the body
$L$	m	Characteristic dimension
$P$	kW	Power

$Q$	Nm	Torque
$R$	m	Rotor radius
$Re$	-	Reynolds number
$v$	m/s	Mean velocity of the object relative to the fluid
$V$	m/s	Characteristic velocity, free-stream velocity of the fluid
$\delta$	m	Boundary layer thickness
$\varepsilon$	J/kg · s	Dissipation rate of the smallest eddies of turbulence
$\kappa$	-	Reduced frequency
$\lambda$	-	Tip-speed ratio
$\mu$	kg/(m · s)	Dynamic viscosity of the fluid
$\nu$	m <sup>2</sup> /s	Kinematic viscosity of the fluid
$\rho$	kg/m <sup>3</sup>	Density of the fluid
$\omega$	rad/s	Angular velocity of rotation

# Chapter 1 Introduction

## 1.1 Tidal Energy Technologies

With growing concerns about the impacts of carbon emissions on the environment, the security of energy supply, the escalation of energy costs and the danger of peak oil, governments over the world are taking measures to reduce dependence on fossil fuels and diversify the energy mix. Against this background, there is widespread popular support for the development and deployment of renewable energy technologies over many years, which includes promoting the proliferation of relatively mature technologies such as nuclear plants, photovoltaic and wind turbines, as well as developing novel generation strategies. Based on the World Energy Outlook Special Report 2015 by the International Energy Agency (IEA), renewables-based power generation capacity is estimated to have increased by 128 gigawatts (GW) in 2014, of which 37% is wind power, almost one-third solar power and more than a quarter from hydropower (Figure 1-1) (IEA, 2015).



\* Includes geothermal, marine, bioenergy and concentrating solar power.

Figure 1-1 Global renewables-based power capacity additions by type and share of total capacity additions (IEA, 2015)

The oceans have great potential for harnessing energy as they cover 72% of the earth's surface. However, the contribution of ocean energy to the global energy mix is very small, with key technologies still in the development and demonstration phases. Industrial companies and research institutions have attempted, with varying success, to tap ocean energy as it occurs in offshore winds, waves, tides, marine currents, thermal gradients, and salinity gradients. Among these forms, significant benefits and opportunities have been identified in the area of tidal energy extraction.

It is well known that tides are the rise and fall of sea levels caused by the combined effects of the gravitational forces exerted by the Moon and the Sun and the rotation of the Earth. The vertical motion of the tides near the shore causes the water to move horizontally, creating tidal currents. When a tidal current moves toward the land and away from the sea, it "floods". When it moves toward the sea away from the land, it "ebbs". Both the potential energy associated with the rise and fall movement, and the kinetic energy associated with flood and ebb can be transformed into mechanical and electrical energy. As with all sources of renewable energy, tidal energy has advantages and disadvantages, but does offer a significant advantage over other sources of renewable energy, in that it is relatively predictable as the energy production is not influenced by weather conditions but rather by the cycles of the moon, sun and earth, providing a predictable bi-weekly, biannual and annual cycle. This advantage makes it less challenging to connect tidal power generation devices to existing electricity grids and more manageable when used together with other renewable sources as part of a regional generation mix.

There are several technologies for exploiting the energy of tides. Principally they are all harnessing either kinetic energy or potential energy from the tide, and converting it into electricity. As a result, tidal energy technologies can be classified into two types: tidal range technologies and tidal current technologies.

Tidal range technologies harvest the potential energy created by tidal ranges. One common model involves erecting a tidal dam, or barrage, with a sluice across a narrow bay or estuary. As the tide flows in or out, creating uneven water levels on

either side of the barrage, the sluice is opened and water flows through low-head hydro turbines for electricity generation. It has been developed on several commercial-scale projects in the past. The first tidal barrage was completed in the Rance River in the northwest of France (Brittany) in 1966 (Figure 1-2 (a)), with a capacity of 240 megawatts (MW). Between 1960s and 1970s, a number of small tidal plants were built in countries such as Canada (20 MW), China (5 MW) and Russia (0.4 MW). In 2011, tidal power of 254 MW began to be extracted from the Sihwa Lake Tidal Barrage in South Korea (Figure 1-2 (b)), which places it as the largest tidal power generation plant in the world. In the UK, a proposed tidal barrage project (the Severn barrage) has been rejected on multiple occasions, due to the potential financial, technical and environmental risks. As such, despite the technology being ready and bankable, it is unlikely that further tidal barrages will be created in Europe in the near future. Several other models for tidal range facilities have emerged in recent years, including tidal fences, shore-connected lagoons and offshore lagoons, but none are commercially operating.

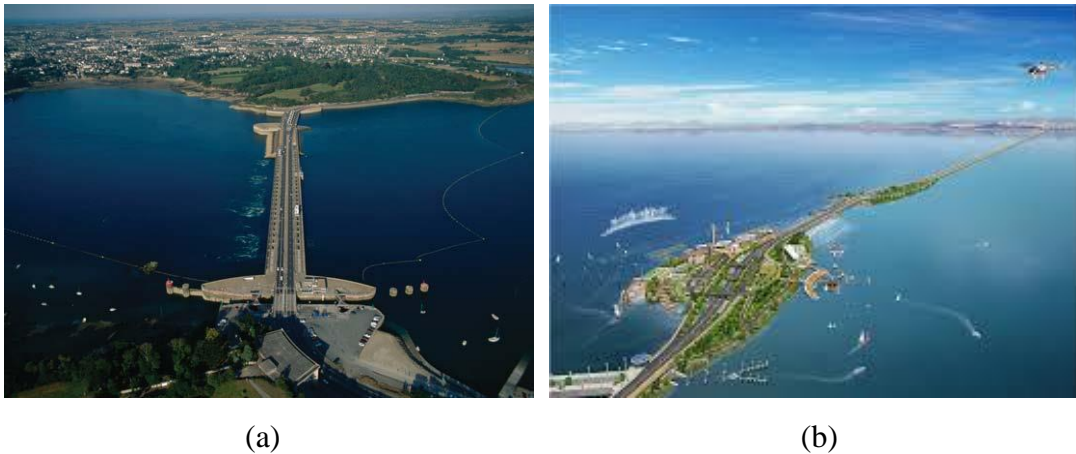


Figure 1-2 (a) Tidal barrage at La Rance, France (b) Tidal barrage at Sihwa Lake, South Korea (Photo: IRENA (2014))

Tidal current technologies usually involve mechanical device of a rotor or foil to extract the kinetic energy from the tidal flow. Compared to either barrage, they have less environmental and ecological impacts and are faster and therefore cheaper to build. In the past few years, tidal current technologies have made enormous strides in

development towards commercialisation. More than 40 new devices are introduced between the period 2006-2014, and a few of them are tested at full scale in the ocean. Following the recent report of 2014 tidal energy technology brief by the International Renewable Energy Agency (IRENA), three main categories of these devices can be distinguished on the basis of different energy conversion systems. They are Horizontal/Vertical Axis Tidal Turbines (HATT/VATT), Reciprocating devices, and other designs. Further classifications of tidal current technologies could be defined according to the type of foundations or mooring employed and on operational conditions of the device (JRC, 2014). To make efficient use of tidal regions, it is also proposed that the devices will be installed in large multi-device arrays.





A HATT or VATT basically works on the same principle as does a wind turbine (Rourke et al., 2009). The rotor blades convert the tidal current kinetic energy into the shaft mechanical energy and a generator converts this mechanical energy into electricity. However, due to the higher density of water (832 times that of air) (Bryden et al., 2004), the blades are smaller and turn more slowly than wind turbines. Furthermore, they have to withstand greater forces and movements than wind turbines. The blades of a HATT or VATT can also be enclosed within a duct. The latter turbines are referred to as Enclosed, Ducted or Shrouded turbines. Due to the enclosure, the ocean current is concentrated and streamlined so that the flow and power output from the turbines increases. Reciprocating devices have blades called hydrofoils – shaped like airplane wings – that move up and down as the tidal stream flows on either side of the blade. The up and down movement of the hydrofoils is subsequently converted into rotation to drive a rotating shaft, or connected to pistons to support a hydraulic system for power generation. The advantage of reciprocating devices is that the length of the blade is not constrained by water depth, however it also requires complex control systems to pitch the blades correctly. There are a number of other designs that are in the research and development stage, which include Venturi Device, Archimedes Screw, and Tidal Kite. The tidal current technologies are still immature and on the pilot stage, they have not been operated commercially for extended periods to establish performances and rates of return on investments.








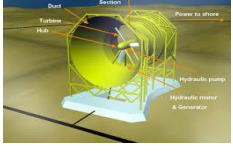




At present, horizontal axis tidal turbines represent the most common type of tidal current technologies. It was estimated that 76% of all research and development (R&D) investments into tidal current technologies went into horizontal axis turbines, 4% into enclosed turbines, and 2% into vertical axis turbines (Joint Research Centre (JRC), 2013). The most representative devices of different tidal current technologies are summarized in table 1-1.

The long-term economic potential and environmental impact of HATTs will become clearer after trials on various designs, notably in the UK, Canada, Japan, Russia, Australia, and China. The engineering challenge is to design reliable and durable equipment capable of operating for many years in a harsh marine environment with low operational and maintenance costs. More work is needed to advance this technology and bring it to commercial-scale electricity production. To make further progress into a fully-commercial phase, it will be important for developers to understand the loading acting on blades to ensure high durability and confidence in designs (McCann, 2008; Batten, 2008).

Table 1-1 Representative devices of different tidal current technologies

Developer	Device	Description	Picture
Siemens Marine Current Turbines, UK	SeaGen (S) 1.2 MW	Twin horizontal-axis rotors; Two variable-pitch blades.	 A photograph of the SeaGen (S) tidal turbine, a twin horizontal-axis design with two variable-pitch blades, mounted on a steel structure in the water.
Andritz Hydro Hammerfest, Norway/UK	HS1000 1 MW	Horizontal axis of rotation; Three-bladed design.	 A photograph of the HS1000 tidal turbine, a three-bladed horizontal-axis design, mounted on a yellow structure in the water.
Alstom Tidal Generation (TGL), UK	Oceade™18 1.4 MW	Horizontal axis of rotation; Three-bladed design.	 A photograph of the Oceade™18 tidal turbine, a three-bladed horizontal-axis design, mounted on a yellow structure in the water.
Atlantis Resources Corp, UK	AR-1000 1 MW	Horizontal axis of rotation; Three-bladed design.	 A photograph of the AR-1000 tidal turbine, a three-bladed horizontal-axis design, mounted on a blue and white structure in the water.

Voith Hydro, Germany	HyTide 1 MW	Horizontal axis of rotation; Three-bladed design.	
Scotrenewables, UK	SR2000 2 MW	Twin horizontal-axis rotors; Two blades; Flexible mooring system.	
Ponte de Archimede, Italy	Kobald 30 KW	Vertical axis of rotation; Utilizes straight blades.	
GCK Technology Ltd, USA	Gorlov Helical Turbine	Vertical axis of rotation; Utilizes twisted blades	
Engineering Business Ltd, UK	Stingray 500 KW	Reciprocating device; Utilizes a hydraulic generator.	
Pulse Generation Ltd, UK	Pulse Tidal Hydrofoil 100 KW	Reciprocating device; Utilizes a hydraulic generator.	
OpenHydro Ltd, Ireland	Open-Centre Turbine 2 MW	Open-Centre rotor and stator; Horizontal axis of rotation; Venturi Duct.	
Lunar Energy, UK	Lunar Energy Tidal Turbine 2 MW	Horizontal axis of rotation; Hydraulic motor and generator; Venturi Duct.	
Flumill, Norway	Fullmill Power Tower 4 MW	Buoyant, solid helical twin screw turbine; Four point base mount.	
Minesto, Sweden	Deep Green 500 KW	a tidal kite 'flying' in the tidal stream tethered to the seabed	

## 1.2 Unsteady Blade loading of HATT

Tidal turbines are operating in harsh environment. Unsteadiness in the onset flow plays a dominant driver of both ultimate and fatigue loads of tidal turbine blades, which arises from the phenomenon such as turbulence, surface waves, and the depth-wise variations in the mean flow. In particular, HATT blades can experience large changes in angle of attack during normal operation, which can result in impulsive loading changes over portions of the rotating blades. Characterising these loads is crucial if tidal turbines are to meet their intended service life of at least 20 years and prove to be economically competitive with other renewable energy technologies.

The unsteady hydrodynamic loads of a rotor that is subjected to an axial flow perturbation include both circulatory and non-circulatory components (Milne et al., 2013). Provided that the boundary layer remains attached to the foil at the outer sections of the blade, Leishman (2002) suggests that the circulatory forces are associated with the response of the induced velocity from a combination of vorticity contained in the shed wake at the blade element, and circulation in the trailed wake. For perturbations with frequencies relatively small in comparison to the rotational frequency of the rotor, the trailing wake component is considered to dominate and is associated with a dynamic inflow effect. These circulatory effects were first observed for helicopter rotors in the 1960s and have been discussed by researchers such as Peters et al. (1989) and Leishman (2006). The non-circulatory or added mass forces are present due to the pressure forces that are required to accelerate the fluid in the vicinity of the blade (Leishman, 2002). This forcing is independent of the presence of the rotor wake opposes the acceleration of the flow. Whelan (2010) discussed that the added mass effect is likely to be more significant for tidal turbines compared to wind turbines, as the fluid and structural densities are of the same order of magnitude.

Due to the highly unsteady operating environment, a rotating HATT can experience rapid changes in the angle of attack of blade elements, resulting in flow separation and stall in a dynamic time-dependent manner, hence is referred to as dynamic stall (McCroskey et al., 1976). Leishman (2006) discusses that dynamic stall is highly

non-linear and is typically associated with both a dynamically induced camber effect, which acts to delay trailing-edge separation, and the formation and shedding of a leading edge vortex, which induces a pressure wave over the upper surface of the airfoil and subsequently leads to larger normal forces. The dynamic stall phenomenon has long been recognized as a limiting factor in rotating blade machinery undergoing time-dependent unsteady motion (Carr, 1988). Once dynamic stall occurs on a HATT blade, separation and reattachment of the flow takes place at higher and lower effective angles of attack respectively, and results in large loads in the formation of a hysteresis loop which is detrimental to the fatigue of the blade (McCroskey, 1982; Whelan, 2010).

Analysis of the unsteady hydrodynamic characteristics is complicated due to severe separation and interferences between blades and vortex in operating process. Failures of early generation HATTs have been cited to be a consequence of a poor understanding of the magnitudes and the spectral characteristics of the unsteady hydrodynamic loads (Liu and Veitch, 2012). Therefore, the need for accurate hydrodynamic predictions associated with HATT blades is very important.

### **1.3 Current Research on HATT Blade Loading**

Research studies on HATT have undergone significant growth in the past decade. Generally, research falls into two categories (Ng, 2013). The first category is the trend of using suitable numerical models to generate marine current data for potential sites in order to estimate the availability of marine current energy. The second category is the trend of improving the performance of HATTs. Research involved in the second category encompasses the fundamental design parameters that govern the performance, the hydrodynamic response of marine currents around the turbine, the electrical components and novel designs. The growths of academic research on HATTs have played an important role in the development of the tidal energy industry. A literature review of previous researches will provide a general understanding of the progress and trends in the HATT blade load area, and give a brief outline of the methodologies that should be used within this thesis.

### 1.3.1 Experimental Studies

Experimental measurements the hydrodynamic performances of HATTs are both costly and extremely difficult, particularly when considering the operating environment and the extent of reliable data required. The vast majority of the literature has been, however, predominantly focused on characterizing the hydrodynamic loads for HATTs with the flow attached across the blades (Bahaj et al., 2007a,b; Myers and Bahaj, 2006, 2007). Unsteady blade loads, which arise from phenomenon such as turbulence, surface waves and a depth-wise variation in the mean flow, have not been well understood due to the complex unsteady hydrodynamics. Until recently, only a handful of laboratory studies have been conducted on the influence of waves on the performance of tidal turbines.

Maganga et al. (2010) acquired measurements of the mean thrust on the tower structure of a 700 mm diameter (approximately 1/30th scale) HATT in a flume, where the turbulence intensity in the flow was varied from 8% to 25%. However, the spectral characteristics of the turbulence were not reported, and it is difficult to relate these results to a full-scale turbine. Furthermore, the perturbations in the thrust were not reported and it cannot be ascertained whether any overshoots in the loading were present.

Barltrop et al. (2006) reported on experiments of a model tidal turbine towed at constant velocity in a still-water tank, where the unsteady flow was imparted from surface waves. Unlike other wave-based experiments, such as those of Galloway et al. (2010), the blade-root bending moment was specifically measured. Acquiring the bending moment response from individual blades is deemed to be more suitable for quantifying the unsteady loading. This is because the non-coherent loading imparted by the surface waves would not be uniform over all three blades and could therefore only be determined in an averaged sense from thrust measurements from the shaft or support structure. Furthermore, additional losses through the shaft bearings etc. do not have to be accounted for if blade root bending moments are measured directly. Barltrop et al. (2007) also found the hydrodynamic characteristics in long and steep waves are different. In long waves, the bending moment response compared

reasonably well with a prediction using a quasi-steady numerical Blade Element-Momentum (BEM) model with no acceleration effects included. This implies that the unsteady hydrodynamic contribution for these cases was relatively small. However, in steep waves, the BEM model underestimates the dynamic behaviour of bending moments, implying non-linear effects are important, additional dynamic effects like dynamic stall and dynamic wake are necessary to be considered for these cases.

The study by Whelan et al. (2010) involved perturbing a 300 (mm) diameter twin-bladed rotor using a towing carriage. These experiments were conducted in a flume with a steady flow and the total axial thrust was inferred from the force applied to the fixed structure that supported the rotor. It was the first investigation that attempted to establish the relative contribution of the forcing components in-phase and out-of-phase with velocity of a tidal turbine. However, as the quasi-steady loading would also appear in-phase with velocity and was not removed, quantifying the unsteady hydrodynamic contribution alone from these results is inherently complicated. Whilst the investigation showed promise, the experimental set-up was subject to not only the challenges of speed control, high blockage and background unsteadiness, but also to the presence of a low frequency wave. Therefore, it is possible that the effects of unsteadiness on the loads were inherently small at these relatively low frequencies.

In an attempt to overcome some of these shortcomings, the investigation of Milne et al. (2013, 2015) adopted the approach of superimposing an unsteady surging motion upon a steady forward speed in calm water in a towing tank. A tri-bladed turbine was used in the study, where the blockage was relatively low at approximately 5%, the rotor speed was maintained constant and the blade-root bending moments were measured. The study demonstrated that for a turbine perturbed about a tip-speed ratio near maximum power, the unsteady bending moments can be significant and 25% greater than the maximum load under steady flow. However, these large loads, which were also non-linear, were believed affected by separation of the boundary layer on the foil and dynamic stall. This complicated the identification and quantification of the contribution to the loads from the unsteady attached flow phenomena. The measurements also indicated that at higher tip-speed ratios, where no dynamic stall

was believed to be present at the outer blade sections, the response tended to be comparatively more linear. Therefore, conducting the experiments at similarly high tip-speed ratios was deemed to be more suitable for quantifying the relative contribution of the dynamic inflow (circulatory) and non-circulatory forcing to the loading in terms of an amplitude and phase, and allowing the construction of a relationship akin to a transfer function. It is also important to consider that higher tip-speed ratios conditions may also be of more interest for tidal turbines that employ active pitch control for power regulation and are less likely to experience dynamic stall.

### **1.3.2 Numerical Simulations**

In existing researches involving HATT numerical simulation, the Blade Element Momentum (BEM) theory and the Computational Fluid Dynamics (CFD) methods are the most commonly used methods for determining the performance and loadings on a HATT.

BEM theory is a classic turbine rotor analysis method that combines both blade element theory and momentum theory, originally for aircraft propellers (Glauert, 1926). A full description of the most basic BEM theory can be found in e.g. Hansen (2007). In practice, BEM theory is implemented by dividing the blades of a turbine into a number of independent elements along the span. As these elements rotate in the rotor plane, they trace out annular regions. A force and momentum balance is performed over each annulus, using the induction factor obtained via momentum theory to calculate the local angle of attack and therefore the lift and drag from knowledge of the local section characteristics. An average of the wake and upstream velocities (obtained via momentum theory) is used to calculate the resultant velocity at the rotor, from which rotor force (and torque) is obtained, and then a momentum balance is applied. This process, although iterative, is exceptionally quick on modern computers, and relatively simple to program.

Because of its simplicity, BEM theory includes some assumptions and limitations. One primary assumption is that the calculations are static. The fluid around the

aerofoil remains in equilibrium and the passing flow accelerates instantly. In practice this is not the case with the aerofoil requiring time to adjust to the changing wake resulting from a dynamic inflow (Burton et al., 2001). Another limitation comes from blade element theory, which assumes there is no span-wise flow along the blade (Moriarty and Hansen, 2005; Burton et al., 2001). This is not the case for heavily loaded rotors with large pressure gradients across the span and rotors subjected to a dynamic inflow, therefore making the theory less accurate. There is also a dependence on the availability of high quality section data, at the right Reynolds number, for the foil sections of interest (Coton et al., 2002). A further limitation is that BEM theory breaks down when the blades are subjected to large deflections outside the rotor plane. Because the theory assumes momentum is conserved in a plane parallel to the rotor, any deflection will incur aerodynamic errors (Moriarty and Hansen, 2005). Some other limitations of the original theory include no modeling of tip or hub vortex influence on the induced velocities and an inability to account for skewed inflow. Most modern BEM theory accounts for this using Prandtl's theory (Manwell et al., 2009; Moriarty and Hansen, 2005; Burton et al., 2001).

In spite of the limitations listed above, benefitting from the promising trade-off between sufficiently accurate and computationally inexpensive, BEM theory has been used extensively in the design and analysis of wind turbines for decades (Hansen et al., 2006) and is also commonly used for modelling and designing tidal turbine blades (Myers and Bahaj, 2005; Fraenkel, 2007; Batten et al., 2007, 2008; Nicholls-Lee et al., 2013; Clarke et al., 2007; Whelan, 2010).

Generally two different approaches are used to perform CFD analysis on HATTs: the parameterization approach and the turbine resolving approach (Holst, 2015).

The parameterization approach is a simplified approach based on an actuator disc concept where the rotor was represented by a disk plane that causes a uniform pressure drop as the flow goes across it (Burton, 2011). The total pressure drop that the actuator disk area exerts on the fluid is represented by a unidirectional momentum loss applied at the disk volume (Lartiga and Crawford, 2010). This



approach has the advantage of requiring a reduced grid density compared to other available numerical models for CFD simulations, thus is applicable if the detailed physics at the turbine is less important, typically if a turbine farm is about to be analysed.

The turbine solving approach is using the Navier-Stokes CFD methodology that inherently includes the effects of 3-D rotation and blade root and tip vortices, so it is of great promise to give insight into the hydrodynamic characteristics of the turbine rotor flow field, thereby enabling design optimization that can lead to low-cost yet high-energy efficiency devices. This is naturally the most complex approach since the geometry is directly implemented and hence requires grid resolution at the surface to be sufficient to capture the boundary layer and separation around the turbine, whilst also requires a very large number of grid elements and subsequently significant computational effort to capture the development of the wake in the downstream (Harrison et al., 2011). Even though the turbine solving approach is considered as one of the most challenging tasks, as the improvements of the fidelity and ease of use for CFD codes it becomes realizable to analyze the blade loads and relevant hydrodynamic performance quantitatively using this approach (Mason-Jones et al., 2012). Previous CFD researches on HATT unsteady blade loads are very rare.

McSherry et al. (2011) numerically simulated the same laboratory scale turbine of Bahaj et al. (2006) by resolving the complete blade geometry. The authors used the standard SST  $k - \omega$  model with a commercial solver to predict the mean blade loadings within 5-10% of the measurements. However, little or no wake data was reported.

Afgan et al. (2013) published a detailed CFD investigation via RANS and LES to understand the flow physics and predict the behaviour of a HATT under different operating conditions. The LES results seem to be very promising with both power and thrust coefficients predicted within 3% of the experimental measurements by Bahaj et al. (2007). Mean performance coefficients were slightly under predicted by RANS, except at the optimum tip-speed ratio. This is due to prediction of flow

separation, leading to reduced lift and drag on the blade. It was also found that the general trend of the wake is similar by both methods.

Holst (2015) performed a CFD analysis to investigate the wave-current interaction on a tidal turbine. The CFD setup was based on conditions of experiments carried out at Norwegian Marine Technology Research Institute (MARINTEK, Trondheim, Norway). The wave-current interaction was obtained by simply adding the current velocity to the water particle velocities from linear wave theory. The SST turbulence model was chosen in this study and the CFD results are found to be trustworthy with calculated values close to experimental data. In addition to the wave-induced forces, the wake characteristics and wave influence on the wake are investigated. The occurrence of dynamic stall has been mentioned but not investigated in this simulation, as the requirements of a very refined grid and a transition model are hard to meet.

## **1.4 Aims and Objectives**

The work reported in this thesis represents an attempt to add pieces of knowledge into these new research topics arisen from the current development of tidal current energy utilization. The overall aim is to develop and validate a CFD numerical model to study the unsteady blade loads and relevant dynamic stall effects of HATT blades. To this end, specific objectives include:

- To critically review state-of-the-art in the modelling of HATT blade loads with the view to identifying best practice to be used and gaps to be targeted by this research.
- To understand the general concepts involves the hydrodynamic blade loads and dynamic stall phenomenon, and consider the key factors that govern blade performance.

- To validate a 2-D CFD model to simulate the dynamic stall process of a pitching NACA0012 aerofoil, and gain an understanding of the grid and turbulence models should be used to analyse dynamic stall.
- To build 3-D CFD model to simulate unsteady HATT blade loads, compare the simulation results with experimental data, and analyse the hydrodynamic flow field.
- To provide reliable strategies for the CFD modelling of the operating HATTs.
- To offer recommendations for future research in this area.

## **1.5 Thesis Outline**

The layout of the thesis is outlined next:

Chapter 2 reviews the theories relevant to this thesis and serves as a reference for later chapters. This chapter will cover everything from the hydrodynamics on the HATT, to the CFD methods used in this thesis.

In Chapter 3 a validation case of 2-D dynamic stall is studied. The details of the complex flow development of 2D dynamic stall and the boundary layer transition have been discussed.

Chapter 4 introduces the methodology for HATT blade hydrodynamics modelling. The whole processes of numerical setup, especially the grid generation approach, are discussed in detail. Validation investigations are performed to give an impression of the accuracy of the applied methodology in Chapter 5.

The results of numerical simulation are divided into two chapters. Chapter 6 presents the steady inflow performance and non-dimensional scaling effects of the model turbine. Chapter 7 indicates the oscillatory inflow performance of the model turbine.

Chapter 8 is the conclusion of the thesis work. In this chapter some recommendations are also made for future research.

# Chapter 2 Theory

---

## 2.1 HATT Blade Hydrodynamics

### 2.1.1 Reynolds Number

Two distinctly different flow regimes exist, laminar and turbulent flow. In the laminar flow state the velocity field varies smoothly and the streamlines do not mix, but move parallel to one another. In the turbulent flow state large velocity and pressure fluctuations occur in both space and time. Reynolds (1894) first demonstrated the difference in laminar flow and turbulent flow in his experiments in the late 19<sup>th</sup> century and found whether a flow is laminar or turbulent is a function of the ratio of inertial to viscous forces, i.e. for laminar flow the fluid viscosity is large enough to damp out perturbations introduced to the flow, while for turbulent flows the inertial forces are much larger than the viscous forces. The non-dimensional Reynolds number,  $Re$ , represents this ratio of inertial to viscous forces, is given by

$$Re = \frac{\text{inertial forces}}{\text{viscous forces}} = \frac{\rho v L}{\mu} = \frac{v L}{\nu} \quad (2.1)$$

Where

- $\rho$  is the density of the fluid [ $\text{kg}/\text{m}^3$ ]
- $v$  is the mean velocity of the object relative to the fluid [ $\text{m}/\text{s}$ ]
- $L$  is the characteristic linear dimension of the body [ $\text{m}$ ]
- $\mu$  is the dynamic viscosity of the fluid [ $\text{kg}/(\text{m} \cdot \text{s})$ ]
- $\nu$  is the kinematic viscosity ( $\nu = \mu/\rho$ ) [ $\text{m}^2/\text{s}$ ]

In the case of a Newtonian fluid (one whose viscosity remains constant with shear rate) such as water (Kundo and Cohen, 2010),  $Re$  can be used to identify the point at which fluid flow undergoes a change from laminar to transition flow and from transition to turbulent flow.

## 2.1.2 Froude Number

The Froude number, denoted by  $Fr$ , is the dimensionless parameter that quantifies the ratio between gravitational and inertial forces of waves. The Froude number is given by

$$Fr = \frac{V}{\sqrt{gL}} \quad (2.2)$$

Where

- $V$  is the characteristic velocity [m/s]
- $g$  is the gravitational constant [m/s<sup>2</sup>]
- $L$  is the characteristic dimension [m]

In naval architecture the Froude number is a very significant figure used to determine the resistance of a partially submerged object moving through water, and permits the comparison of similar objects of different sizes, because the wave patterns generated are similar at the same Froude number.

Waves are incorporated into most of the HATT experiments, since the free surface effects could impact on both the performance and loading of a device and the wake structure behind the device, Froude's scaling law in combined with geometric similarity is normally considered to define the various parameters (length, time, velocity etc.) in HATT scaled experimental design (Galloway, 2013). When Froude scaling is used, the Froude numbers for both the prototype and the model are remained, this results in the following relationship

$$Fr_p = \frac{V_p}{\sqrt{gL_p}} = \frac{V_m}{\sqrt{gL_m}} = Fr_m \quad (2.3)$$

The subscripts  $p$  and  $m$  in equation 2.3 represents the prototype and the model, respectively.

## 2.1.3 Hydrodynamic Performance of Blade Elements

HATT blades have carefully selected blade elements with the shape of hydrofoils (a specialized version of the aerofoil that is manufactured to work in water). A number of parameters are used to characterize a hydrofoil, as shown in Figure 2-1. The mean camber line is the locus of points halfway between the upper and lower surface of the hydrofoil. The most forward and rearward points of the mean camber line are on the trailing and leading edges, respectively. The straight line connecting the leading and trailing edges is the chord line of the hydrofoil, and the distance from the leading to the trailing edge measured along the chord line is designated as the chord,  $c$ . A rotating turbine blade will experience a relative (or apparent) velocity, which is the vector sum of the free stream velocity and the relative flow due to blade speed. The angle of attack (angle of attack),  $\alpha$ , is defined as the angle between the relative fluid flow and the chord line.

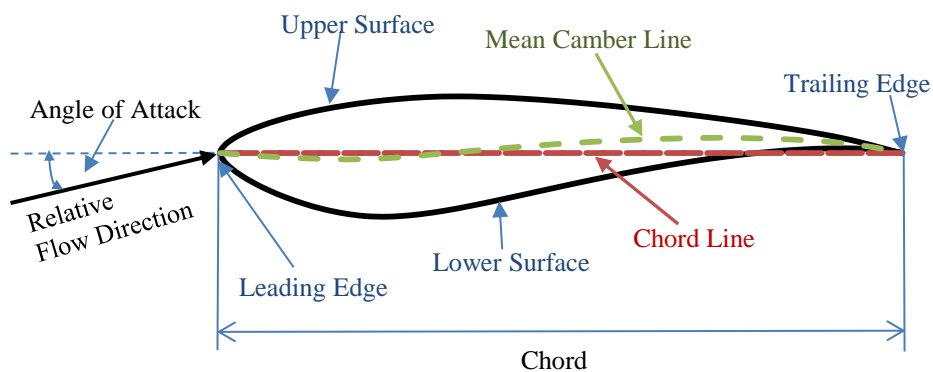


Figure 2-1 Hydrofoil nomenclature

According to Bernoulli's Principle, the passing of a fluid in the vicinity of the hydrofoil creates different velocity profiles around the hydrofoil that results in different pressure distribution. The suction (or low pressure) side of the hydrofoil is generally associated with higher velocity and lower static pressure. The pressure side of the hydrofoil has a comparatively higher dynamic pressure than the suction surface. The pressure difference between the suction and pressure side of the hydrofoil generates a lift force,  $F_l$ , which is perpendicular to the relative flow. In 2-D

flow, friction between the flow and the airfoil surface is the main reason for the drag force,  $F_d$ , which is a force parallel to the flow (Manwell et al., 2010). The lift force is typically far greater than the drag force and the result is a net movement of the turbine around the rotational axis.

2-D hydrofoil performances are usually analyzed in terms of dimensionless quantities of the section or local lift and drag coefficients, i.e. performance per unit span. The section lift coefficient  $c_l$ , and section drag coefficient  $c_d$  are respectively defined by

$$c_l = \frac{F_l}{\frac{1}{2}\rho V^2 c} \quad (2.4)$$

$$c_d = \frac{F_d}{\frac{1}{2}\rho V^2 c} \quad (2.5)$$

Where

- $F_l$  is the lift force per unit span [N/m]
- $F_d$  is the drag force per unit span [N/m]
- $\rho$  is the density of the fluid [kg/m<sup>3</sup>]
- $V$  is the free-stream velocity of the fluid [m/s]
- $c$  is the chord length of a blade element [m]

Some important parameters to describe a hydrofoil's shape are its camber and its thickness. The camber is the maximum distance between the mean camber line and the chord line, measured perpendicular to the chord line, generally expressed as a percent of the length of the chord line, such as 5% camber. The thickness is the maximum distance between the upper and lower surfaces, also measured perpendicular to the chord line and designated as a percent of chord length. A hydrofoil with zero camber is called symmetric and will generate zero lift at zero angle of attack. A cambered foil will generate positive lift at zero angle of attack with the magnitude dependent on the amount of camber. Thick hydrofoils normally



have more drag than thin hydrofoils, but when the thickness is symmetric about the camber line it has a very little effect on the lift since it affects the pressure distribution symmetrically.

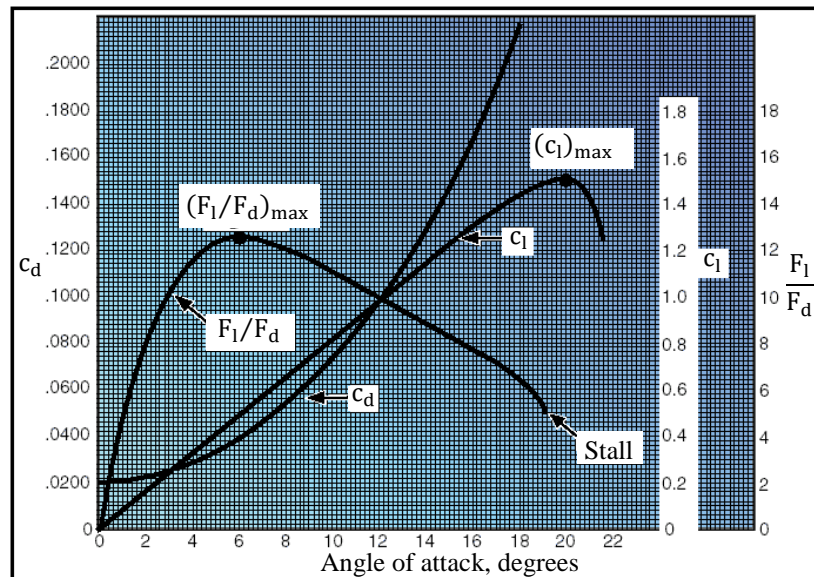


Figure 2-2 Lift/Drag ratio and coefficients vs. angles of attack ([http://www.free-online-private-pilot-ground-school.com/Aerodynamics\\_in\\_flight.html](http://www.free-online-private-pilot-ground-school.com/Aerodynamics_in_flight.html))

Just like an airplane wing, the blades of a turbine work by generating lift due to their shape. The lift force is responsible for the power yield generated by the turbine and it is therefore essential to maximize this force using appropriate design, while the drag force which opposes the motion of the blade must be minimized. It is then apparent that an aerofoil section with a high lift to drag ratio,  $F_l/F_d$  (Manwell et al., 2010) is desirable. Typical methods of presenting 2-D performance data of a lifting foil are in terms of plotting the lift coefficient, drag coefficient and lift to drag ratio as functions of the angle of attack, Figure 2-2 shows a typical example that describes the aerodynamic performance of an airplane blade element. The lift force increases as the blade is turned to present itself at a greater angle of attack. At very large angles of attack the blade “stalls” and the lift decreases. So there is an optimum angle of attack to generate the maximum lift, which is called the critical (stall) angle of attack. If the foil shape is good, the lift force is much larger than the drag. But at very high

angles of attack, especially when the blade stalls, the drag increases dramatically. So that the maximum value of the  $F_l/F_d$  ratio profile corresponds to an optimal angle of attack slightly less than the maximum lift angle for attaining the maximum efficiency of the turbine rotor blade. Stall will be discussed in detail in section 2.2.

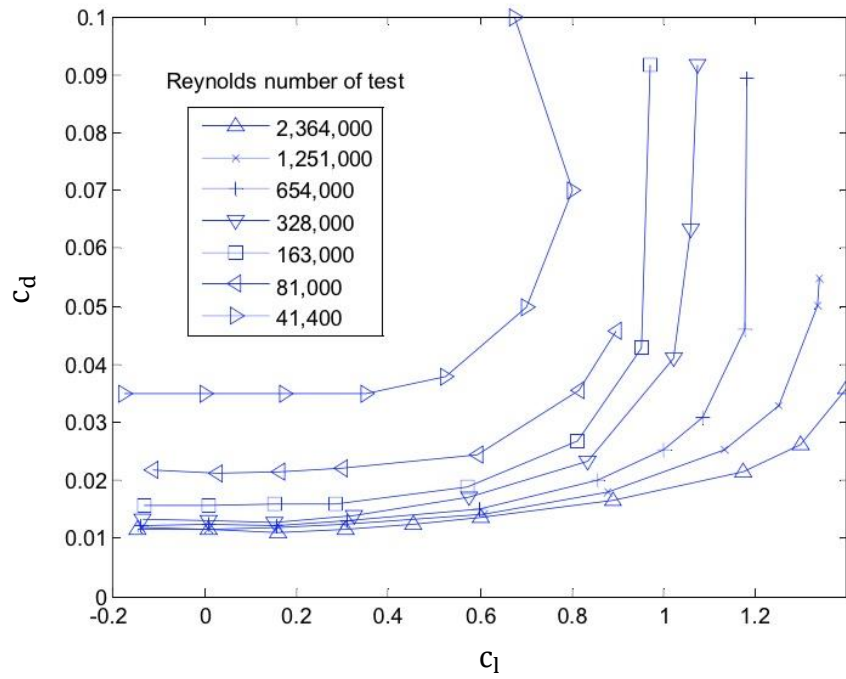


Figure 2-3 Polar curve illustrates the dependency of lift and drag on Reynolds number of a NACA 0018 airfoil (Whelan and Stallard, 2011).

The lift to drag ratio is highly dependent on the Reynolds number at which the foil is operating. Lissaman (1983) has pointed that of low Reynolds number airfoils,  $Re = 7e4$  is identified as close to transition between laminar flow and turbulent flow. Above this Reynolds number lift to drag ratio increases whereas at lower  $Re$  lift reduces and drag increases. The polar curve in Figure 2-3 illustrates the dependency of lift and drag on Reynolds number of a NACA 0018 airfoil (Whelan and Stallard, 2011). This figure clearly demonstrates the detrimental effect on the lift to drag ratio of the foil with decreasing Reynolds number and a significant jump in the lift to drag ratio as the Reynolds number increases above  $Re = 7e4$  can be clearly identified.

## 2.1.4 Hydrodynamic Performance of Blade

For an energy device, the more relevant components are the torque and thrust. The resultant of the lift and drag forces constitutes the thrust force,  $T$ , which is perpendicular to the blade rotational speed. The torque of the blade element,  $Q$ , will act at the centre of pressure which lies close to 25% of the chord length behind the leading edge, parallel to the rotational speed of the blade. The torque generates useful work, while the thrust force causes the majority of the momentum reduction in the flow (and is the dominant force when considering structural design).

Mechanical power is the most important parameter for performance evaluation of a tidal turbine blade. As previously discussed, hydrodynamic forces acting on a blade can be divided into a lift and a drag component for each blade element. Lift and drag forces move the turbine blades which convert the kinetic energy of tidal current into blade rotational energy, resulting in the hydrodynamic torque to spin a shaft that leads from the hub of the rotor to a generator. The generator turns that rotational energy into electricity that is then transferred to home power grids or utility companies for use in the usual way. Conventionally, the turbine blade performance can be analyzed in terms of dimensionless quantity of power coefficient, which is defined by

$$C_P = \frac{P}{\frac{1}{2}\rho AV^3} = \frac{Q\omega}{\frac{1}{2}\rho AV^3} \quad (2.6)$$

Where

- $P$  is the power extract from a blade [kW]
- $Q$  is the blade torque [Nm]
- $\omega$  is the angular velocity of rotation [rad/s]
- $\rho$  is the density of the fluid [kg/m<sup>3</sup>]
- $A$  is the frontal area of the rotor [m<sup>2</sup>]
- $V$  is the free-stream velocity of the fluid [m/s]

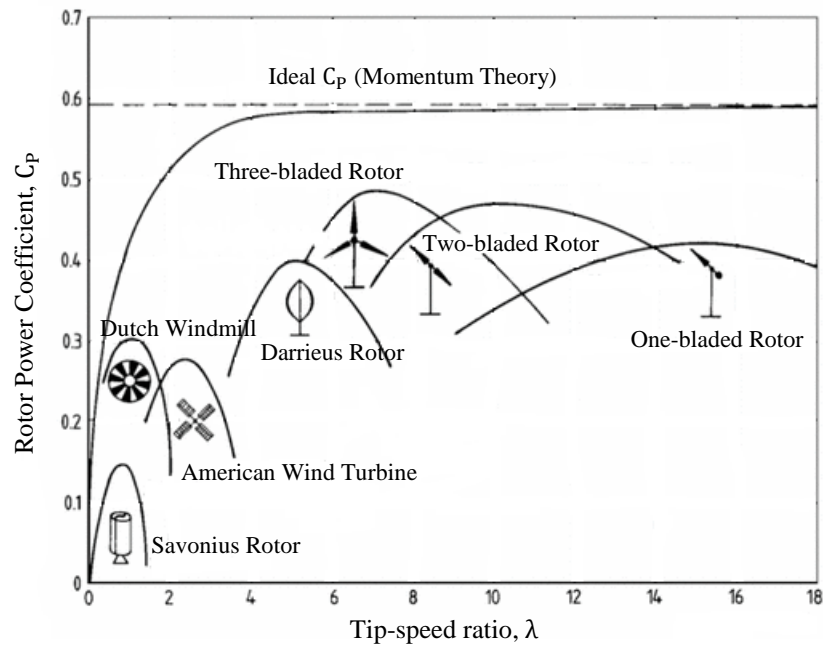


Figure 2-4 Power coefficient and tip-speed ratio for a variety of wind turbine configurations (Hau, 2006)

According to the Betz's law, the theoretical upper limit (also the Lanchester-Betz limit) on the power production from an individual wind or tidal turbine in a free stream (i.e. where the flow is uniform and the flow boundaries are far from the rotor) can be expressed as a maximum rotor power coefficient of  $16/27$ , or  $0.593$ . The Lanchester-Betz limit derived from the momentum theory, which uses conservation of mass and momentum of the fluid stream across an open flow "actuator disk". If a diffuser is used to collect additional fluid flow and direct it through the turbine, the Betz limit could be exceeded (Oman et al., 1977; Hansen et al., 2000; Jamieson, 2008). In practice, isolated turbines without ducting cannot exceed the Betz limit for several reasons, for example due to the inefficiencies and losses attributed to different configurations, rotor blades profiles, friction, and turbine designs (Manwell et al., 2010; Gasch and Twele, 2012). Practical utility-scale wind turbines achieve at peak 75% to 80% of the Betz limit (Burton, 2011). Figure 2-4 shows the ideal power coefficient for common wind turbine designs for various configurations (Hau 2006). It is apparent that the three bladed HAWTs are the most efficient with a power

coefficient of about 0.49. In reality, power coefficients in the region of 0.2-0.6 are likely for tidal turbines.

The speed at which the turbine rotates is a fundamental choice in an efficient HATT blade design. The tidal flow rotates turbine blades that ultimately result in electric power generation. The blades should be in contact with as many fluid particles as possible to achieve higher turbine efficiency. If the rotor of the turbine turns too slowly, the flow of fluid particles will pass undisturbed through the gap between the rotor blades and their kinetic energy cannot be converted to electrical energy. Alternatively if the rotor turns too fast, the blurring blades will appear like a solid wall obstructing the flow and reducing the power extraction. Therefore, it is necessary in the design of HATTs to match the angular velocity of the rotor to the fluid stream velocity in order to obtain maximum or optimal rotor efficiency.

The relationship between the rotational speed of the blade tips and the fluid stream velocity is characterized by a non-dimensional factor, known as the tip-speed ratio,  $\lambda$  (Bahaj et al., 2007). Mathematically it is expressed as

$$\lambda = \frac{\text{speed of rotor tip}}{\text{free stream velocity}} = \frac{\omega R}{V} \quad (2.7)$$

Where

- $V$  is the free-stream velocity of the fluid [m/s]
- $R$  is the rotor radius [m]
- $\omega = 2\pi f$  is the angular velocity of rotation [rad/s]
- $f$  is the frequency of rotation [ $s^{-1}$ ]

The angular velocity  $\omega$  (unit: rad/s) is determined from the rotational speed  $n$  (Revolutions per minute, abbreviated rpm) by the equation

$$\omega = \frac{2\pi n}{60} \quad (2.8)$$

The turbine efficiency is related to tip-speed ratio, with the optimum varying with turbine blade design. Higher tip speeds result in higher noise levels and require stronger blades due to large centrifugal forces.

In general a high tip-speed ratio is a desirable feature since it results in a high shaft rotational speed that is needed for the efficient operation of an electrical generator (Gasch and Tvele, 2012). However, a high tip-speed ratio poses several possible limitations such as erosion of the blade leading edges, increased noise, structural vibration and failure (Schubel and Crossley, 2012). These limitations require that turbine blades be designed with optimal tip-speed ratio, or design tip-speed ratio, where the power coefficient is a maximum. It can be noticed from Figure 2-4 that the power coefficient reaches a maximum at different tip-speed ratios for different machine designs, indicating that a unique optimal point ( $\lambda, C_p$ ) exists for each kind of turbine. This is useful for control purposes in maximizing the turbine power generation even for low speed flows.

Turbine blade loads are usually analysed in two directions, namely the flap-wise direction and the edge-wise direction. For each blade element, they are orthogonal to each other, and are characterised by the maximum and the minimum geometric moment of inertia respectively (Hau, 2006). In the 2-D blade, they set the directions of flexural vibrations: blade bending occurs about the weak and the strong principal axis in each element, which is called the flap-wise and edgewise bending respectively. For a tidal turbine, the blade flap-wise bending is mainly a result of the hydrodynamic thrust force in flap-wise direction, and the edgewise bending is mainly related to the hydrodynamic torque in edgewise direction.

When it comes to bending, a rotor blade in principle behaves like a bending beam that is clamped at one end. If all edgewise and all flap-wise acting forces have the same sign respectively throughout the rotor span, the resulting bending moments will add up towards the clamped end and become maximal at the blade root. This is generally the case for HATT operation, thus the flap-wise and edgewise bending moments at the blade root can serve as an indication for the bending load of the

whole blade. However due to the blade's twist, the axis directions change over the blade span, therefore the flap-wise and edgewise bending and deflections cannot be assigned to a fixed direction with respect to the blade root. An alternative system of directions, which is fixed for a blade, is based on the rotor plane. The according directions are the so-called out-of-plane direction and the in-plane direction. The first is a vector perpendicular to the rotor plane, while the latter is a tangential vector to the blade element's path. As Figure 2-5 shows, this system of directions differs from the flap-wise-edgewise system by the angle  $\theta^*$ , which varies with the blade radius and the pitch angle.

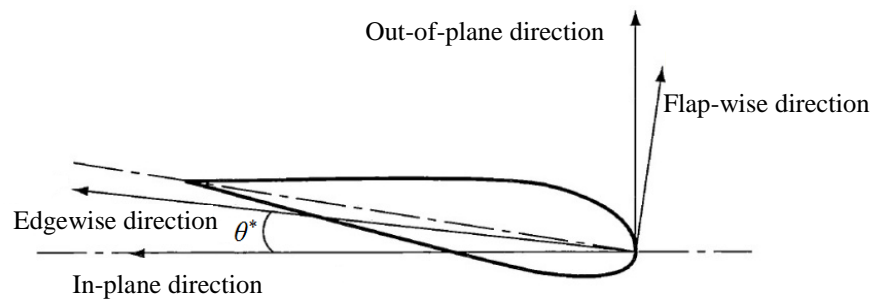


Figure 2-5 Edgewise and Flap-wise Direction at a Rotor Blade Element

The 2-D hydrodynamic forces and loads of tidal turbine blades are usually analyzed in terms of dimensionless quantities of the thrust coefficient  $C_T$ , blade root in-plane bending moment coefficient  $C_{M_x}$ , and blade root out-of-plane bending moment coefficient  $C_{M_y}$ . They are respectively defined by

$$C_T = \frac{T}{\frac{1}{2}\rho AV^2} \quad (2.9)$$

$$C_{M_x} = \frac{M_x}{\frac{1}{2}\rho AV^2 R} \quad (2.10)$$

$$C_{M_y} = \frac{M_y}{\frac{1}{2}\rho AV^2 R} \quad (2.11)$$

Where

- $T$  is the thrust force on a turbine blade [N]
- $M_x$  is the in-plane bending moment on a turbine blade [Nm]
- $M_y$  is the out-of-plane bending moment on a turbine blade [Nm]
- $A$  is the frontal area of the rotor [ $\text{m}^2$ ]
- $\rho$  is the density of the fluid [ $\text{kg}/\text{m}^3$ ]
- $V$  is the free-stream velocity of the fluid [m/s]
- $R$  is the rotor radius [m]

The edge-wise/flap-wise bending moments are often transferred to the in-plane/out-of-plane system of directions. This offers the advantage that these bending moments can more easily be related to some operating parameters of the tidal turbine blade. E.g. the blade out-of-plane bending moment leads to the thrust force while the blade in-plane bending moment is related to the torque.

## 2.1.5 Scaling Effects

The HATT technology is developing fast in recent years, different designs are being proposed and most HATT developers have tended to build large single devices, typically with a rated power of about 1 MW corresponding to a rotor of approximately 20 m diameter in a rated flow of 2.5 m/s (Starzmann et al., 2013). However, due to the high costs of developing this technology, little full-scale data exists and the unique features of each tidal location make it very difficult to assess the power performance of a HATT prior to deployment. Therefore, it is important to have reliable performance and flow field predictions based on scaled experimental tests and validated numerical simulations to reduce the cost of development.

Dimensional analysis provides scaling laws that are used to upscale model test information into performance and design information for a full-scale prototype HATT (Mason-jones et al., 2012). Drawing on the experience of the principle of



dimensional analysis in hydrodynamics, the power output  $P$  of HATT can be written as a function,  $f$

$$P = f(R, \omega, \rho, \mu, V) \quad (2.12)$$

Where

- $R$  is the characteristic diameter [m]
- $\omega$  is the angular velocity [rad/s]
- $\rho$  is the density of fluid [kg/m<sup>3</sup>]
- $\mu$  is the dynamic viscosity [kg/(m · s)]
- $V$  is the characteristic velocity [m/s]

Using the Buckingham Pi theory, the relationship between the power output and the other variables can be expressed in terms of three non-dimensional groups

$$\frac{P}{\rho R^2 V^3} = \psi_1\left(\frac{\rho V R}{\mu}, \frac{\omega R}{V}\right) \quad (2.13)$$

The parameter on the left can be expressed in a more conventional engineering format, i.e., the non-dimensional power coefficient. The first independent parameter on the right is the Reynolds number, while the second independent parameter on the right is the tip-speed ratio. Thus the non-dimensional power coefficient from the turbine should be a function of both the Reynolds number and the tip-speed ratio

$$C_p = \psi_1(Re, \lambda) \quad (2.14)$$

Similarly, the non-dimensional parameters of thrust, in-plane bending moment, and out-of-plane bending moment can also be written as functions of Reynolds number and tip-speed ratio

$$C_T = \frac{T}{\frac{1}{2} \rho A V^2} = \psi_2(Re, \lambda) \quad (2.15)$$

$$C_{M_x} = \frac{M_y}{\frac{1}{2}\rho AV^2 R} = \psi_3(Re, \lambda) \quad (2.16)$$

$$C_{M_y} = \frac{M_y}{\frac{1}{2}\rho AV^2 R} = \psi_4(Re, \lambda) \quad (2.17)$$

That is to say, if the same Reynolds number and tip-speed ratio are used in the model and the full scale, the values for  $C_p$ ,  $C_T$ ,  $C_{M_x}$  and  $C_{M_y}$  of the turbine in the full scale will be the same as that measured or predicted using the model scale. Hence hydrodynamic similitude is achieved when the Froude number, Reynolds number and the tip-speed ratio of the model and the full scale HATT are the same. However, it is well known that the Froude law and Reynolds law cannot be simultaneously satisfied (Chester et al., 1979). When Froude scaling is applied in experimental tests, due to the size constraints on realistically available tank testing facilities, the Reynolds number based on the blade chord is usually significantly reduced compared with full-scale tidal turbines. This Reynolds dissimilitude may results in a laminar flow field at model scale while the flow is fully turbulent for the full scale (Otto et al., 2012). In addition, HATTs are mostly operating at high angle of attack, flow separation occurs often especially for low Reynolds numbers. The laminar/turbulent difference between model and full-scale in combination with the presence of flow separation may have a major impact on HATT hydrodynamic performance and loading.

Numerical modelling does not necessarily suffer from scaling issues, since the model can be run at both small and full scale. Results from computational fluid dynamics (CFD) analysis can be used to both inform the development of tidal power devices when moving from smaller to larger scale, and shed light on and explain the mechanisms of fluid dynamics and device behavior observed during experimental testing. There are of course a number of phenomena that are particularly challenging to model using CFD.

## **2.2 Dynamic Stall**

In order to get a more elaborated view on dynamic stall, an introduction of boundary layer separation and static stall will be given first in this section. Understanding the theory behind dynamic stall is key in order to understand the complexity of the work in this thesis.

### **2.2.1 Boundary Layer Separation**

Because of the non-zero viscosity of real fluids, all flows feature the no-slip condition at the surface of a solid body, resulting in a boundary layer flow with high transverse velocity gradients (Sultanian, 2015). The effect of viscosity is predominantly confined to the boundary layers. Outside the boundary layer, for all practical purpose, the flow may be treated as a potential flow with negligible viscosity. As part of the boundary layer assumptions, the transverse gradient of static pressure in the boundary layer is negligible, and its gradient in the flow direction can be obtained from the Bernoulli's equation, i.e., the pressure gradient in the flow direction is essentially imposed from the outer potential flow (Schlichting, 2000; Breton, 2008). The thickness of the boundary layer is defined as the distance from the solid surface where the velocity reaches 99% of the free stream velocity. This thickness increases as the flow moves along the solid surface, as can be seen in Figure 2-6.

The fluid layer adjacent to the solid surface has to do work against surface friction at the expense of its kinetic energy. Thus the velocity of the layer goes on decreasing. Along the length of the solid surface, at a certain point a stage may come when the boundary layer may not be able to stay attached to the solid body if it does not have adequate kinetic energy to overcome the resistance offered by the solid body. In other words, the boundary layer will be separated from the surface. This phenomenon is called the boundary layer separation. The point on the body at which the boundary layer is on the verge of separation from the surface is called the point of separation.

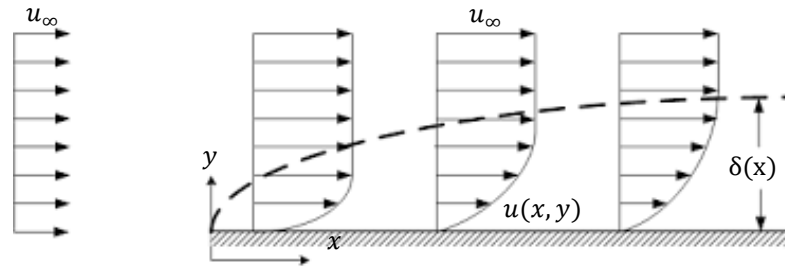


Figure 2-6 Velocity distributions in a boundary layer of thickness  $\delta$  close to the surface of a body ( $u_\infty$  is free stream velocity,  $u$  is local velocity) (Schlichting and Gersten, 2000)

The presence of the pressure gradient in the direction of flow has a significant effect on the boundary layer profile and growth. It is easy to see that the shear stress caused by viscosity has a retarding effect upon the flow. When the pressure gradient is negative, the pressure decreases in the direction of flow and the flow is accelerated. In this case, the pressure force can assist the fluid movement and there is no flow retardation. When the pressure gradient in the direction is positive, the pressure forces act opposite to the direction of flow and the flow is decelerated. In this case, the pressure force and surface friction force together try to increase the retarding effect of the viscous force. Subsequently, the thickness of the boundary layer increases rapidly in the direction of flow. Whenever such forces act over a long stretch, the forward flow is then brought to rest and further on a back flow in the pressure gradient sets in, which causes the boundary layer separation (Houghton and Carpenter, 1993). Therefore, a negative pressure gradient is said to be favorable and a positive pressure gradient is termed an adverse pressure gradient. The point of separation is determined as the limit between forward and back flow in the layer adjacent to the wall, where the wall shear stress is zero (Gad-el Hak, 2000). Figure 2-7 shows the course of events described so far.

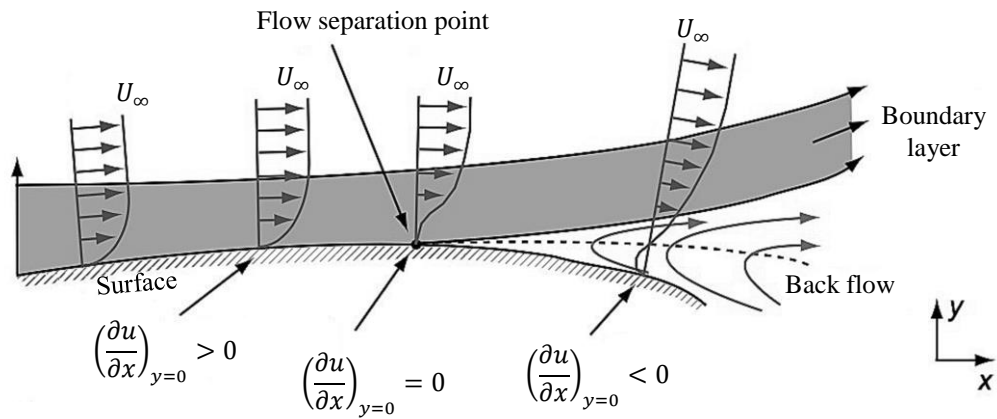
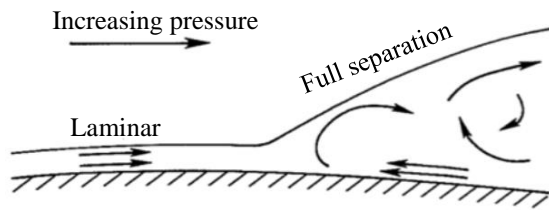
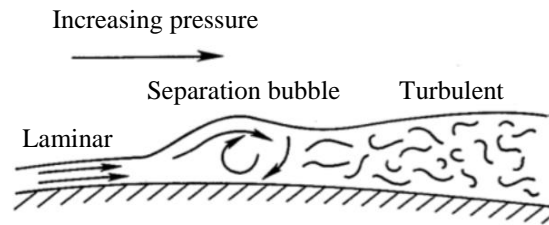


Figure 2-7 Boundary layer separation on a solid surface (Sturm et al., 2012)

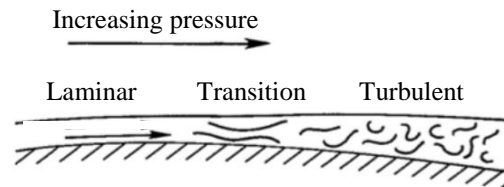
Boundary layers can be either laminar or turbulent. The laminar boundary layer is highly sensitive to separation when adverse pressure gradients are present (typically towards the trailing edge of a blade element) and is susceptible to destabilization and transition to turbulent flow. For an airfoil, depending on the Reynolds number the laminar boundary layer reacts to adverse pressure gradients in three different ways as can be seen in Figure 2-8. At low Reynolds numbers, the local curvature over the forward part of an airfoil may initiate a laminar separation when the airfoil is at a moderate angle of attack. With the increase of Reynolds number, the separated laminar boundary layer may undergo transition to turbulence with characteristic rapid thickening (Schlichting, 2000; Breton, 2008). This thickening may be sufficient for the lower edge of the now turbulent shear layer to come back into contact with the surface and reattach as a turbulent boundary layer on the surface. In this way, a Laminar Separation Bubble (LSB) of fluid is trapped under the separated shear layer between the separation and reattachment points (Houghton, 1993). When the Reynolds number is sufficiently high, the transition from laminar to turbulent occurs without the appearance of LSB. Fluid in turbulent boundary layer has appreciably more momentum than the flow of a laminar boundary layer, thus a turbulent boundary layer can penetrate further into an adverse pressure gradient without separation (Houghton, 1993).



(a) Low Reynolds numbers: full separation and stall



(b) Medium Reynolds numbers: separation and reattachment as turbulent



(c) High Reynolds numbers: transition to turbulent

Figure 2-8 Reynolds number effects on laminar boundary layer subject to adverse pressure gradient (Miley, 1982).

## 2.2.2 Static Stall

When the boundary layer separates, its displacement thickness increases sharply, which modifies the pressure field of the outside potential flow. In the case of airfoils, the pressure field modification results in an increase in pressure drag, and if severe enough will also result in loss of lift and stall, all of which are undesirable.

Stall is determined by the angle of attack. Figure 2-9 shows a typical example that illustrates the relationship between the angle of attack and boundary layer separation of an airfoil. Flow separation begins to occur at small angles of attack while attached

flow over the airfoil is still dominant. As soon as the angle of attack increases the separation point moves forward, the separated regions increase in size and hinder the airfoil's ability to create lift. At the critical angle of attack, separated flow is so dominant that further increasing in angle of attack causes rapid deterioration of the lift force, while at the same time it dramatically increases the drag, resulting in a stall.

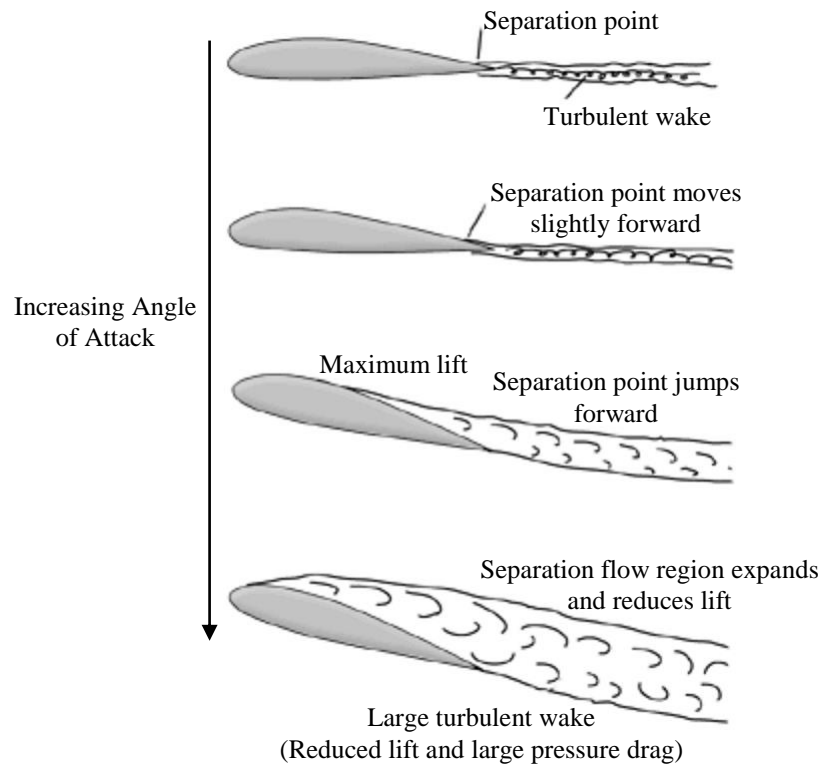


Figure 2-9 boundary layer separation and stall on an airfoil

The stall phenomenon can be divided into three forms: trailing-edge stall, leading-edge stall and thin-airfoil stall (McCullough and Gault, 1951). Figure 2-10 shows these three types of stall. Trailing-edge stall is preceded by the separation point of the turbulent boundary layer moving forward from the trailing edge with increasing angle of attack. This type of stall is characteristic of most thick aerofoil sections with thickness to chord ratios of approximately 15% and greater. Leading-edge stall has abrupt flow separation near the leading edge generally without subsequent reattachment. The abrupt separation usually results from a small laminar separation bubble that ‘bursts’ at stall and usually causes a sharp decrease in lift. This stall is generally inherent to most aerofoil sections of moderate thickness with ratios

between 9% and 15%. Thin-airfoil stall is preceded by flow separation at the leading edge with reattachment (a laminar separation bubble) at a point that moves progressively downstream with increasing angle of attack. This stall is typical on aerofoils with thickness ratios less than 9% and is generally referred to as 'long bubble bursting'. It should be point out that airfoil stall type is a function of several variables such as Reynolds number, surface roughness, or free stream turbulence. Therefore, any particular airfoil may exhibit a combination of stall types, or its stall type may change when flow conditions are changed (Broeren and Bragg, 2001).

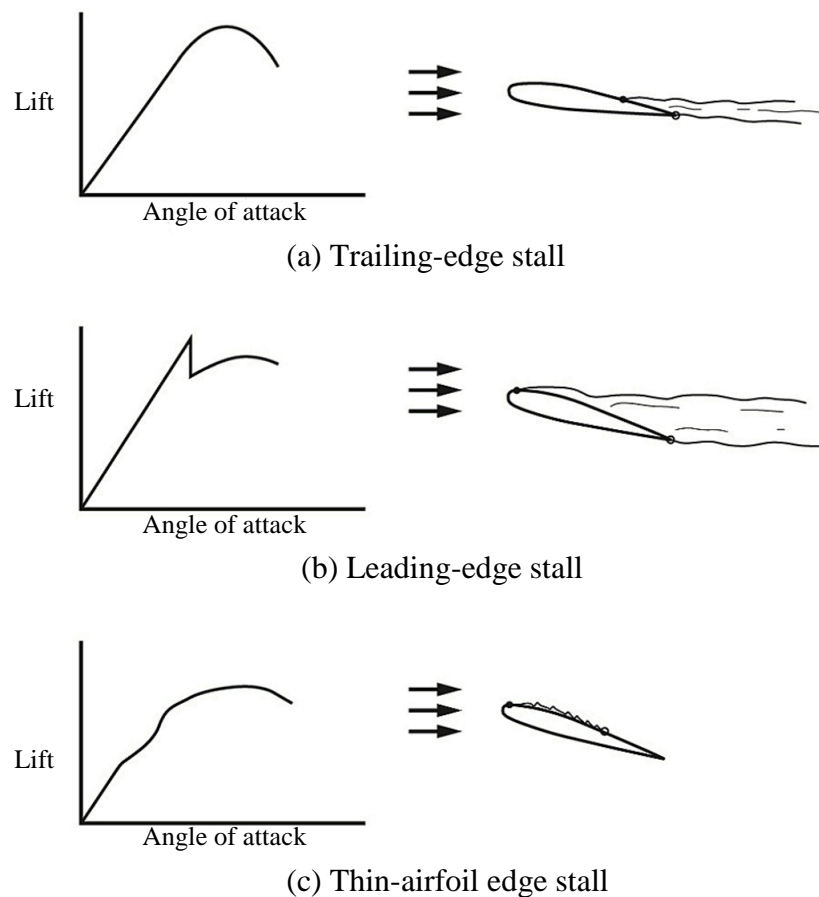


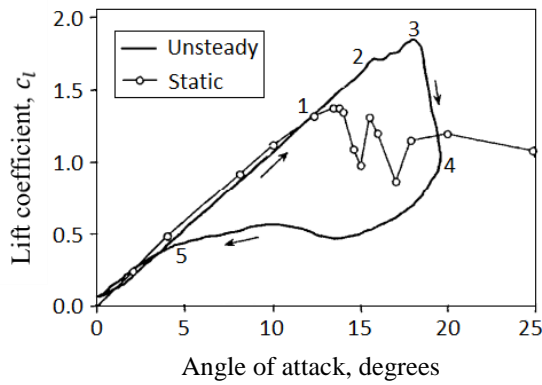
Figure 2-10 Three types of airfoil stall (Crimi, 1973)



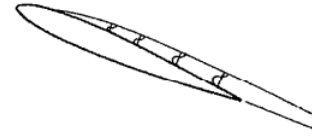
### 2.2.3 Dynamic Stall

Dynamic Stall is a significant unsteady flow problem taking place on rotary wings (e.g., helicopters and wind/tidal turbines) as the airfoils experience large variations of angle of attack (Carr 1976). The feature of dynamic stall that distinguishes it from static stall is the shedding of significant concentrated vorticity from the leading edge region. This vortex disturbance subsequently sweeps over the airfoil surface causing pressure changes and resulting in significant increases in airfoil lift and large nose-down pitching that exceeds static values (McAlister et al. 1978; McCroskey 1981; Carr 1988). A typical dynamic stall process can be categorized into five key stages, as illustrated in Figure 2-11 for an airfoil (Leishman, 2000). The overall process of dynamic stall was well described by Young (1981) and more detailed understanding of the specific events described by Young have been aided by researchers such as Galbraith et al. (1983; 1984; 1992), Carta (1960; 1979), McCroskey (1976; 1980; 1981; 1982), Carr (1977; 1995) and many more.

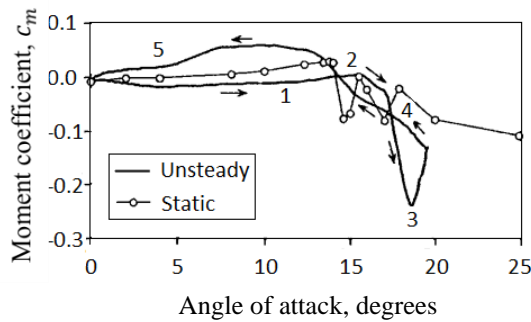
A general categorization of separating flows for oscillating airfoils, based on experimental data, is made by McCroskey and Pucci (1982) distinguishing them as having no stall, stall onset, light and deep stall. Oscillating airfoils with no stall exhibit no appreciable viscous-inviscid interaction. To distinguish stall onset, it is observed that the magnitude of the viscous-inviscid interaction for this type can increase rapidly with small increase in the maximum angle of attack, and the extent of the separation can decrease or disappear with increase in frequency. Light stall means an extensive portion of the airfoil is separated over a significant part of the cycle with reversal of the lift hysteresis in the higher angle of attack region. Deep stall involves break up and shedding of large vortex structures usually extending over a major portion of the oscillation cycle. Transition from light to deep stall typically involves the incipient break up of a large contiguous separation and emergence of isolated vortices.



Stage 1: Airfoil exceeds static stall angle, flow reversals take place in boundary layer.



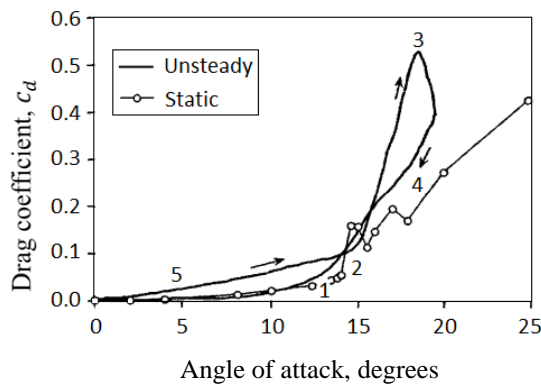
Stage 2: Flow separation at the leading edge, formation of a 'spilled' vortex. Moment stall.



Stage 2-3: Vortex convects over chord, induces extra lift and aft centre of pressure movement.



Stage 3-4: Lift stall. After vortex reaches trailing edge, flow progresses to a state of full separation.



Stage 5: When angle of attack becomes low enough, flow reattaches to back.

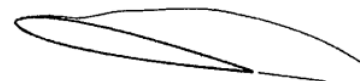


Figure 2-11 Dynamic stall stages from Leishman (2000)

Reduced frequency is considered to be the most important dimensionless parameter affecting dynamic stall on an airfoil since it incorporates the pitch rate, the chord length and the free-stream velocity into a single parameter, as well as defines the degree of unsteadiness in a flow or forcing term (McCroskey et al., 1982; Brydges,

1989; Leishman, 1990). The reduced frequency is denoted by the letter ‘ $\kappa$ ’ and given by the expression

$$\kappa = \frac{\omega c}{2U} \quad (2.18)$$

Where

- $\omega$  is the angular frequency of oscillatory changes [rad/s]
- $c$  is the chord length of a blade element [m]
- $U$  is the free-stream velocity of the fluid [m/s]

According to Leishman (2006), one can consider that if  $\kappa = 0$ , the flow is steady; if  $\kappa < 0.05$  the problem is quasi-steady, i.e. the unsteady effects are generally small and can be neglected; if a problem is characterized by a reduced frequency  $0.05 < \kappa \leq 0.2$ , it is considered unsteady, and the unsteady terms in the equations cannot be neglected if a realistic analysis is to be conducted. Moreover, if we have  $\kappa > 0.2$ , the unsteady terms will begin to dominate the behaviour of the dynamic loads, and consequentially the problem is highly unsteady.

The reduced frequency can be interpreted as the ratio between the convective time scale  $c/U$  and the time scale of the force oscillation  $1/\omega$ . It is thus easy to understand that as one increases the reduced frequency, the system will have “less time” to adapt to the changes, or in other words, it takes longer until it “becomes aware” of the changes in angle of attack, and thus the vortex shedding is delayed, as well as the reattachment. Leishman (2006) has also indicated that by further increasing the reduced frequency, it is even possible to prevent flow separation from initiating in any point of the cycle.

It should be noted that the dynamic stall flow is inherently a 2-D phenomenon, because there are significant differences between 2-D airfoil flow and 2-D flow on a rotating blade particularly for the innermost part of the blade. Rotation was found to have a delaying effect on the occurrence of separation. Lift coefficients attained at the inboard sections of a rotating blade will significantly in excess of the maximum

value possible in 2-D static test, which is why this 2-D rotational effect is usually termed as rotational augmentation, or more commonly, stall delay. Therefore, any modelling and analysis techniques involving dynamic stall should be 2-D.

## **2.3 CFD Turbulence Modelling**

### **2.3.1 Introduction of CFD**

The physical aspects of any fluid flow are governed by three fundamental principles:

- a) Mass is conserved;
- b) Momentum is conserved (Newton's second law);
- c) Energy is conserved.

All of these principles can be expressed using basic mathematical equations, which are generally in the form of integral equations or partial differential equations, and for those equations, analytical solutions are unavailable. Computational Fluid Dynamics (CFD) replaces the integrals or the partial derivatives in these equations with discretized algebraic forms, which in turn are solved to obtain numbers for the flow field values at discrete points in time and/or space (Anderson, 1995). In short, CFD is a numerical technique to solve and analyse the fluid flow problem with the aid of computers. Therefore, development of CFD is closely linked with the evolution of modern computers. The accuracy of CFD solutions that can be achieved and the details of fluid flow that can be modelled are very much dependent on advances in computer hardware, particular related to CPU speed and storage capacity. CFD methods can provide an insight into the sophisticated fluid flow phenomena in the area where the experimental instruments have difficulty in reaching, for example the blood flow in human arteries. CFD methods can also be used to give predictions before physical experiments in order to save costs and improve efficiency. Because of those advantages, nowadays CFD is widely applied in nearly all disciplines where fluid flow is important and has been viewed as a 'third-approach' to the study of

fluid dynamics, complementing the other two conventional methods: pure theory or pure experiment.

There are three main stages enclosed in every CFD simulation process: pre-processing, solver and post-processing (Versteeg and Malalasekera, 2007).

- **Pre-processing**

In this phase the physical problem is implemented into the mathematical model. The computational domain is now defined. Then, it is divided into a certain number of elements, which constitute the mesh or grid. The fluid properties and the boundary conditions are set. Since the CFD solution of a fluid dynamic problem is given locally, for well-defined positions within computational grid, the global accuracy strongly depends on the total number of mesh elements. The mesh quality is a prerequisite for obtaining the reasonably physical solutions and it is a function of the skill of the simulation engineer. A rule-of-thumb says the larger is the number of elements, the better is the solution accuracy, even though CPU effort and the total time of convergence will be higher as well. Consequently, the optimal grid should not be uniform, but finer where higher are the variables gradients and coarser in the region characterized by smooth changes in the flow. The final success of a CFD simulation strongly depends on the pre-processing and therefore a special attention might be paid to the choice of the mesh and of boundary conditions. There are different popular Pre-Processing software available in the market including: Pointwise, CFD-GEOM, ANSYS Meshing, ANSYS ICEM CFD, ANSYS Fluent Gambit, ANSYS TGrid etc.

- **Solver**

The numerical solution algorithm is the core of a CFD code. All the main CFD solvers work with the following procedure:

- a) Modelling the problem unknowns by means of simple analytical functions.
- b) Discretising the governing equations for the fluid flows, properly modified by substituting the former mentioned functions.
- c) Solving the algebraic system of equations.

Most of the commercial CFD codes (e.g., ANSYS Fluent, ANSYS CFX, STAR-CD etc.) are based on a Finite Volume (FV) discretization. The integration phase distinguishes between FV methods and other numerical techniques. By integrating the governing equations, a new set of equations even now exact is obtained, which states the conservation of the fundamental properties for each of the cells (finite control volumes) within the computational domain.

- **Post-processing**

Under this definition we include the analysis of solution results. The solver output is a set of solution variables, associated to the given grid nodes or volumes. These data must be collected, elaborated in the most suitable way (e.g., contour plots, vector plot, streamlines, data curve etc.) for the analysis, in order to produce a physical representation of the solution. Some of the popular post-processing softwares include: ANSYS CFD-Post, EnSight, FieldView, ParaView, Tecplot 360 etc.

Detailed explanations of CFD will be described in the following sub-sections. In this thesis, the commercial software ANSYS ICEM is used as the preprocessor, ANSYS Fluent is used as the CFD solver, and Tecplot is used as the post-processor. As the flow field around a HATT is highly turbulent, the using of appropriate turbulence models must be carefully considered.

### **2.3.2 The Governing Equations of Fluid Flow**

The cornerstone of CFD is the fundamental governing equations of fluid dynamics that are derived from conservation laws of mass, momentum and energy (Anderson,

2009). These equations for viscous flow are usually summarised under the term of “Navier-Stokes equations”. In the present problem heat transfer is negligible and the flow can be regarded as incompressible. Hence, the equation for energy conservation does not need to be solved, reducing the problem to the solution of the mass and momentum conservation equations.

The mass conservation equation, also called the continuity equation, is a mathematical representation of the law of conservation of mass, and can be stated as: ‘In a given volume of fluid, the rate of increase of mass inside that volume must be equal to the net rate of flow of mass into that volume across its face’. The momentum conservation equation is a statement of Newton’s second law when applied to a fluid element and can be stated as: ‘The rate of change of momentum of a fluid particle equals the sum of the forces on the particle’. In the momentum equations it is common to highlight the contributions due to surface forces as separate terms, while including the effects of body forces as source terms (Versteeg and Malalasekera, 2007).

The continuity and momentum equations for an incompressible Newtonian fluid can be written in equation (2.24) and (2.25) respectively by the following equivalent forms:

$$\nabla(\vec{u}) = 0 \Leftrightarrow \frac{\partial u_i}{\partial x_i} = 0 \Leftrightarrow \frac{\partial u}{\partial x} + \frac{\partial v}{\partial y} + \frac{\partial w}{\partial z} = 0 \quad (2.19)$$

$$\rho \left( \frac{\partial \vec{u}}{\partial t} + (\vec{u} \cdot \nabla) \vec{u} \right) = -\nabla p + \mu \nabla^2 \vec{u} + \vec{S} \Leftrightarrow \quad (2.20)$$

$$\rho \left( \frac{\partial u_i}{\partial t} + \frac{\partial}{\partial x_j} (u_i u_j) \right) = -\frac{\partial p}{\partial x_i} + \mu \frac{\partial^2 u_i}{\partial x_j^2} + S_i \Leftrightarrow$$

$$\begin{cases} \rho \left( \frac{\partial u}{\partial t} + u \frac{\partial u}{\partial x} + v \frac{\partial u}{\partial y} + w \frac{\partial u}{\partial z} \right) = -\frac{\partial p}{\partial x} + \mu \left( \frac{\partial^2 u}{\partial x^2} + \frac{\partial^2 u}{\partial y^2} + \frac{\partial^2 u}{\partial z^2} \right) + S_x \\ \rho \left( \frac{\partial v}{\partial t} + u \frac{\partial v}{\partial x} + v \frac{\partial v}{\partial y} + w \frac{\partial v}{\partial z} \right) = -\frac{\partial p}{\partial y} + \mu \left( \frac{\partial^2 v}{\partial x^2} + \frac{\partial^2 v}{\partial y^2} + \frac{\partial^2 v}{\partial z^2} \right) + S_y \\ \rho \left( \frac{\partial w}{\partial t} + u \frac{\partial w}{\partial x} + v \frac{\partial w}{\partial y} + w \frac{\partial w}{\partial z} \right) = -\frac{\partial p}{\partial z} + \mu \left( \frac{\partial^2 w}{\partial x^2} + \frac{\partial^2 w}{\partial y^2} + \frac{\partial^2 w}{\partial z^2} \right) + S_z \end{cases}$$

Where

- $\rho$  is the fluid density
- $t$  is the time
- $p$  is the pressure
- $\mu$  is the fluid dynamic viscosity
- $\nabla$  is the del operator
- $\vec{u}$  is the vector of flow velocity vector
- $\vec{S}$  is the vector of body force (per unit mass) acting on the continuum

These Navier-Stokes equations are a coupled system of non-linear partial differential equations that are difficult to solve analytically. For all but few special cases there is no closed-form solution to these equations (Anderson, 1995) and thus they must be solved numerically.

### 2.3.3 Turbulence Approach

The scope of problems addressed by CFD calculations often cross into the realms of turbulence. The most direct but costly numerical method for turbulence modelling is Direct Numerical Simulation (DNS). DNS resolves all spatial and temporal fluctuations in turbulent flow without need for modelling and provides most detailed information of the flow including turbulence. This means that the spatial and temporal discretisation should be fine enough to resolve such small scales. The cost required by DNS to resolve the entire range of scales is proportional to  $Re^3$  (Gatski et al., 1996) and this makes the method be prohibitive for most practical engineering fluids, even with the help of the most powerful computers available in the foreseeable decades. However, DNS is applicable at low Reynolds numbers and is



regarded as a promising tool to study the physics of turbulence and to develop turbulence models.

The second method to preserve the turbulence information at best is Large Eddy Simulation (LES). LES abandons the complete range capture of every scale through a filtering operation. The selected filtering function would separate any field scalar into a filtered and sub-filtered portion. The large scale eddies would be solved explicitly and the effect of smaller scales on large scales would be considered by SGS (Sub-Grid Scale) model. LES is less costly than DNS, but still very expensive under the currently available computing power for industrial flow applications because even the large eddy scales are still very small within the boundary layer of the fluid flow with a high Reynolds number and therefore a large number of grids are needed in these regions. As a result, further detailed descriptions of this model would not be given here.

The turbulence models based on Reynolds Averaged Navier-Stokes (RANS) equation are dominantly used in most engineering fluid simulations due to their economic computation cost and reliable precision. In Reynolds averaging, the separation of an instantaneous scalar quantity into a mean (ensemble-averaged or time-averaged) component and a fluctuating component is generally termed the “Reynolds decomposition”:

$$\phi = \bar{\phi} + \phi' \quad (2.21)$$

where

- $\phi$  denotes a scalar such as velocity, pressure
- $\bar{\phi}$  is the mean component
- $\phi'$  is the fluctuating component

The ensemble-averaging operation obeys the following rules:

$$\overline{\phi'} = 0 \quad \overline{\bar{\phi}} = \bar{\phi} \quad \overline{\bar{\phi} + \phi'} = \bar{\phi} \quad \overline{\bar{\phi}f} = \bar{\phi}\bar{f} \quad \overline{\phi'f} = 0 \quad \overline{\phi'f} = \bar{\phi}\bar{f} \quad (2.22)$$

$$\frac{\partial \bar{\phi}}{\partial x_i} = \frac{\partial \bar{\phi}}{\partial x_i} \quad \frac{\partial \bar{\phi}}{\partial t} = \frac{\partial \bar{\phi}}{\partial t} \quad \frac{\partial^2 \bar{\phi}}{\partial x_i^2} = \frac{\partial^2 \bar{\phi}}{\partial x_i^2} \quad \frac{\partial^2 \bar{\phi}'}{\partial x_i^2} = 0 \quad \frac{\partial \bar{\phi}'}{\partial x_i} = 0$$

Applying the Reynolds decomposition to the velocity and pressure in Navier-Stokes equations (2.24) and (2.25) using the ensemble-averaging operation rules, we have the Reynolds-averaged Navier-Stokes equations (RANS) in tensor notation:

$$\frac{\partial \bar{u}_i}{\partial x_i} = 0 \quad (2.23)$$

$$\rho \left( \frac{\partial \bar{u}_i}{\partial t} + \frac{\partial}{\partial x_j} (\bar{u}_i \bar{u}_j) \right) = -\frac{\partial \bar{p}}{\partial x_i} + \mu \frac{\partial^2 \bar{u}_i}{\partial x_j^2} + S_i - \frac{\partial (\rho \overline{u'_i u'_j})}{\partial x_j} \quad (2.24)$$

As can be seen in equation (2.29), the right hand side of the momentum equation now contains a term that is defined as the Reynolds stress tensor,  $-\rho \overline{u'_i u'_j}$ . The Reynolds stresses are additional unknowns and their presence means that the governing equations for the turbulent flows are not closed. As a result, additional equations are needed to make the RANS equations closed. An approximation allowing a solution for the Reynolds stresses and thus providing closure to the RANS equations is given by use of a turbulence model, to represent the velocity fluctuations or their effects on the flow.

Turbulence models of various complexities have been developed and can generally be classified in two groups: eddy viscosity models and Reynolds stress models. Reynolds stress models model the stresses directly through a set of transport equations, one for each stress, thus requiring the solution of six additional transport equations. The key advantage of the Reynolds stress models is that they do not require isotropy in the stresses, as all stresses are computed directly. However, the additional complexity renders these models more expensive to solve, and they are therefore not widely used. In comparison, eddy viscosity models only require one or two additional transport equations. Various eddy viscosity models are implemented

in commercial flow solvers such as ANSYS FLUENT and these are usually the first choice for modelling turbulence in an engineering application.

The underlying assumption employed in all eddy viscosity models is the Boussinesq hypothesis (Boussinesq, 1878), which provides the results of the Reynolds stress tensor using the gradient of the time-mean velocity field. The corresponding equation in tensor notation is

$$-\rho \overline{u'_i u'_j} = \mu_t \left( \frac{\partial \bar{u}_i}{\partial x_j} + \frac{\partial \bar{u}_j}{\partial x_i} \right) \quad (2.25)$$

where

$\mu_t$  is the eddy viscosity (also referred to as turbulent viscosity)

It should be noted that the Boussinesq hypothesis assumes the eddy viscosity to be isotropic. According to the equations introduced to solve  $\mu_t$ , the eddy viscosity turbulence models can be classified as:

- a) Zero-equation algebraic models: Cebeci-Smith model, Baldwin-Lomax model
- b) One-equation Spalart-Allmaras model
- c) Two-equation models: Standard  $k - \varepsilon$  model, RNG  $k - \varepsilon$  model, Realizable  $k - \varepsilon$  model, Standard  $k - \omega$  model, SST  $k - \omega$  model
- d) Four equation  $v^2 - f$  model
- e) Laminar-turbulent transition models:  $k - kl - \omega$  Transition Model, Transition SST model

Detailed theories about these models can be seen in ANSYS Fluent Theory Guide. The choice of turbulence model for a specific will depend on considerations such as the physics encompassed in the flow, the established practice for a specific class of problem, the level of accuracy required, the available computational resources, and the amount of time available for the simulation. Generally, Numerical simulations

employing the zero-equation model are usually restricted to attached boundary-layer flows, which can be modelled using only local relations (Bredberg, 2001). Spalart-Allmaras model could get reasonable prediction results for aerodynamics wall-bounded flows and boundary flows subjected to adverse pressure gradients (ANSYS, 2012). High Reynolds number  $k - \varepsilon$  and  $k - \omega$  models are widely used in industrial turbulent flows for their acceptable computation cost and reasonable accuracy (ANSYS, 2012). Low Reynolds number  $k - \varepsilon$ ,  $k - \omega$  and the Laminar-turbulent transition models are believed to be promising to accurately predict boundary layer development and transition from laminar to turbulent flows (ANSYS, 2012).

In general, turbulence models based on the  $\varepsilon$ -equation predict the onset of separation too late and under-predict the amount of separation later on (Johnson and King, 1984), they are therefore not widely used in external aerodynamics especially airplanes involves the stall phenomenon. The  $k-\omega$  models developed to solve this problem have shown a significantly more accurate prediction of adverse pressure gradient boundary layer flows and separation in a number of test cases and in industrial applications (Menter, 1993). The use of the standard  $k-\omega$  model (Wilcox, 1998) is not generally recommended in ANSYS Fluent due to its relatively strong sensitivity of the solution depending on the freestream values of  $k$ - and  $\omega$ - outside the shear layer (Menter, 1992). The  $k-\omega$  based Shear-Stress-Transport (SST  $k-\omega$ ) model has been designed to avoid this disadvantage by the inclusion of transport effects into the formulation of the eddy-viscosity (Menter, 1994). This results in a major improvement in terms of flow separation predictions. The superior performance of this model has been demonstrated in a large number of validation studies (Bardina et al., 1997). In areas with high normal stresses such as congestive flow standard SST  $k-\omega$  model generates too high turbulence levels, which leads to a significant qualitative change in the calculated flow pattern (Yakhot et al., 1992). In addition, the SST model is as economical as the widely used  $k-\varepsilon$  model, but it offers much higher fidelity, especially for separated flows, providing excellent answers on a wide range of flows and near-wall grid conditions. ANSYS Fluent complements the SST model with numerous other turbulence modeling innovations, including an automatic wall treatment for maximum accuracy in wall shear and heat transfer

predictions and a number of extensions to capture effects like streamline curvature. Although the SST  $k-\omega$  model is for fully turbulent flow, it can accommodate the transitional regime with a low-Reynolds number correction in FLUENT.

In order to avoid the high resolution requirements of LES, the Detached Eddy Simulation (DES) has been proposed by Spalart and co-workers (Spalart 2000, Spalart et al. 2006, Strelets 2001), by proposing a hybrid formulation which switches between RANS and LES based on the grid resolution provided. This strategy is optimal for wall-bounded applications, since sub-grid scale RANS models are utilized locally to resolve the boundary layer whilst the turbulent scales are properly resolved in the unsteady regions. The cost scaling of the method is thus favourable since LES is not applied to resolution of the relatively smaller-structures that populate the boundary layer. The DES however carries the same grid sensitivity requirements as pure LES in the detached regions, and past experience has proven that results are highly sensitive to grid spacing that precludes DES from being used with confidence on arbitrarily complex industrial geometries (Menter and Kuntz, 2002). In order to avoid this limitation, the DES concept has been extended to Delayed-DES (DDES), which provides additional shielding functions (Shur et al. 2008) to ensure that the model does not inadvertently switch to LES within the boundary layer as a result of grid sensitivity. Grid generation of (D)DES is more complicated than for a simple RANS or LES case due to the RANS-LES switch. Independent of this technical detail, (D)DES is the most frequently applied hybrid RANS-LES model in industrial CFD simulations (Spalart 2000, Spalart et al. 2006, Strelets 2001, Shur, 2008, Haase et al., 2009).

### **2.3.4 Near-Wall Treatments**

Turbulent flows are significantly affected by the presence of walls where the viscosity-affected regions have large gradients in the solution variables, and the momentum and other scalar transports occur most vigorously. Hence, successful prediction of wall-bounded turbulent flows is partly determined by the accurate presentation of the near-wall region flows (Gerasimov, 2006).

Central issues of wall-bounded flows are the forms of the mean velocity profiles and the friction laws, describing the shear stress exerted by the fluid on the wall. Close to the wall, the flow is affected by viscous effects and the mean flow velocity  $u$  depends on several parameters as formulized below

$$u = f(y, \rho, \mu, \tau_w) \quad (2.26)$$

Where

- $y$  is the distance from the wall
- $\rho$  is fluid density
- $\mu$  is fluid viscosity
- $\tau_w$  is the wall shear stress

By dimensional analysis it is found that

$$u^+ = \frac{u}{u_\tau} = f\left(\frac{y\rho u_\tau}{\mu}\right) = f(y^+) \quad (2.27)$$

Where

$$u_\tau = \sqrt{\tau_w/\rho} \quad \text{is the friction velocity}$$

The formula 2.44 contains the definitions of two important dimensionless parameters,  $u^+$  and  $y^+$ . The wall  $y^+$  is a non-dimensional distance similar to local Reynolds number, often used in CFD to describe how coarse or fine a grid is for a particular flow. It is the ratio between the turbulent and laminar influences in a cell. Very close to the wall the  $y^+$  is of small value, viscous damping reduces the tangential velocity fluctuations, while kinematic blocking reduces the normal fluctuations. Towards the outer part of the near-wall region the value of  $y^+$  increases, the turbulence is rapidly augmented by the production of turbulent kinetic energy due to the large gradients in mean velocity. The relationship between  $u^+$  and  $y^+$  is called the ‘Law of the Wall’, which could represent the different layers of the near-wall region as shown in Figure 2-12 (Fluent12.1, 2010).

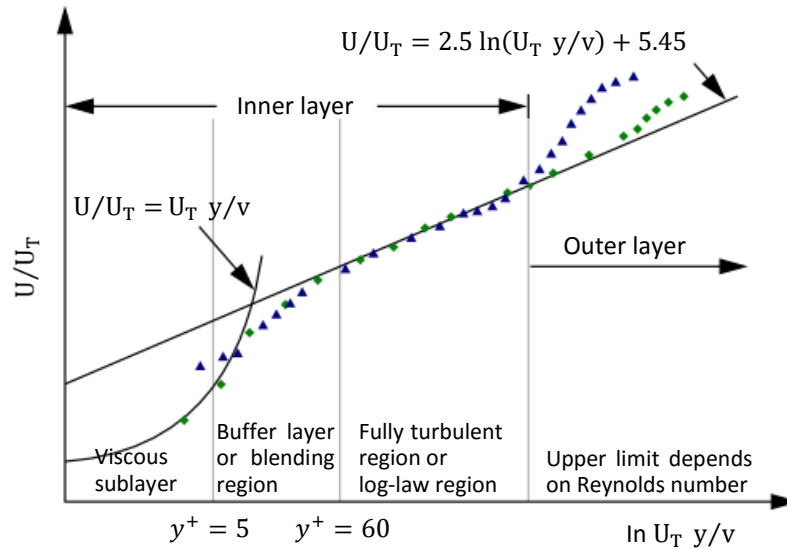


Figure 2-12 Subdivisions of the Near-Wall Region (Fluent12.1, 2010)

From Figure 2-12 it can be seen that the near-wall region consists of the inner layer and the outer layer. The inner layer (viscosity-affected region) is about 10-20% of the total thickness of the wall layer and is composed of three zones corresponding to the wall  $y^+$ , namely the:

- a) Viscous sub-layer ( $y^+ < 5$ ): viscous stresses dominate the flow;
- b) Buffer layer ( $5 < y^+ < 30$ ): viscous and turbulent stresses are of similar magnitude;
- c) Log-law layer ( $y^+ > 30$  to 60): turbulent stresses dominate.

Traditionally, in ANSYS FLUNET, there are two approaches to model the near-wall region, namely the Wall Function Approach and the Near Wall Model Approach, as depicted schematically in Figure 2-13. The first approach uses semi-empirical formulas (also wall functions) to bridge the viscosity-affected region between the wall and the fully turbulent region, which means the viscosity-affected inner region (viscous sub-layer and buffer layer) is not resolved. The use of wall functions obviates the need to modify the turbulence models to account for the presence of the wall. While in the second approach, the turbulence models are modified to enable the

viscosity-affected region to be directly resolved with a grid all the way to the wall, including the viscous sublayer.

The  $k - \varepsilon$  models, the RSM, and the LES model are primarily valid for turbulent core flows (i.e., the flow in the regions somewhat far from walls). Consideration therefore needs to be given as to how to make these models suitable for wall-bounded flows. ANSYS Fluent provided four options for the near-wall treatments of the  $k - \varepsilon$  models and the RSM. They are the standard wall functions, the non-equilibrium wall functions, the enhanced wall functions and user-defined wall functions. Detailed descriptions of these near-wall options can be seen in Fluent 12.1 (2010). For the LES modelling, an alternative near wall approach in the name of the Werner-Wengle wall functions can be applied for wall-bounded flows. The Spalart-Allmaras and  $k - \omega$  models are designed to be applied throughout the boundary layer, they use Enhanced Wall Treatment (EWT) as default, provided that the near-wall grid resolution is sufficient.

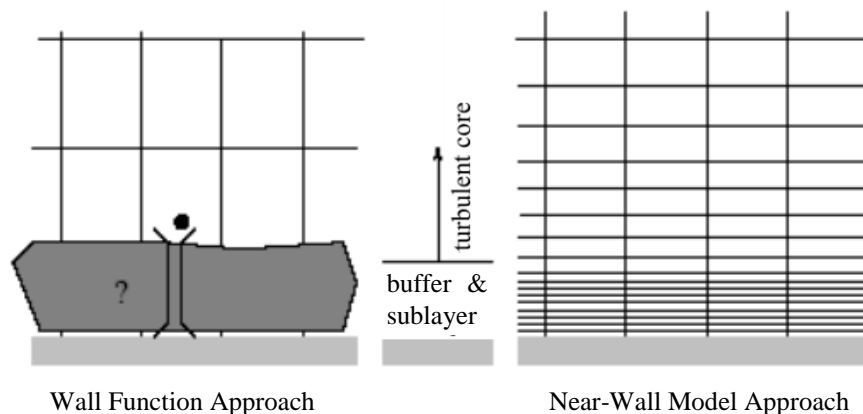


Figure 2-13 Near-Wall Treatments in FLUENT (Fluent 12.1, 2010)

The wall function approach substantially saves computational resources in most high Reynolds number wall bounded flows and is popular because it is economical, robust, and can be reasonably accurate. It can be a practical option for the near-wall treatments for industrial flow simulations. However, the wall function approach becomes less reliable when the flow conditions depart too much from the ideal



conditions underlying the wall functions. One example of limitations of the wall function approach is for flows with severe pressure gradients leading to boundary layer separations (Rodi, 1997; Catalano et al., 2003). At such situations the appropriate low-Reynolds-number boundary conditions (e.g. the SST model) are recommended, and values of wall  $y^+ \leq 1$  are much desirable to guarantee fine enough grid in the near wall region.

## 2.3.5 Numerical Solver

ANSYS Fluent uses a finite-volume approach to solve the governing equations numerically. The numerical approach is a control-volume-based technique and consists of the following three procedures:

- a) Discretizing the spatial domain into finite control volumes (cells) with the use of a computational grid.
- b) Integrating the governing equations on each control volume to obtain a discrete equation for the dependent variable.
- c) Linearizing the discretized equations and solving the linear system of equations to obtain the updated values of the dependent variables.

In the present study, the segregated pressure-based solver is applied to perform the numerical solution for low-speed incompressible flow. By using this approach, the pressure field is obtained by solving a pressure correction equation, which results from combining continuity and momentum equation in such a way that the velocity field, corrected by the pressure, satisfies the continuity. The governing equations are non-linear and coupled one another. The solution process involves therefore iterations, wherein the entire set of governing equations is solved repeatedly until the solution converges. The segregated algorithm solves the governing equations in a sequential manner. This algorithm is memory efficient but solution convergence is relatively slow with this method.

The solution of Navier-Stokes equation is complicated because of the lack of an independent equation for the pressure, whose gradients contribute to each of the three

momentum equations. Moreover, for the incompressible flows dealt with here, the continuity equation does not have a dominant variable, but it is rather a kinematic constraint on the velocity field. Thus, the pressure field (the pressure gradients when incompressible) should be generated by satisfying mass conservation. Several approaches for pressure-velocity coupling are possible, ANSYS Fluent provides four types of pressure-based segregated algorithms: SIMPLE (Semi-Implicit Method for Pressure-Linked Equations), SIMPLEC (SIMPLE-Consistent), PISO (Pressure-Implicit with Splitting of Operators) and FSM (Fractional Step Method). SIMPLE or SIMPLEC are useful mainly for steady computations and low-skewed grids. PISO is recommended for transient calculations; PISO with skewness correction may also be useful for steady-state and transient calculations on highly skewed grids. FSM is available with the use a NITA (Non-Iterative Time-Advancement) scheme and has similar characteristics as PISO.

For transient simulations, the governing equations must be discretized in both space and time. In our calculations, the temporal discretization used for unsteady incompressible computations is first order implicit. For spatial discretization, we usually need to perform a few iterations with the first-order scheme and then turn on the second-order scheme and continue the calculation to convergence. For turbulent flows, the upwind schemes are usually used together with the RANS models, a second-order-accurate bounded central differencing discretization scheme should be applied for LES and DES.

Under the pressure-based solver, a pressure interpolation scheme is required to compute the face values of pressure from the cell values. The schemes adopted were the default “standard” scheme and the PRESTO! (PREssure STaggering Option) scheme. The standard scheme computes the face pressure using momentum equation coefficients. This procedure works well as long as the pressure variation between cell centers is smooth. When there are jumps or large gradients in the momentum source terms between control volumes, the pressure profile has a high gradient at the cell face, and cannot be interpolated using this scheme. For flows with high swirl numbers, high-Rayleigh-number natural convection, high-speed rotating flows, flows

involving porous media, and flows in strongly curved domains, the PRESTO! Scheme, which uses the discrete continuity balance for a staggered control volume about the face to compute the staggered (i.e., face) pressure, is preferred.

Boundary conditions specify the flow variables on the boundaries of the chosen physical model. They are therefore a critical component of a CFD simulation, and it is important they are specified appropriately. The utilized boundary conditions are described as follows

- **Wall (no-slip)**

Wall boundary conditions are used to bound fluid and solid regions, for instance the blade surface in a HATT model. The no-slip condition is the default setting for viscous flows and the shear-stress calculation in turbulent flows follows the adopted turbulent model.

- **Velocity-Inlet**

Velocity inlet boundary conditions are used to define the flow velocity, along with all relevant scalar properties of the flow, at flow inlets. This boundary condition is suitable for incompressible flows, whereas for compressible flows will lead to a non-physical result because stagnation conditions are floating. It is possible to set both constant and variable parameters, as well as they can be alternatively uniform or non-uniformly distributed along the boundary itself.

- **Pressure-Outlet**

Pressure outlet boundary conditions require the specification of a static (gauge) pressure at the outlet boundary. It allows also a set of backflow conditions to minimize convergence difficulties. The value of the specified static pressure is used only while the flow is subsonic. Should the flow become locally supersonic, the specified pressure will no longer be used; pressure will be

extrapolated from the flow in the interior. All other flow quantities are extrapolated from the interior.

- **Pressure Far-Field**

Pressure far-field conditions are used to model a free-stream condition at infinity, with free-stream Mach number and static conditions being specified. To effectively approximate true infinite-extent conditions, it is suggested to place the far-field boundary far enough from the object of interest. For example, in lifting airfoil calculations, it is not uncommon for the far-field boundary to be a circle with a radius of 20 chord lengths (Wernert et al., 1996).

- **Symmetry**

It is the analogous of a zero-shear slip wall in viscous flow. Zero normal velocity is at a symmetry plane and zero normal gradients of all variables exist there as well.

- **Periodic**

They are used to take advantage from the periodically repeating nature of both the geometries and flow patterns. Periodic boundaries are always in pair and the overlooking volumes on the two surfaces are direct neighbors, i.e. the outcoming flow from one, the incoming flow is into the other.

Generally in the CFD simulation of tidal turbine flows, the approaches available to simulate the rotational motion are the sliding mesh and the Multiple Reference Frame (MRF) models. Detailed descriptions of these two models can be read from the ANSYS FLUENT tutorial guide. For the cases studied in this thesis, the MRF model was preferred to simulate the rotational motion. There are several reasons for this choice. First of all, the MRF approach is simpler and computationally cheaper, since it does not require complicated grid motion, and uses a steady state calculation

of the flow field. Moreover, the rotor/stator effects were considered negligible because the substructures were ignored in the numerical model. Another possibility relates to numerical errors related to the complexity of the sliding mesh procedure. For the sliding mesh case, around the rotor we are solving a transient problem in a grid whose geometry and topology are continually changing with time. This may well introduce additional temporal discretization errors that are absent in the MRF solution.

The dynamic mesh capability can be used to solve the flow-driven rigid-body motion problem, such as a pitching airfoil. In this situation, the motion can be described using either boundary profiles or user-defined functions (UDFs), all of the boundaries of a given grid zone move together in a rigid fashion. The nodes of the grid move in space (relative to the fixed, global coordinates), but the cells defined by the nodes do not deform. Furthermore, grid zones moving adjacent to one another can be linked across one or more non-conformal interfaces. As long as the interfaces stay in contact with one another (i.e., “slide” along a common overlap boundary at the interface), the non-conformal interfaces can be dynamically updated as the meshes move, and fluid can pass from one zone to the other. For transient problems, the implicit mesh updating can be enabled to have the dynamic mesh updated during a time step (as opposed to just at the beginning of a time step).

For performing large calculations that are computationally expensive, the underlying grid is decomposed into various numbers of smaller grids that are distributed to various processors for performing numerical calculations in parallel using many CPUs. In the current study, the University of Strathclyde in-house supercomputer cluster, ARCHIE-WeSt, is used for parallel computations. ARCHIE-WeSt comprises almost 3500 cores for distributed parallel computing providing almost 38 Teraflops peak performance, eight 512GB RAM large memory nodes, 8 GPU servers, 2 visualisation servers and 150TB of high performance LUSTRE storage. The numbers of partitions of the grids for parallel processing are made according to the complexity of the problem. For example, a grid used for flow simulations over a tidal turbine rotor consisted of about 2.5 million hexahedral cells is decomposed into 24 smaller

partitions, such that the case runs on 24 processors with about 100,000 cells on each processor, this specific number for partitioning is decided so that there is least waiting time on each processor during the parallel run.

## **2.4 Summary**

This chapter provides the background knowledge required to answer the research questions posed in this thesis. The unsteady hydrodynamics that might occur on HATT blades are explained. The scaling effects that have important influence on the performance predicting of a scaled HATT are discussed. Since dynamic stall is an important consequence of unsteady blade loading, there is also a detailed explanation of this phenomenon by beginning with the introduction of boundary layer separation and static stall. Finally, background knowledge of CFD is described, which provides a clear understanding of the numerical methods that was utilized in this thesis.

# Chapter 3 Case Study of 2-D Dynamic Stall

---

## 3.1 Introduction

It is a challenge to use CFD methods to accurately model the unsteady hydrodynamic loads on HATT blades and the flow fields through the turbine. Firstly, the flow passing through a rotating blade is much more complicated than that of a 2-D airfoil simulation because the blade elements' angles of attack vary along the blade. Moreover, the turbine blade loads are may be significantly affected by the occurrence of dynamic stall, and there are also centrifugal forces along the blade due to rotor rotation, which makes the turbulent flow around the blade more complex. On the other hand, simulation accuracy is sensitive to the turbulence model, grid and time step size selected and applied in the calculation. Typically a high resolution structured grid with advanced turbulence and transition modelling as well as small time step is required for the 3-D turbine, which places a high demand on computational power and time. Besides, geometry of the blades is difficult to grid with quality due to the span-wise twist and size difference between tip and root. Finally, experimental data suitable for validation of the computation results are relatively rare. Having in mind that 3-D CFD calculation of HATT blade loads is difficult and costly, it is useful to benchmark the ability to accurately predict the time-dependent blade loads and fundamental features of vorticity dynamics in 2-D before more complex 3-D effects are addressed.

Nominally 2-D problems remain useful as validation cases for computations, as explorations of the salient features of turbine blade dynamics, and as means of addressing large parameter studies with comparative simplicity. In this chapter, a basic 2-D CFD test of a pitching airfoil was carried out to determine the turbulence model and grid method to prepare for the modelling of unsteady HATT blade load and relevant dynamic stall phenomenon. This validation case is based on the experimental work of Lee and Cerontakos (2004), which involves a wind tunnel test of NACA0012 airfoil pitching in a sinusoidal pattern,  $\alpha = \alpha_0 + \alpha_1 \sin(\omega t)$ , at

relatively low Reynolds number. The main reasons for choosing this case are listed below:

- a) The hydrodynamics of a HATT blade element under the conditions such as unsteady harmonic oscillatory inflow is qualitatively similar to what occurs when an airfoil performs a harmonic pitching, in terms of the formation and shedding of a leading edge vortices, trailing edge separation etc., due to the constant changing in the angle of attack.
- b) The phenomenon of dynamic stall is an inherent effect of the operation of a HATT at low tip-speed ratios. The presence of dynamic stall has significant impact on both power and blade loads. However, there are very limited research literatures directly pertaining to dynamic stall of tidal turbines. Insight into the phenomenon associated with stall is instead directed to works in the helicopter and wind turbine contexts (Shipley et al., 1995). The majority of the experimental studies used to infer dynamic stall phenomenon involve wind tunnel tests of 2-D airfoils typically oscillating in pitch.
- c) Most of the previous researches on dynamic stall have been devoted to flows at relatively high Reynolds numbers ( $Re \geq 10^6$ ), however, the HATT blade element may operate under a relatively low Reynolds number such as of the order of  $10^5$  or even lower, due to the slower flow velocity and smaller size (especially elements near the blade tip) compares to wind turbine. Complex boundary layer flow transition will occur under the low Reynolds number, thus it is of great importance to advance the knowledge to the level on which the phenomenon can be accurately predicted and precisely controlled.
- d) Although the dynamic stall flow is inherently a 3-D phenomenon, in the experimental investigation by Lee and Cerontakos (2004), measurements have been taken to ensure a 2-D flow in the mid-span plane, where the experimental data were obtained, and the 2-D non-uniformity of the flow over the airfoil was within 4% of the free stream value with a hot-wire probe



employed. Therefore, the data obtained can be employed with confidence for the purpose of validating 2-D numerical simulations. Furthermore, Wang et al. (2012) and Gharali and Johnson (2013) published results of CFD turbulence modelling of deep dynamic stall validated with these experimental results, which can be compared to evaluate the work of this chapter.

When considering the 2-D numerical simulations of the dynamic stall process, existing literatures available for the relative low Reynolds number regime are very limited. Spentzos et al. (2005) investigated the dynamic stall over an oscillating blade with Reynolds number of  $10^4$ - $10^5$ , using the unsteady Reynolds-Averaged Navier-Stokes (URANS) method but coupled with the standard  $k - \omega$  model. The velocity profiles and pressure distributions obtained were compared favourably against experiments. However, no validation on the predicted aerodynamic forces on the oscillating blade was reported. Martinat et al. (2008) evaluated the behaviour of various URANS and hybrid delayed DES (DDES) modelling approaches on the flow around a pitching airfoil with Reynolds number ranging from  $10^5$  to  $10^6$ . The turbulence models employed in their URANS study include the Spalart-Allmaras model,  $k - \varepsilon$  Chien model, SST  $k - \omega$  model, and the so-called Organized Eddy Simulation (OES) for modelling the non-equilibrium turbulence effects. Advanced turbulence models like OES and SST modelling have shown better results than classical URANS models for the occurrence of dynamic stall prediction. The DDES predictions in 2-D did not show significant improvements over the URANS predictions. None of the models present a satisfactory agreement with the corresponding experimental data in particular at the down-stroke phase, in which the flow behaviour is proven to be 2-D dependent, as concluded in works of McAllister et al. (1978) and Martinat et al. (2008). Wang et al. (2010a, 2010b, 2012) performed a series of numerical investigations to assess the ability of various turbulence models to simulate the dynamic stall at relatively low Reynolds numbers. Turbulence models such as the Standard  $k - \omega$  model, SST  $k - \omega$  model,  $v^2 - f$  model, Transition SST ( $\gamma - Re_\theta$ ) model and SST  $k - \omega$  based DDES model were employed successively. It was noticed that the SST  $k - \omega$  model,  $v^2 - f$  model and Transition SST ( $\gamma - Re_\theta$ ) model can predict the lift and drag for a large portion of the up-stroke

phase well, except at high angle of attacks and they all failed to reproduce flow reattachments accurately over the down-stroke phase. The SST  $k - \omega$  based DDES presents generally good agreement with the experimental data, especially for the down-stroke phase. However, DDES predicts a slightly earlier stall point than that observed in the experiment and it fails to capture the peak of the lift coefficient for the case studied. Gharali and Johnson (2013) studied the effects of horizontal oscillations of the freestream velocity superimposed on a pitch oscillating NACA0012 airfoil using the SST  $k - \omega$  model coupling with a low-Reynolds number correction. It was found that the instantaneous loads are compared well with the existing experimental results of Lee and Gerontakos (2004) and more stable than the SST  $k - \omega$  results of Wang et al. (2010a) by considering the cell skew factor as a key parameter, but the vortical structures as well as wake velocity profiles during post stall cannot be exactly captured.

Based on the above discussions and summary, in this chapter, the SST  $k - \omega$  model with low-Reynolds correction, the Transition SST model and the SST  $k - \omega$  based DDES model were applied by using ANSYS Fluent. Numerical results were compared with experimental data of Lee and Cerontakos (2004) and CFD data of Wang et al. (2010a, 2010b, 2012) in terms of their capability and accuracy in capturing the dynamic stall flow characteristics and the aerodynamic forces.

## 3.2 Description of the Test Case

In the work of Lee and Gerontakos (2004), the experimental investigation was conducted in a  $0.9\text{m} \times 1.2\text{m} \times 2.7\text{m}$  low speed, suction-type wind tunnel with a free stream turbulence intensity of 0.08% and at a free stream velocity  $u_\infty = 14\text{ m/s}$ . The test model is a NACA0012 airfoil which has a chord length of  $c = 0.15\text{ m}$  and a span of  $0.375\text{ m}$ , resulting in a Reynolds number of  $Re_c = 1.35 \times 10^5$  based on the chord length. During the test, the NACA0012 airfoil executes a sinusoidal pitching motion around an axis located at a quarter of its chord ( $0.25c$ ) from the leading edge, with the instantaneous angle of attack of  $\alpha = 10^\circ + 15^\circ \sin(18.67 * t)$ , and a reduced frequency of  $\kappa = 0.1$ .

The airfoil was fitted with two end plates with 30 cm in diameter in the experiments to minimize the flow leakage from the blade tip (blade tip effects) and to eliminate as much as possible any substantial 3-D effects of the flow at the measurement location at the mid-section of the blade. By checking the blade wake flow, the flow non-uniformity along the span-wise direction was found to be negligible in the experimental investigations. A comprehensive description of the experimental setup is detailed in Lee and Gerontakos (2004).

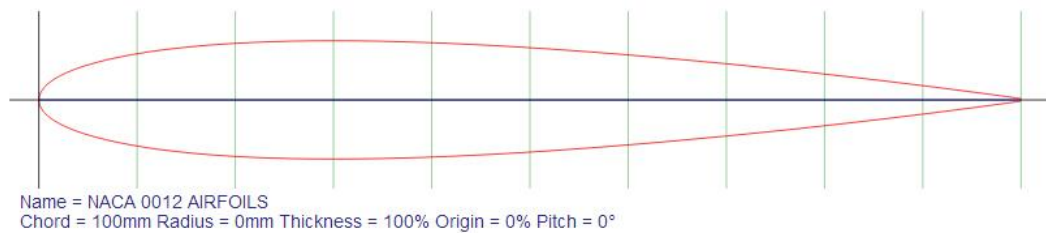


Figure 3-1 The profile of the NACA0012 Airfoil

### 3.3 Numerical Methods

The profile of the NACA0012 aerofoil is depicted in Figure 3-1. Geometric model and computational grids were generated using the commercial software ANSYS ICEM. A typical 2-D C-topology structured grid was used for numerical computation. The whole computational domain is described in Figure 3-2. The airfoil coordinates were read to form the inner boundary of the computational domain. The external boundary of the computational domain was determined at 20 chord lengths away from the airfoil at each side. This domain size is found to be sufficient on the basis of other researchers' work (e.g., Wernert et al., 1996; Spentzos et al., 2005; Wang et al., 2012), which not only allows the air flow to be fully expanded to eliminate the boundary reflections, but also minimized the total number of computational cells without losing the accuracy in the simulations. Stationary wall with no-slip shear

condition was imposed on the airfoil surface. As the computational domain is large enough, the pressure far-field boundary condition was used for the outer boundary.

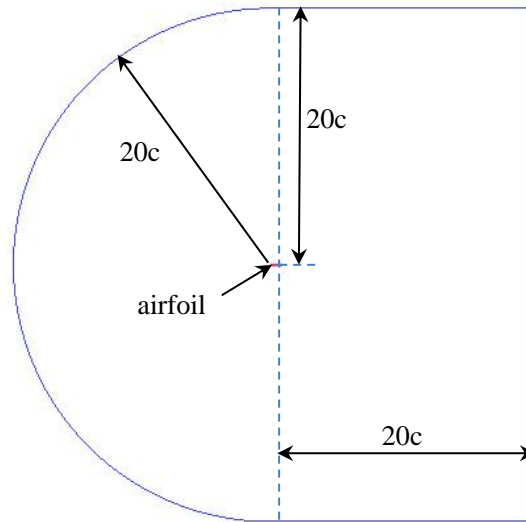


Figure 3-2 The C-type Computational Domain (here 20c means 20 times of the chord length)

The choice of grid size and time step size for current study were arise from the very thorough numerical refinement study of Wang et al. (2012), hence in this chapter grid size and time step size sensitivity studies are not discussed in detail. A structured grid consists of approximately 610,000 quadrilateral cells was generated for URANS modelling, which is similar to the grid consists of about 605,000 cells in the numerical study of Wang et al. (2012). In order to accurately capture the pressure gradient at the boundary layer, a large number of cells were placed around the aerofoil surface. Along the airfoil there were 580 grid nodes and they were clustered close to the leading and trailing edges, as can be seen in Figure 3-3. The height of the first row of the cells bounding the airfoil was set to be  $10^{-5}c$ , which ensures the wall  $y^+ \leq 1$  so that the boundary layer flow can be properly resolved without using a wall function. In the far field area, the grid resolution can become progressively coarser since the flow gradients approach zero, therefore the height of the cells was set to expand with a growth factor of 1.2 towards the external boundary of the computational domain to reduce the cell number far from the airfoil. For DDES

modelling, the grid need to be refined based on the URANS grid because LES is activated to resolve the larger scale turbulence eddies in the regions outside the boundary layer. The grid refining was processed on the basis of the ‘Young-Person’s Guide (YPG) to Detached-Eddy Simulation Grids’ by Spalart (2001) and estimations by Wang et al. (2012). The size of the DDES grid after refining based on the URANS grid sums up to approximately 795,000 quadrilateral cells. The numerical time step sizes were set based on the characteristic time  $T_c$  defined as  $c/u_\infty$ , and have the same value as that be used in the numerical study of Wang et al. (2012). For URANS calculation the time step size was  $0.0125T_c$ , and for DDES the time step size was  $0.005T_c$  as the DDES requires very fine time step size to simulate small turbulent structures.

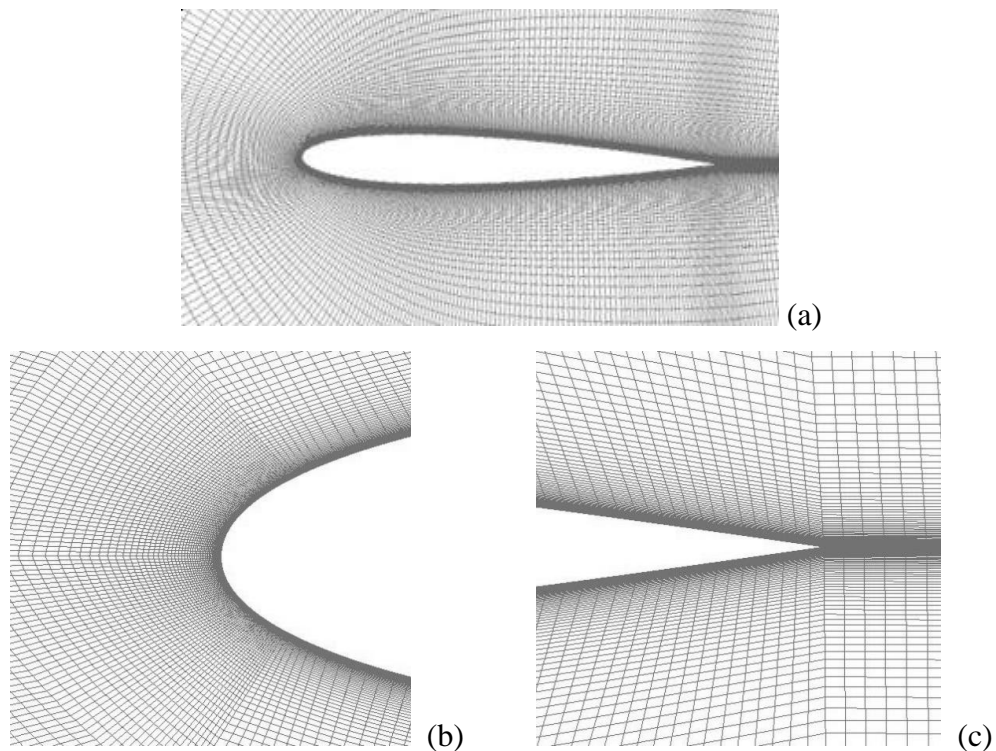


Figure 3-3 Grids distribution of the C-type grid used for URANS (a) around the airfoil (b) around leading edge (c) around the trailing edge

Table 3-1 Computational conditions

Airfoil	NACA0012	
Solver	Pressure-Based Transient Solver	
Fluid Material	Air	
Flow Type	Incompressible Flow	
Temperature	300k	
Kinematic Viscosity	1.4607e-05 m <sup>2</sup> /s	
Reynolds Number	1.35e5	
Density	1.225 kg/m <sup>3</sup>	
Pressure	101325 pa	
Flow Speed	14 m/s	
Dynamic Mesh	Rigid Body	
Turbulent model	SST k – ω, Transition SST	SST k – ω based DDES
Pressure-Velocity Coupling	SIMPLEC	SIMPLEC
Spatial Discretization	<i>Gradient</i> Last Squares Cell Based <i>Pressure</i> Standard <i>Momentum</i> Second Order Upwind <i>Turbulent Kinetic Energy</i> Second Order Upwind <i>Specific Dissipation Rate</i> Second Order Upwind	<i>Gradient</i> Last Squares Cell Based <i>Pressure</i> Standard <i>Momentum</i> Bounded Central Differencing <i>Turbulent Kinetic Energy</i> Second Order Upwind <i>Specific Dissipation Rate</i> Second Order Upwind
Transient Formulation	First Order Implicit	
Boundary condition	Pressure far-field boundary condition Stationary Wall with No Slip Shear Condition Turbulence intensity: 0.08%	

Based on the discussions on CFD turbulence modelling in the previous chapter, the pressure based transient solver was employed and the segregated algorithm that solves the governing equations sequentially was chose to reduce the memory demand. In terms of the settings of solution methods, the classical SIMPLEC algorithm was employed for pressure-velocity coupling, which is useful mainly for steady

computations and low-skewed grids, even if some unsteady cases are studied, and in spite of the high degree of distortion within the mesh. This is because the convergence appeared acceptable, even when compared to the PISO scheme that is usually the best option for transient computations. Proper under-relaxation factors were set for the different investigated solutions. The convective terms in the URANS equations were discretized with a second-order upwind scheme, the gradients of solution variables were discretized with the default Least-Squares Cell-Based approach, and the Standard scheme was chosen for calculating cell-face pressures when using the pressure-based solver in FLUENT. For DES, the *SST*  $k - \omega$  model and the DDES option was applied for RANS calculation, the default Bounded Central Differencing scheme was adopted for momentum discretization. With special care taken to make sure the time-step employed is small enough to obtain accurate numerical solutions, the temporal term has been discretized with a first-order implicit scheme.

Detailed information on CFD solver setup can be found in ANSYS Fluent USER'S GUIDE. Table 3-1 is a summarization of the computational conditions used in current study. In order to simulate the sinusoidal pitching motion of the blade, the whole grid was set to pitch like a rigid body with the same sinusoidal mode as the airfoil, by using the dynamic mesh technique with a user defined function (UDF) subroutine developed and attached to the ANSYS Fluent solver.

The required CPU time for one pitching cycle in the 2-D calculating is reported in Table 3-2.

Table 3-2 Details of the CPU time required for 2-D calculations

Grid	Size	No of processors	CPU time (s) per cycle
URANS	610,000	12	$3.9 \times 10^4$
DES	795,000	12	$5.4 \times 10^4$

## 3.4 Results

### 3.4.1 Lift and Drag Force Predictions

To confirm the accuracy of the numerical simulations, the instantaneous lift and drag coefficients were compared with the existing experimental results of Lee and Gerontakos (2004) for sinusoidal pitch oscillation with a steady freestream, as well as numerical simulation results published by Gharali and Johnson (2013) using the SST  $k - \omega$  turbulence model with low-Reynolds correction, and by Wang et al. (2012) using the Transition SST and SST  $k - \omega$  based DDES model.

It should be noted that after the first pitching cycle, the aerodynamic lift coefficients become periodic as shown in Figure 3-4. However, unlike the URANS simulating results that can finally achieve an identical periodical solution, the computed values of lift coefficient obtained from the SST  $k - \omega$  based DDES method present a strong fluctuating behaviour that differs from cycle to cycle. This fluctuating flow feature is likely due to the existence of the complex and intensive unsteadiness of the separated flows at deep stall conditions in the down-stroke (decreasing angle of attack) phase being captured even with a DDES calculation in 2-D. The fluctuated aerodynamic loads obtained from the DDES method are consistent with the flow physics revealed by experimental data (Geissler et al., 1997) in terms of the significant differences in the aerodynamic loads observed among different pitching cycles, whilst the URANS is incapable of capturing this. In such situation, the presented DDES results are obtained using the phase-averaged values to reduce phase error.



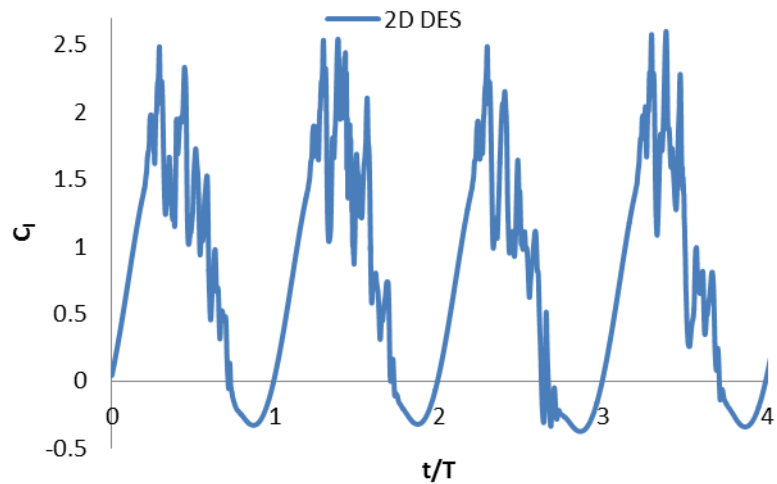
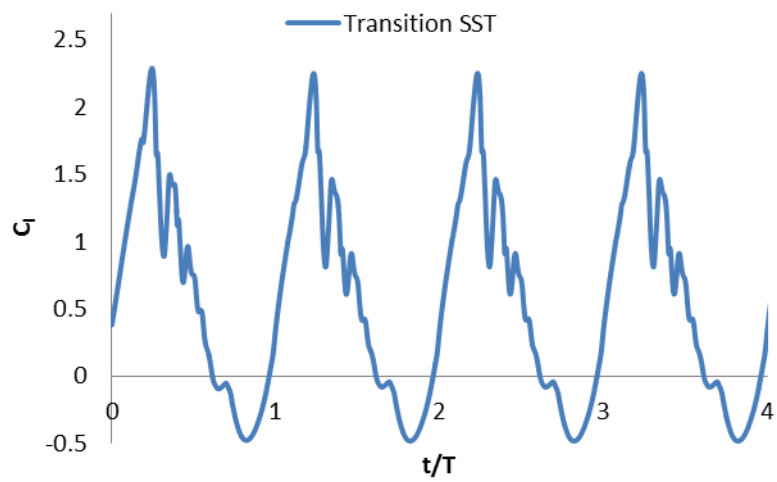
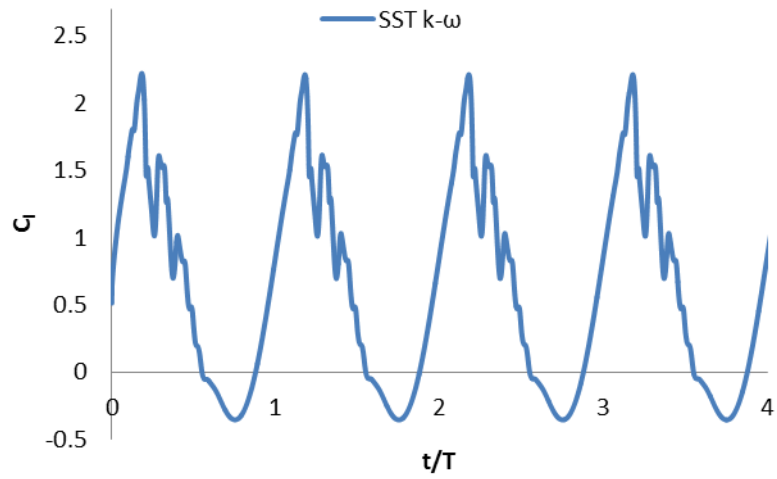


Figure 3-4 History of the lift coefficient for the pitching NACA0012 airfoil

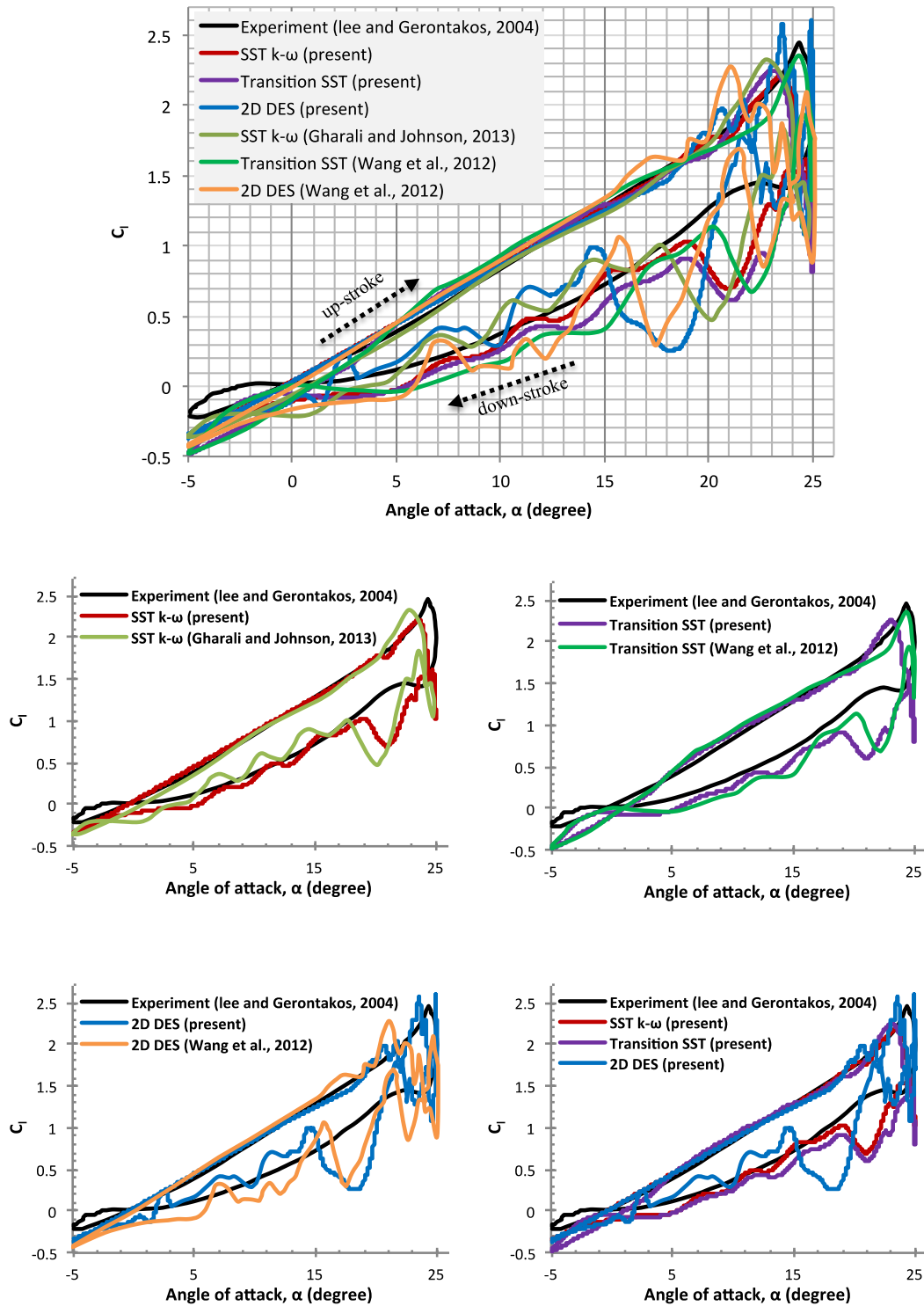


Figure 3-5 Comparison of the lift coefficient hysteresis loops of the pitching NACA0012 airfoil between current and previous results using various models

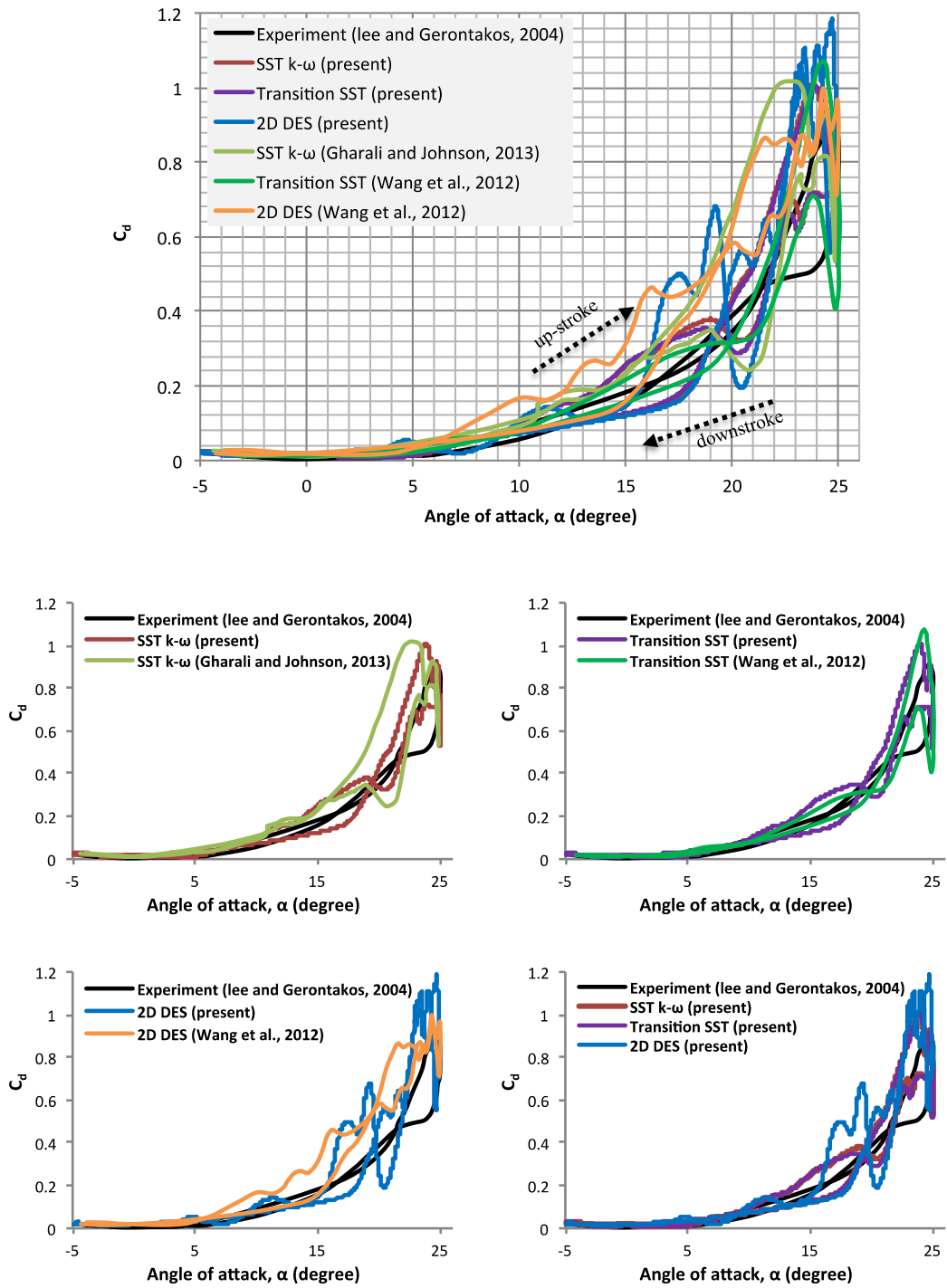


Figure 3-6 Comparison of the drag coefficient hysteresis loops of the pitching NACA0012 airfoil between current and previous results using various models

The predicted lift stall seems occur earlier than the experimental results for all the simulation results as shown in Table 3-3. Compared to the experimental results, the present numerical simulation results advance the stall point by no more than  $1.6^\circ$ . Except for the present SST  $k - \omega$  based DDES result which presents an over-prediction of the lift peak by 5.7%, all the other simulation results show under-prediction of the lift peak by less than 9.4%, showing that all the present numerical simulations can predict the lift peak with relatively good accuracy. Compared to the SST  $k - \omega$  based DDES result of Wang et al. (2012) which predicts a slightly earlier stall point ( $\alpha = 21.03^\circ$ ) than that observed in the experiment and fails to capture the peak of the lift coefficient, the present SST  $k - \omega$  based DDES result give better performance by the refinement of boundary layer grids. However, the present Transition SST simulation shows a too sharp drop-off of lift coefficient shortly after the lift stall occurs, this also occurs by the Transition SST simulation of Wang et al. (2012), presenting an over-prediction of the intensity of the stall which significantly affects the prediction of the subsequent flow-reattachment in the down-stroke phase.

Table 3-3 Occurrence of Lift Stall

	Occurrence of lift stall	
	$\alpha$	$C_l$
Experiment	$24.7^\circ$	2.44
SST $k - \omega$ (present)	$23.5^\circ$	2.21
Transition SST (present)	$23.1^\circ$	2.25
SST $k - \omega$ based DDES (present)	$23.5^\circ$	2.58
SST $k - \omega$ (Gharali and Johnson, 2013)	$22.75^\circ$	2.33
Transition SST (Wang et al., 2012)	$24.2^\circ$	2.36
SST $k - \omega$ based DDES (Wang et al., 2012)	$21.03^\circ$	2.28

In the down-stroke phase, with the decreasing of the angle of attack, all the calculations are showing a fluctuated lift force and not in good agreement with experimental data as the up-stroke phase. This is because the post-stall flow structure consisting of vortex rolling and shedding in the down-stroke phase is much more

complicated than that prior to the stall in the up-stroke phase, and is hard to be well captured by the turbulence models.

Although results of the down-stroke phase are not as good as the up-stroke phase, they are still in relatively good agreement with experimental data when  $\alpha \leq 15^\circ$ . The computed lift coefficient from the Transition SST model jumps back quickly from the over-predicted intensity of stall and then follows the tendency of the experimental curve well. The SST  $k - \omega$  model presents a fairly good consistency with the experimental data. The SST  $k - \omega$  based DDES model presents a fluctuated prediction of the lift force from blade oscillating cycle to cycle for the down-stroke, but averaged values of lift coefficient from the consecutive cycles presents a fairly good consistency with the experimental data. The inaccuracy result indicates that the advantage of DES in capturing 2-D characteristics of vortex is not revealed well by using in 2-D flow field.

All the present simulation results in down-stroke improve slightly compared to the results published by Gharali and Johnson (2013) and Wang et al. (2012), indicating that turbulence models are sensitive to grid, and grid refinement is essential to get better results.

The simulated drag coefficient is shown in Figure 3-6. The results obtained by the SST  $k - \omega$  model and Transition SST model are in relatively good agreement with the experimental data. The SST  $k - \omega$  based DDES gives a significant overshoot especially in large angle of attack, showing that the SST  $k - \omega$  based DDES do not have much advantages in this 2-D case compared to URANS.

### **3.4.2 Flow structure of Dynamic Stall**

A detailed interpretation of the numerical results via the flow visualization of the flow field under deep dynamic stall is present in this section. Chronologies of the static pressure fields at different oscillating locations superimposed on the instantaneous streamlines are displayed in Figure 3-7 (using the SST  $k - \omega$  model), Figure 3-8 (using the Transition SST model), and Figure 3-9 (using the SST  $k - \omega$

based DDES model), respectively. The complicated vortex patterns formed during the stall process are also depicted through these figures.

Deep dynamic stall is characterized by the process of the formation and shedding of the Leading Edge Vortex (LEV) that carries a low-pressure wave sweeping over the aerofoil along the suction surface of the airfoil. This feature is well captured by the numerical models and can be demonstrated as following:

- a) In the early stage of up-stroke phase, the angle of attack is very low ( $-5^\circ \leq \alpha \leq 15^\circ$ ) and the flow is attached to the airfoil surface, except there are streamlines ending or reversed at the trailing edge of the airfoil surface which was also reported in the experimental results of Lee and Gerontakos (2004). This can be explained that the fluid particles adjacent to the airfoil always have the same velocities as the local oscillating airfoil surface, thus forms a very small and thin reversal layer over the trailing edge of the upper surface. The lift coefficient during this relatively stable stage is characterized by a roughly constant slope and increasing almost linearly as shown in Figure 3-5.
- b) With the increasing of angle of attack, a tiny bubble was found at the leading edge as can be seen in Figure 3-7  $\alpha = 16.65^\circ \uparrow$ , Figure 3-8  $\alpha = 15.17^\circ \uparrow$ , and Figure 3-9  $\alpha = 16.37^\circ \uparrow$  (here  $\uparrow$  means the up-stroke phase). Considering the relative low Reynolds number in this study, this bubble is confirmed as the Laminar Separation Bubble (LSB). The LSB grows in size with the angle of attack increasing and turned into a LEV with a low-pressure region within it. At  $\alpha = 22.78^\circ \uparrow$  in Figure 3-7, the LEV moves toward the trailing edge and grows to approximately half of the airfoil chord, this caused a sudden rise in the lift coefficient in Figure 3-5. Such a relationship between the position and size of LEV and the slop changing point of lift coefficient are also observed in Figure 3-8  $\alpha = 21.86^\circ \uparrow$  and Figure 3-9  $\alpha = 22.61^\circ \uparrow$ . It should be noted that at this stage, the reverse flow separation layer behind the LEV becomes thicker.

- c) Dynamic stall occurs when the LEV occupies more of the suction surface and reaches the trailing edge, see Figure 3-8  $\alpha = 23.36^\circ \uparrow$ , resulting in a maximum value of the lift coefficient. After stall, the LEV keeps growing in size, we can also observe that the front part of the LEV has broken into two small vortices as in Figure 3-7  $\alpha = 24.01^\circ \uparrow$  and Figure 3-9  $\alpha = 23.9^\circ \uparrow$ . Then during further convection of the LEV downstream, the LEV begins to detach from the airfoil suction surface and induces a Trailing Edge Vortex (TEV) from the low-pressure wave it bears. These phenomena cause a rise in the pressure on the upper surface and the lift coefficient decreases significantly. With the angle of attack increases to its maximum value ( $\alpha = 25^\circ$ ), the TEV grows and rolls up at the upper surface, and the LEV becomes obscure.
- d) When the airfoil oscillates to down-stroke phase, the TEV sheds to the wake before the small vortices in the leading edge grow, merge and occupy the suction surface creating a maximum peak of the lift coefficient. This second LEV then sheds and following the initialize of the second TEV. The process of this post stall stage repeats and is similar to the upstroke, but not exactly the same and shows more complexity. The down-stroke LEV is not as strong as the upstroke one and that the aerodynamic coefficients do not recover to the values at the stall point. Small vortices with higher pressure than the upstroke LEV are formed irregularly especially in the numerical simulation using SST  $k - \omega$  based DDES model in Figure 3-9. This explains that an accurate prediction of down-stroke phase may not be warranted.
- e) The flow becomes reattached to the airfoil since the angle of attack becomes very small and all the small vortices have disappeared. It still can be observed that the flow is not fully attached because of the thin reverse flow layer in the trailing edge.

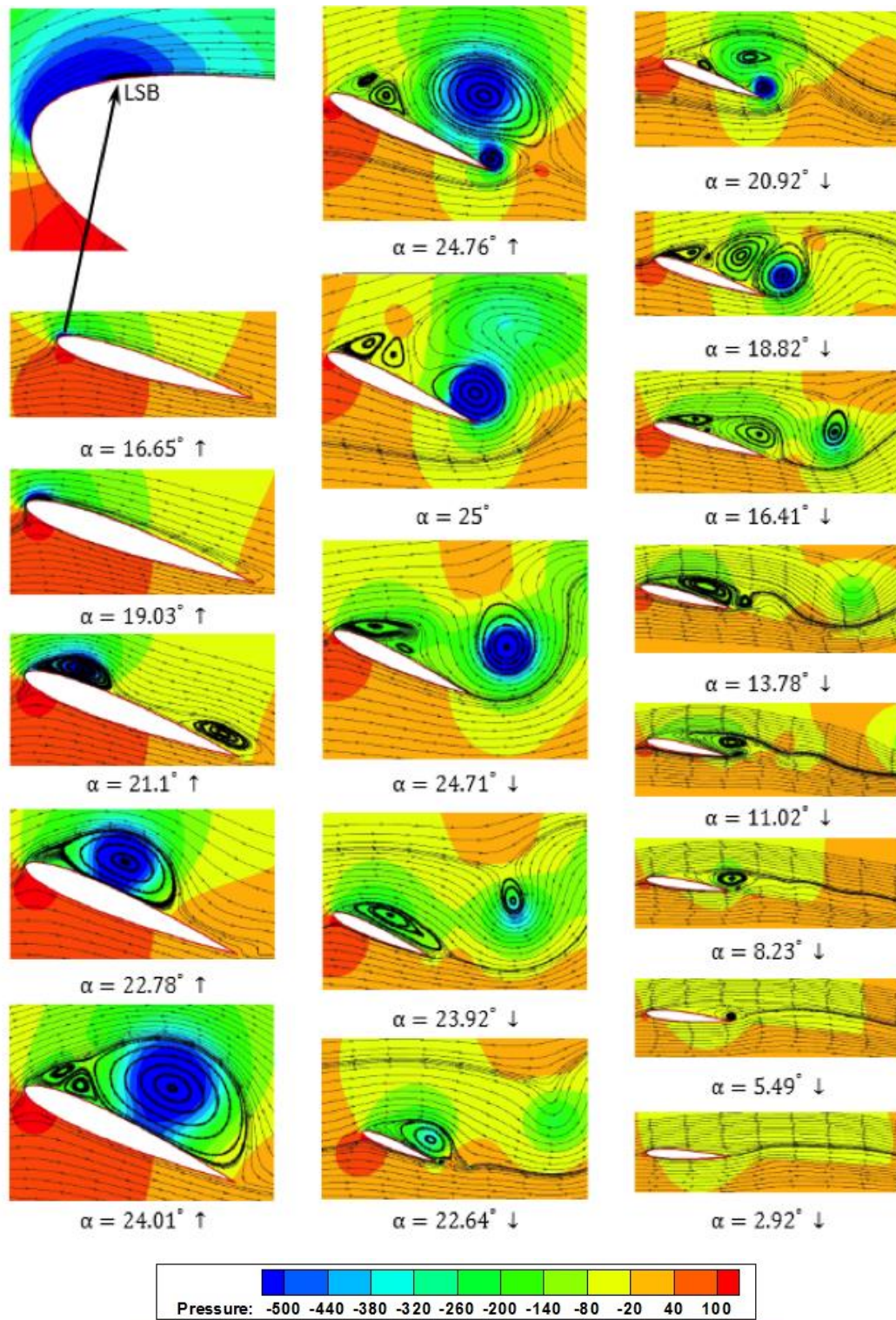


Figure 3-7 Pressure field superimposed on the instantaneous streamlines computed using the SST  $k - \omega$  model



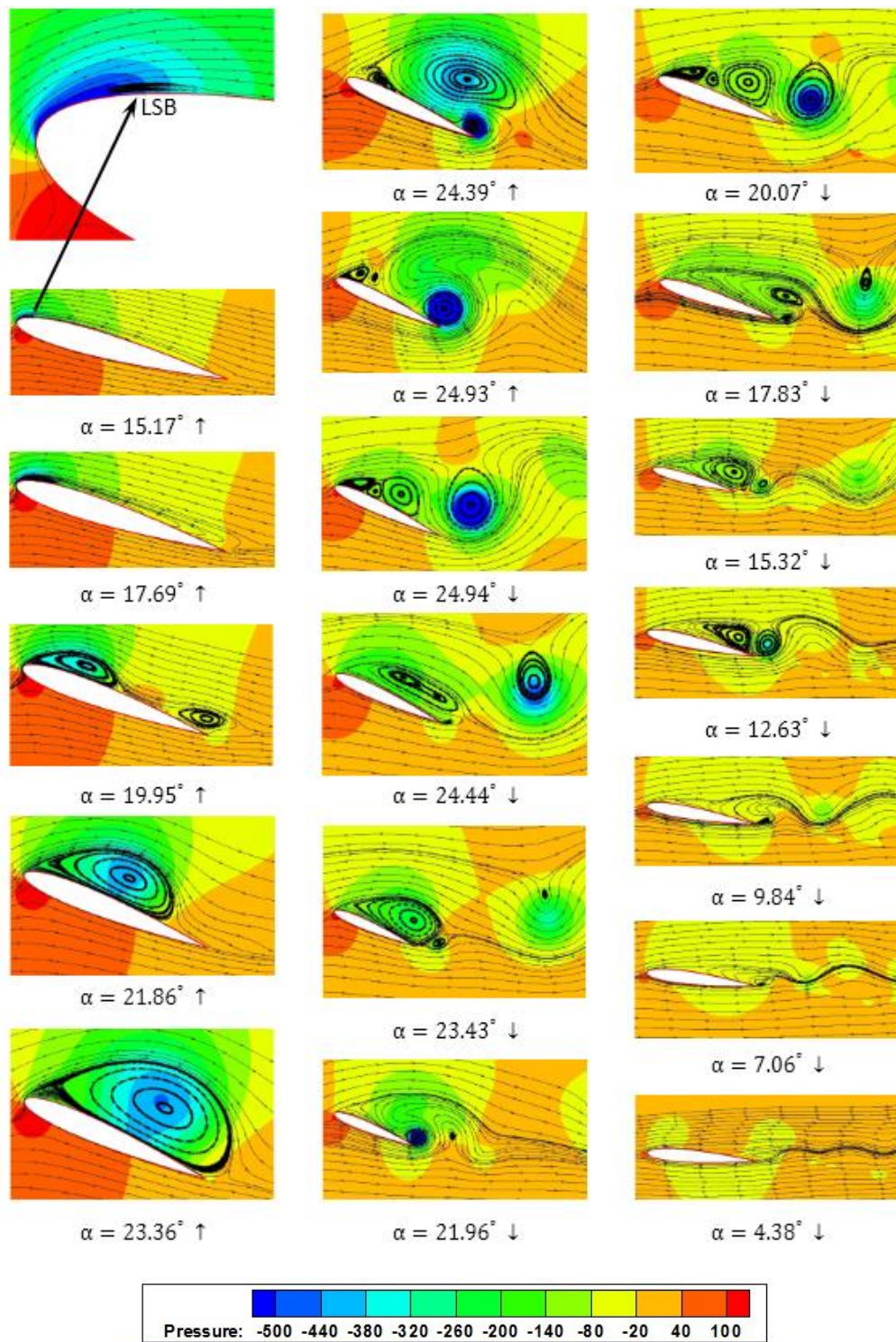


Figure 3-8 Pressure field superimposed on the instantaneous streamlines computed using the Transition SST model

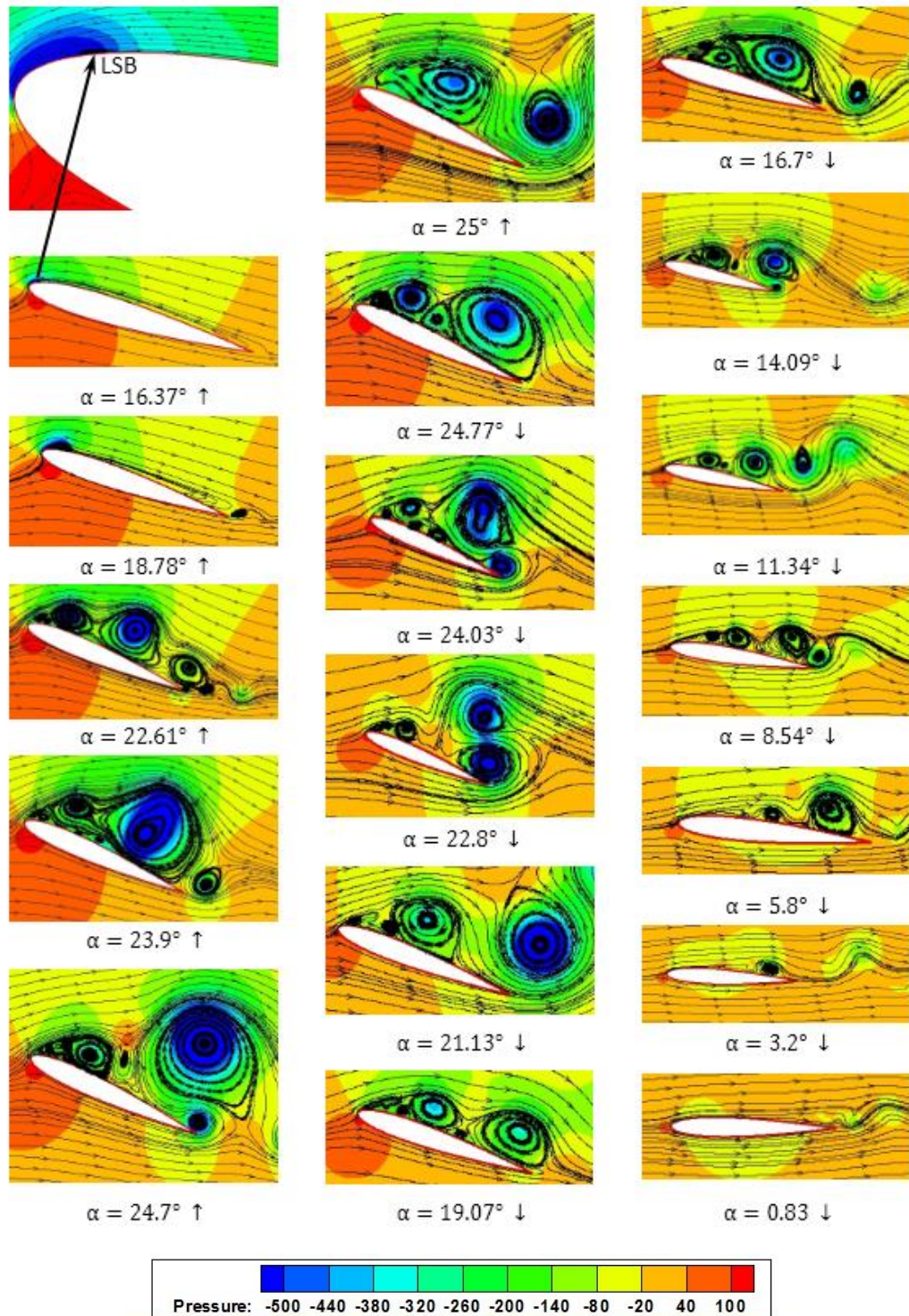


Figure 3-9 Pressure field superimposed on the instantaneous streamlines computed using the SST  $k - \omega$  based DDES model

In general, the SST  $k - \omega$  based DDES presents much more complicated flow structures as shown in Figure 3-9, involving a more complex system of vortices. The continuous generating and shedding of these vortices can be a reasonable answer for the fluctuation of the aerodynamic load in using SST  $k - \omega$  based DDES. Although in the down-stroke phase the flow structure of the numerical results have some common characteristics, it is not clear if they revealed the real flow field as the aerodynamic load in the post-stall stage is not accurately predicted compared to experimental results.

### 3.5 Summary

In this chapter, fluid flow over a NACA 0012 airfoil pitching in low Reynolds number region is numerically simulated by using the SST  $k - \omega$  model coupling with a low-Reynolds number correction, Transition SST model and the SST  $k - \omega$  based DDES model. The instantaneous cyclical aerodynamic forces and associated flow structure around the airfoil, including boundary layer transitions have been numerically revealed. Based on the presented results and analysis, the following conclusions can be obtained:

- The dynamic stall process as shown in Figure 2-15 has been well captured for each case studied in this chapter.
- Unlike the results of Wang et al. (2010a), the present numerical results of the SST  $k - \omega$  model coupling with a low-Reynolds number correction is in good agreement with the experimental data, and well captured the boundary layer transition, indicating grid refinement have significant effects on the SST  $k - \omega$  calculation results.
- In general the Transition SST model can predict the experimental data with reasonable accuracy.
- The DDES model does not show much improvement in 2-D application.

- The results show that there is a strong correlation between the lift coefficient curve and the development of the LEV for the specific case studied. Since the LEV originates from the LSB, the accurate modelling of the boundary layer transition process is crucial in simulating the low Re dynamic stall phenomena.

Based on the experience of turbulence modelling and dynamic stall process analysis gained from this chapter, 3-D simulation of a scaled HATT blade will be performed to understand the dynamic stall effects on blade loading. Grid generation for 3-D simulation is even more difficult because of the complicated geometry features. Experience from 2-D dynamic stall analysis will benefit the grid refining process in 3-D simulation, e.g. local grid refinement will be applied on the blade surface near the leading edge and trailing edge on the suction side for high fidelity turbine performance prediction. The SST  $k - \omega$  model and DDES model will be applied in 3-D simulation and corresponding results will be compared with experimental data. However, it should be noted that even with the current available HPC computer powers, performing 3-D DES type simulations of the dynamic stall process for engineering applications, which require substantially fine grid and temporal steps, is very computationally demanding.

# Chapter 4 CFD Methodology for HATT

## Blade Hydrodynamics Modelling

---

### 4.1 Model Turbine and Experimental Setup

To validate CFD results against experimental data, care must be taken to ensure that the same geometry and boundary conditions are used. The turbine experiments were conducted at the Kelvin Hydrodynamic Laboratory at University of Strathclyde in UK. The still water tank has a working length of 76 m and width of 4.6 m; the water level was maintained at 2.23 m. In the experimental tests, a notionally 1/20<sup>th</sup> scale model of a horizontal axis, tri-bladed test turbine was constructed and tested in the towing tank, as shown in Figure 4-1. The turbine had rotor and hub diameters of 0.78 m and 0.12 m respectively. The blades have a non-uniform profile, with the chord and twist varying along the span. The geometry of blade sections conforms to the 24% thick (defined with respect to the local chord), laminar-flow NERL S814 airfoil. This blade profile was specifically designed for the root section of small wind turbines (Somers, 1997) and was deemed to provide a sufficient degree of rigidity such that hydro-elastic effects on the blades of the model tidal turbine could be neglected. Negligible elastic deformation of the blades when loaded was confirmed during initial trials. For all the tests the rotor was 0.7 m below the mean free water surface. During operation, the out-of-plane bending moment from one of the rotor blades was captured by water proof strain gauge, which was instrumented on the blade root at a radius of  $r_{sg} = 36mm$  from the rotor axis.

In order to achieve a controllable unsteady flow that is uniform over the rotor plane and at an appropriate level of complexity, the experiments were designed to superimpose an unsteady surging motion upon a steady forward speed in calm water in the towing tank. In the experimental setup, a main carriage was moving forward with constant speed represented the mean velocity of the current. An auxiliary carriage mounted with the rotor was equipped on the main carriage, and was driven

by a linear actuator to generate a planar oscillatory motion to represent unsteady flow. A schematic of the test configuration is shown in Figure 4-2, and the turbine as installed on the two carriages can be observed in Figure 4-3.

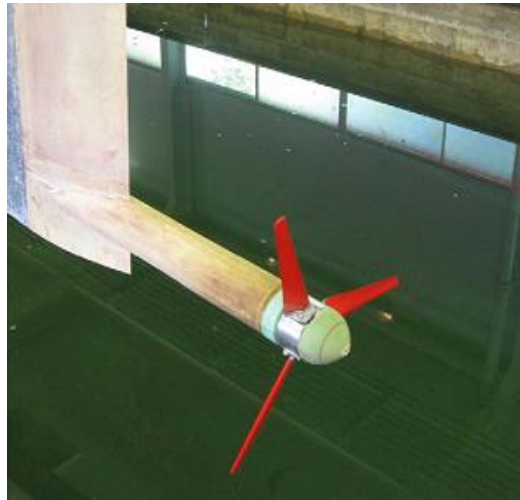


Figure 4-1 Turbine used in experiments by Milne et al. (2013)

A simple harmonic displacement time history of frequency  $f$  was input into the computer controlling the sub-carriage, such that the desired velocity upstream of the turbine  $u(t)$  was of the form

$$u(t) = U + \tilde{u}\sin(2\pi ft) \quad (4.1)$$

Where

- $U$  is the velocity of the main carriage (assumed constant)
- $\tilde{u}$  is the maximum velocity of the auxiliary carriage
- $f$  is the oscillatory frequency of the auxiliary carriage
- $t$  is the instantaneous time

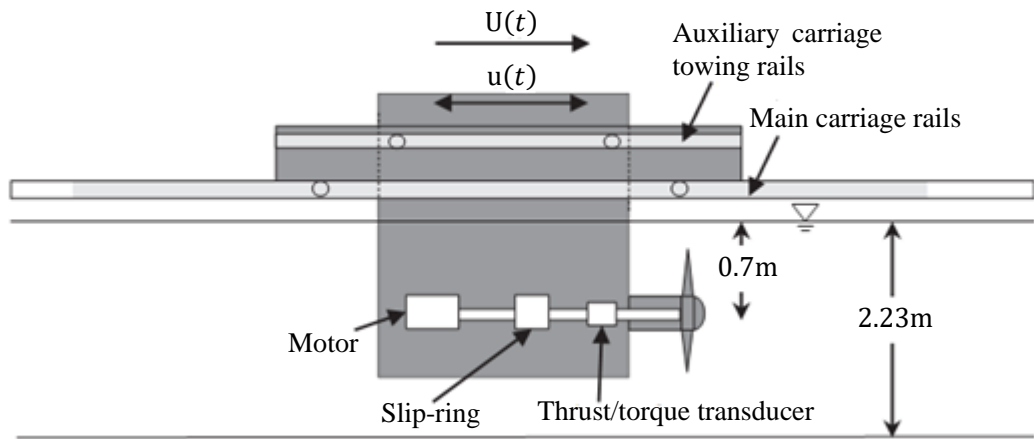


Figure 4-2 Schematic of the turbine and experimental test configuration

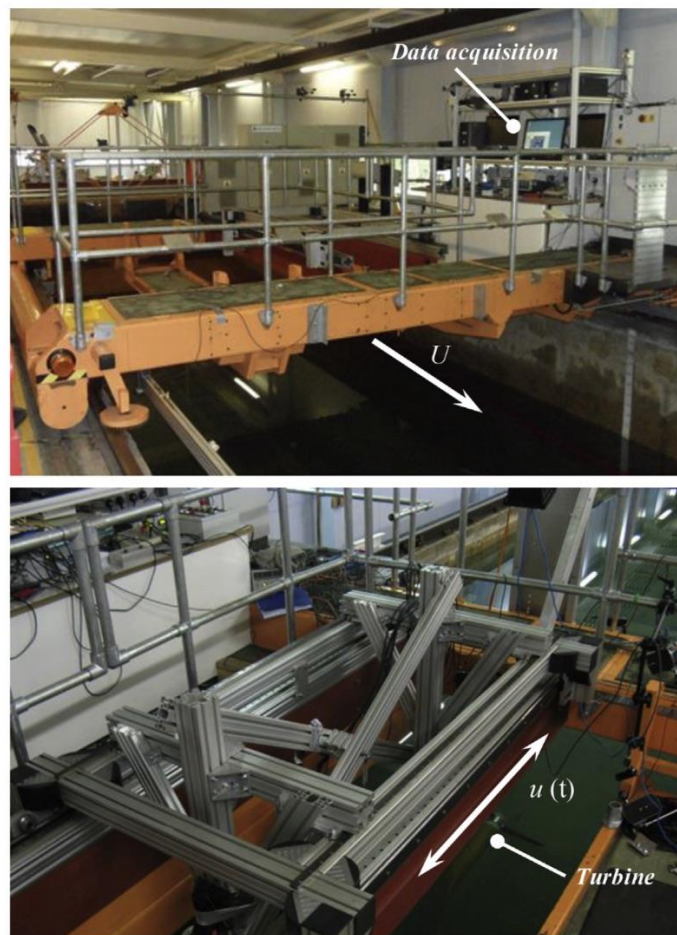


Figure 4-3 The turbine as installed, with the main and auxiliary carriages visible

A closed-loop digital controller was used to drive the rotor at constant rotational speed. To estimate the dominant experimental errors in the measurement of blade root out-of-plane bending moment, an uncertainty analysis was attempted and the uncertainties were considered to be sufficiently small for the purposes of the analyses presented herein in this study. The blockage of the rotor based on the projected frontal area was relatively low at 4.7%. For the turbine used by Bahaj et al. (2007), where the blockage in the towing tank was 8%, the thrust was estimated as being 5% greater than for unblocked conditions. Therefore, given the blockage was relatively low for the present tests, the blockage effects on the loads are expected to be relatively small and no blockage correction was applied.

Steady velocity experiments were implemented as an initial step in quantifying the role of unsteadiness, in providing a base line from which to reconstruct a quasi-steady based response with no acceleration component. The tests were performed at constant rotor speeds between 67 rpm and 96 rpm and the main carriage speeds between  $U = 0.45 - 1.01$  m/s. These speeds are equivalent to full scale speeds  $U_{FS} = 2 - 4.5$  m/s by using Froude number based scaling, in which  $U_{FS} = U\sqrt{h_{FS}/h}$ , where  $h$  is the water depth and it is assumed  $h_{FS}/h = 20$ .

For the oscillatory experiments, in an effort to ensure that the results of the experimental study are applicable to the tidal turbine industry, the axial velocity oscillations need to be carefully selected. Whelan (2010) has indicated that large waves with periods of 9 s may induce velocity fluctuations of up to 2 m/s. Milne et al. (2013) showed that the turbulence intensity at a typical tidal turbine site is of the order of 10-15%, with dominant time scales of 6-10 s. Applying Froude based scaling, the frequencies of interest here range from  $f = 0.45$  Hz to 1.56 Hz. The maximum oscillatory velocity  $\tilde{u}$  can be achieved by multiplying the mean upstream velocity  $U$  by Current number  $\mu$  ( $\mu = \tilde{u}/U$ ), where the Current numbers ranging from 0.1 to 0.3 are akin to the turbulence intensity and provides a means of scaling the oscillatory velocity amplitudes. Unsteady blade section hydrodynamics was typically characterized by the reduced frequency  $\kappa$ , with values ranging from 0.01 to 0.07 likely to be experienced by a full-scale turbine at 0.75R. Therefore, the axial



velocity oscillations tested in the study were representative of those likely to be imposed on a tidal turbine operating in the presence of surface waves and large-scale turbulence.

The sensitivity to both the oscillation frequency and maximum oscillation velocity was analyzed at two mean-tip-speed ratios of  $\lambda=3.6$  and  $\lambda=4.1$ , where the mean flow velocity and mean rotor speed were fixed at two groups, of  $U=0.78$  m/s,  $n=73$  rpm and  $U=0.84$  m/s,  $n = 84$  rpm. These operating points were located at either side of the point of maximum power in steady flow Milne et al. (2013), and were therefore deemed to be of most interest for tidal turbine designers. The investigations were conducted by varying one parameter at a time whilst maintaining the others nominally constant, to aid the inference of the underlying hydrodynamic phenomena.

## 4.2 Coordinates and Geometry

The horizontal axis rotor was described in a global Cartesian coordinate system with origin located at the rotor hub centre. As can be seen in Figure 4-4, the negative z-axis was the rotational axis with a rotor revolving in the clockwise direction. The original 3-D design drawing of the tidal turbine rotor as installed in the experimental tests has been generated using the CAD software Rhino. In the original geometry, there were too many details involving the installation of blades and water strain gages. The rectangular hydrofoil shaped blade root was connected to a small circular platform built in the hub, which results in small and irregular gaps between structure surfaces, raises difficulties in generating high quality grid. For the numerical simulations two adjustments with respect to the original geometry description have been made. Firstly, the geometry of the hub was replaced with a smooth cylinder connected with two smooth nosecones at each bottom, and the original small components were ignored. The second adjustment was in the joint area between the blade and the hub, where the blade root was extended to connection with hub. Figure 4-5 shows the adjusted geometry that was used for this thesis. According to the uncertainty study of Otto et al. (2012), the influence of these geometry adjustments on the numerical results is considered ignorable.

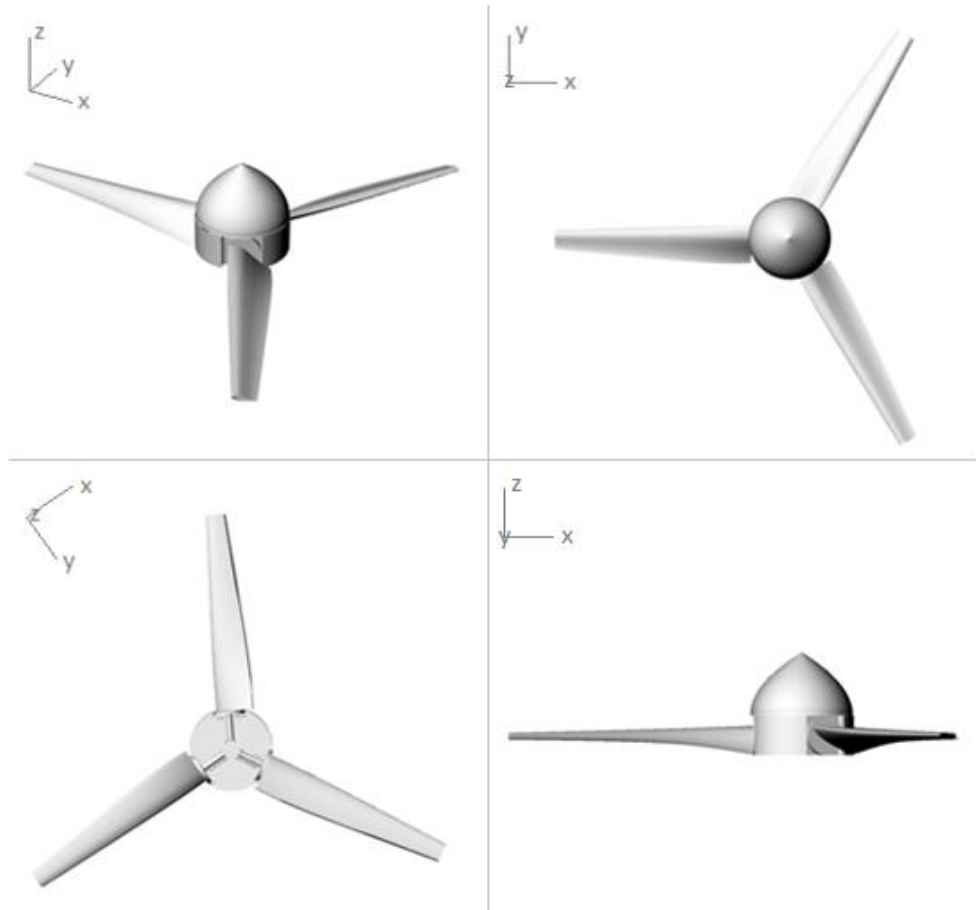


Figure 4-4 Original geometry of the turbine rotor

The substructure used in the experiment was neglected from the CFD analysis because the rotor is located far in front of it. This simplification approach has been widely used within the wind industry as a compromise between accuracy and computational costs, for instance by Zahle et al. (2009). Kang et al. (2012) has investigated the effects of removing the substructure and nozzle on a tidal turbine, where the conclusion is that this simplification could affect the wake behaviour to some extent but the effects on the blade forces are ignorable. The differences on the computed torque were almost identical with and without the substructure, probably due to the fact that the pressure field on the blades is not significantly affected and hence not affecting the torque and thrust. Since the unsteady blade load is the main

objective of this article, removing the substructure is therefore assumed to be a valid geometric simplification.

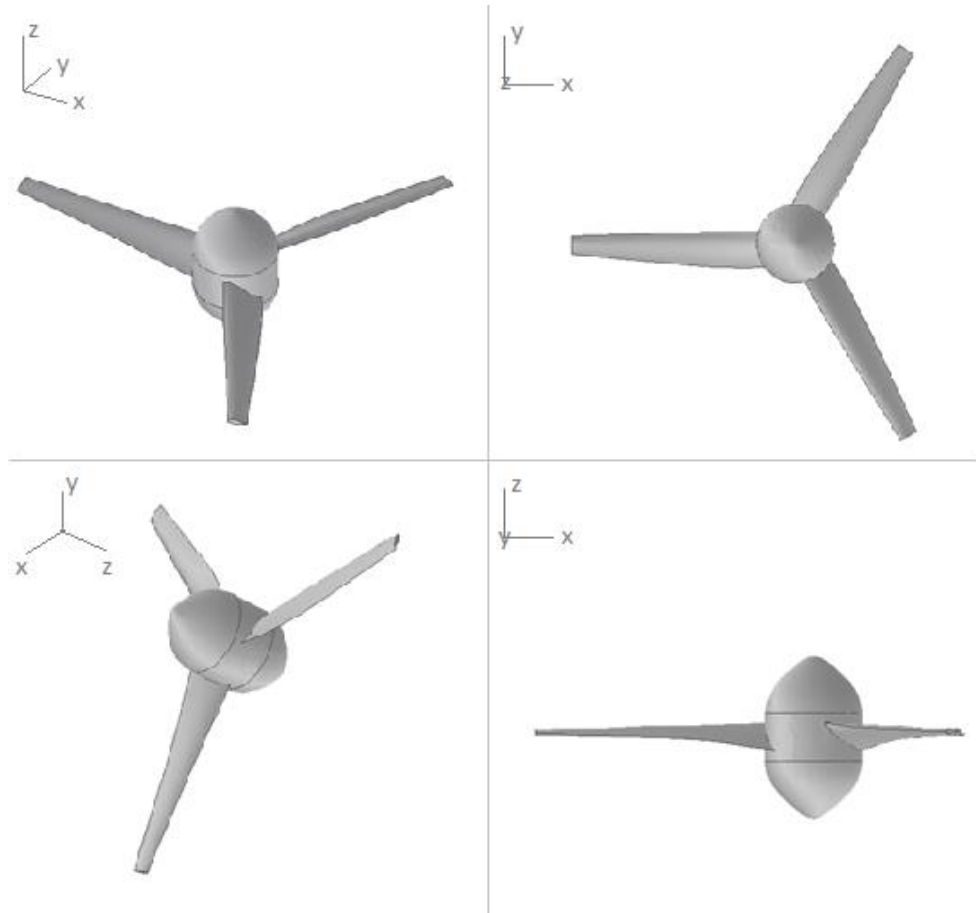


Figure 4-5 Adjusted geometry of the turbine rotor

### 4.3 Computational Domain

A cylindrical computational domain was implemented to be able to use a rotating MRF approach with varying angular velocity without an expensive and unnecessary re-meshing process. Because the inflow was uniform and the rotor blades were periodically located, the 120-degree periodicity advantage of a one-third model was used to minimize the computational cost, i.e., only one blade was meshed. Accordingly, the computational domain consists of a single blade and on third of the

hub, placed in a large one third-cylinder background domain with a periodic boundary condition in the azimuthal direction as shown in Figure 4.6.

In order to correctly reproduce hydrodynamic phenomena, some fundamental criteria should be considered in choosing a suitable size of the computational domain. First of all, the far boundaries of the computational domain had to be suitable for reproducing turbine rotation without wall effects. On the other hand, the domain had to be optimized to take into account the requirements of correct gridding. Too small a domain would not provide good enough grid generation, while too large a domain would lead to an unnecessary increase in the number of cells and hence in the computational time (Lanzafame et al., 2013).

The computational domain extent in the present study was a length of  $9D$  and a radius of  $3D$ , where  $D$  represented the turbine diameter. The inlet and outlet boundaries were located at  $3D$  upstream and  $6D$  downstream, respectively. The sizes of the domain also match that in Lee et al. (2012) and Park et al. (2013). The blockage of the rotor based on the frontal area of this computational domain was 33%, which was much higher than the experimental data. According to the numerical results of blockage ratio effects on HATT by Chime and Malte (2014), power extraction would be under predicted at high blockage ratio, and the under prediction of power extraction increases as the blockage ratio is raised. This inaccuracy was also found in the results of present study as discussed in the following chapters. Even so, the size of current computational domain is considered reasonable, as the flow physics of the HATT hydrodynamic performance were well captured and the computational time was highly reduced considering the complexity of the study.

The whole domain was divided into two sub-domains: the inner-domain includes the rotor blade and was surrounded by the outer-domain, as described in Figure 4-7. Grid generation within these two domains were applied separately. Since ANSYS Fluent provides solutions for non-conformal interfaces, the grid distributions on the boundaries where the sub-domains meets are not required to be the same as each other. By using this approach, different range of geometric scales between the rotor

and computational domain are neglected in order to take care of the local geometric scales for all those different “levels”. The relatively huge outer-domain with a regular geometry pattern can be filled with hexahedral cells to get a high quality solution and decrease the calculation load. While the grid generation for the relatively small inner-domain is difficult and time consuming due to consideration of the simulation accuracy and the complex geometry. Details of the grid generation procedures will be discussed later.

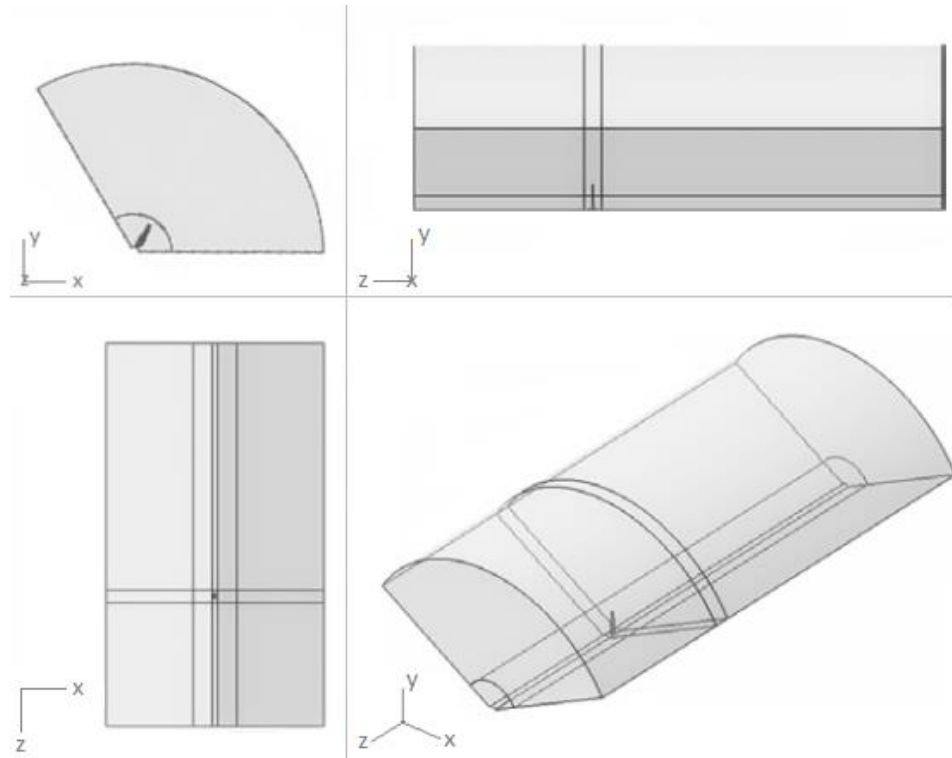


Figure 4-6 Computational domain for the CFD analysis

## 4.4 Boundary Conditions

In order to complete the CFD problem solved here, it is necessary to appropriately specify the flow variables on the boundaries of the chosen physical model. Figure 4-7 shows the boundary conditions and domain extents designed for the present CFD procedure. No-slip conditions were employed on all the surfaces of the rotor. At the

inlet of the computational domain, the flow speed was specified and the pressure was set to zero gradient. The turbulent intensity according to the experiments was specified as 10% and uniform at the inlet of the computational domain, whilst turbulent viscosity ratio was 10. At the outlet of the computational domain, the pressure was predefined and the velocity was set to zero gradient. To reduce flow recirculation on the far-field boundaries and to improve the stability of the numerical solution, a slip (or symmetry) boundary condition was applied across the curved cylindrical surface of the outer domain. At the two rectangular sides of the computational domain, to take the rotational flow into account, the flow across the two opposite planes was assumed to be identical, i.e., periodic. Between the sub-domain near the turbine blade and outer sub-domains, non-matching interfaces were defined and simple linear interpolation was used for the transition of the solution through the interface.

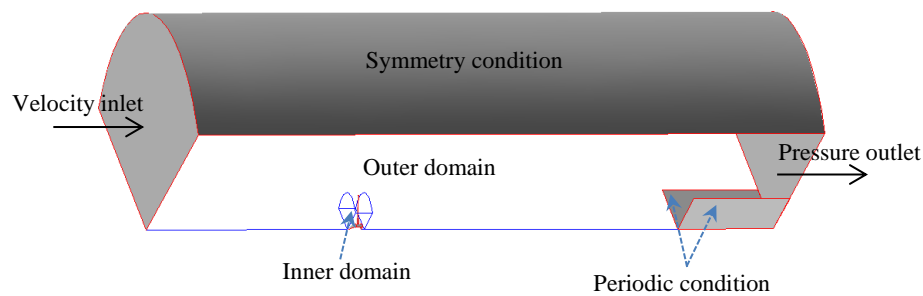


Figure 4-7 Boundary conditions and domain extents

## 4.5 Grid Generation

Grid generation is the most important pre-processing step for CFD simulations. The accuracy of the numerical solution of partial differential equations depends on the quality of the grid used in the discretization of the problem, especially on the grid density, the distribution of the grid points, and the quality of the elements connecting these points. An optimal grid is one that accurately captures all the main features of

the geometry and the fluid flow with the minimum number of grid points and elements.

Grids are either structured or unstructured. A structured grid is a collection of regular repeating elements. Such grids are generally represented by quadrilateral elements in 2-D and hexahedral elements in 3-D. An unstructured grid consists of arbitrarily shaped elements that do not have any regularity among them. This type of grid is generally represented by triangles in 2-D and tetrahedrons in 3-D geometries. Each grid type has its own advantages and disadvantages. Structured grids have been shown to be superior in capturing viscous flows adjacent to solid surfaces due to their orthogonality and somewhat insensitivity to large aspect ratios in the dominant flow direction. However, the process of structured grid generation is a manually intensive and time-consuming task, especially around complicated geometries and can lead to over refinement away from the bodies. In addition, because grid lines must eventually extend across the entire grid-block or domain to maintain certain block structures that are required for some solution methods, additional grid points are often placed in regions where they are not required to resolve the flow accurately. On the other hand, triangular elements can cover any regular or irregular domain efficiently, but stretching these elements affects the accuracy of the solution to a large extent. As a result, when using unstructured grids, care must be taken to insure the grid quality (e.g. grid element skewness, grid element aspect ratio, and grid density) does not adversely impact the accuracy of the numerical solution.

Hybrid grids were preferred for the majority of the CFD studies relevant with wind/tidal turbine performance that has been reported to date (e.g., Digraskar, 2010; Lee et al., 2012; Holst et al., 2012; Park et al., 2013). In the hybrid approach, the sub-domain include the turbine blade is always filled with unstructured tetrahedral cells due to the complex geometry pattern, while other sub-domains with simple geometry are filled with hexahedral cells for high quality solution there. The main advantage of using hybrid grid is their ability to resolve finely around very complex geometric topologies and reduce the computational effort to some extent.

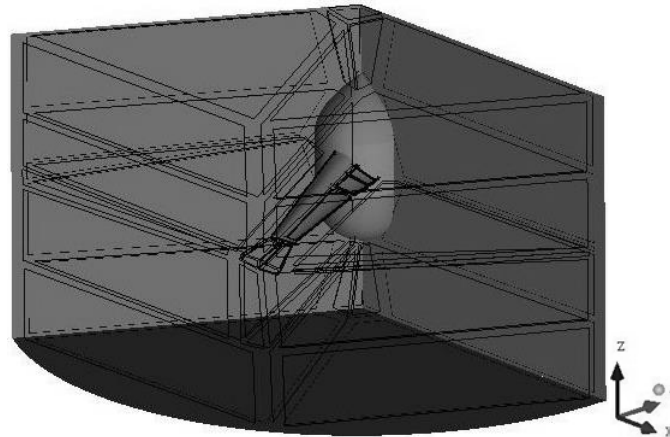
In addition to the type of grid, some other aspects involved in grid generation should also be considered for optimum problem solution. On a rotating turbine blade, the high speed flow occurs near the blade tip and low-pressure appears at the leading edge and blade tip on the suction side, thus for high fidelity turbine performance prediction, accurate prediction of the low-pressure on the suction side is required and a finer grid on the blade surface near the leading edge, trailing edge and blade tip need to be applied. It is also of great importance that applying an appropriate  $y^+$  value in combination with a given turbulence modelling approach, thus there is a need to refine the wall layer grid based on the desired  $y^+$  value.

In the present study, both hybrid grid and fully structured hexahedral cell grid were tested and compared to compromise between the desired accuracy and solution cost. The commercial software Gambit was used to generate hybrid mesh, while the commercial software ANSYS ICEM was used to generate fully structured grid. Grid refinement tests run on different grid sizes and configurations are carried out to match the converged numerical solution as closely as possible to experimental data. Six grids with different nodes number, namely the fine/medium/coarse hybrid/structured grid separately, are generated for using in the grid refinement tests and time step studies. The results of the grid refinement study will be discussed in chapter 5.

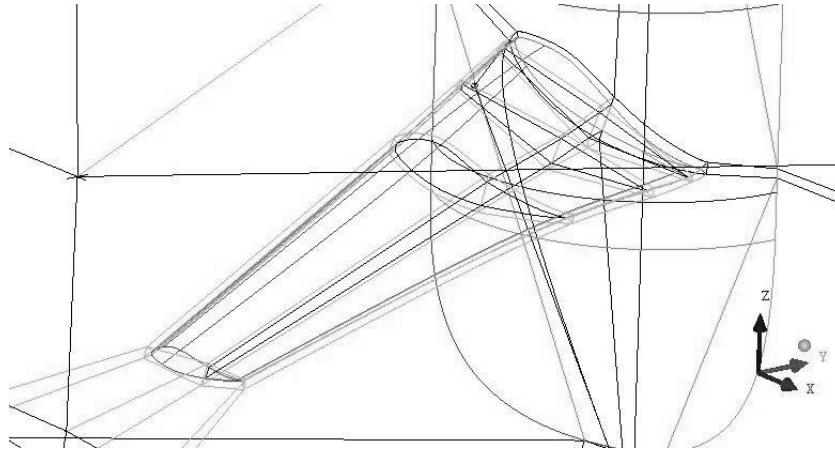
ANSYS ICEM uses the concept of a separate blocking framework that is subdivided to represent the topology of the model and then associated to the specific model geometry. A Conformal grid (traditionally structured hexahedral cells) is generated within each of the blocks and fit to the geometry. Figure 4-8 shows the multi-block structure in the inner-domain. Since the geometry is a little complicated which contains a twisted turbine blade with a sharp trailing edge, extensive blocking skill is required to generate the block topology. Several blocks are generated along the blade spanwise direction and associated with the blade geometry to diminish the grid element skewness induced by blade twist. To generate hexahedral grids around the sharp trailing edge, two block edges parallel and close with each other are applied and associated with the trailing edge. After the multi-block topology is settled, grid



sizes can be arranged according to requirements. Figure 4-9 shows the multi-block structure and hexahedral grids in the outer-domain. This domain has a simple and regular structure that is much easier to apply the hexahedral grids. Figure 4-10 shows the surface grids around the blade of the medium structured grid. Grids around the boundary layer, leading edge, trailing edge, blade root, and blade tip are refined in order to accurately simulate the hydrodynamic performance of the blade.



(a)



(b)

Figure 4-8 (a) Inner-domain blocking using ANSYS ICEM (b) blocks edges around the blade

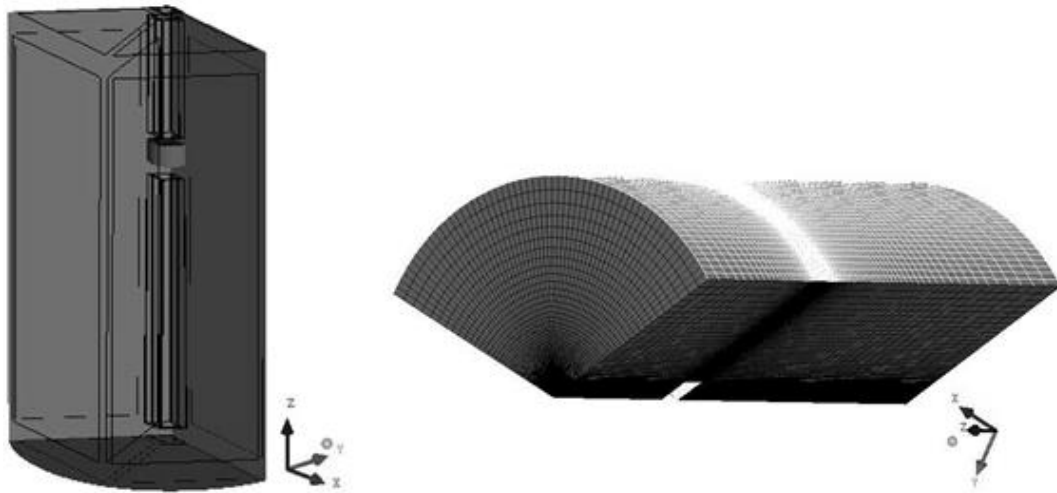


Figure 4-9 Outer-domain blocking and structured grids using ANSYS ICEM

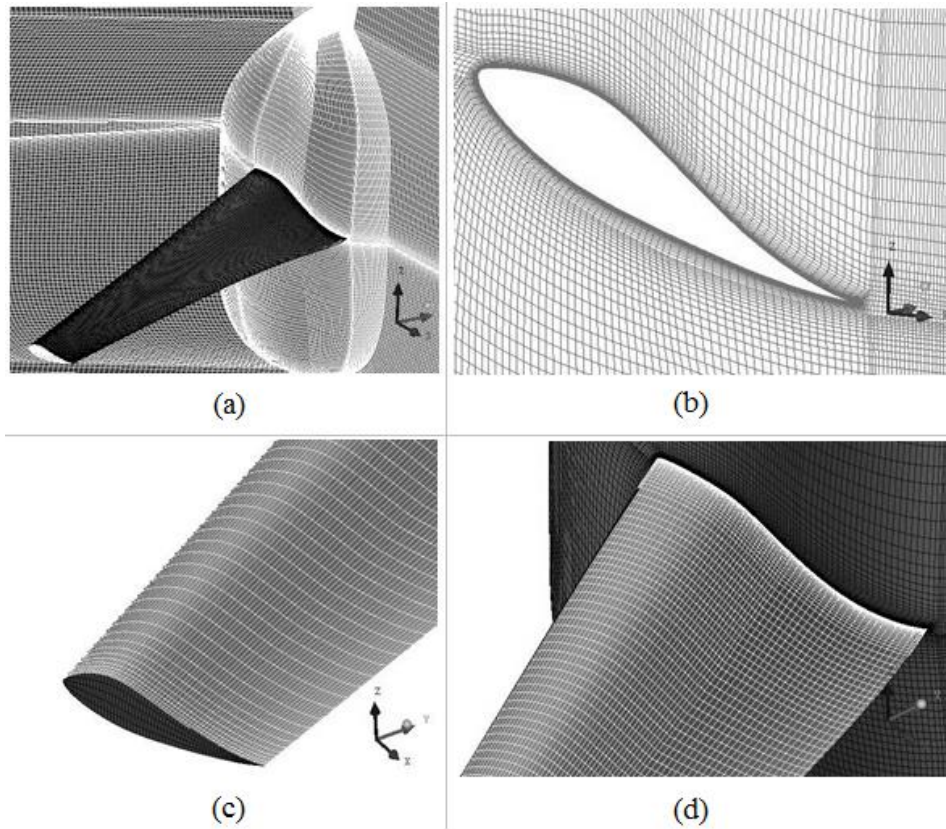


Figure 4-10 Structured surface grid around the blade using ANSYS ICEM (a) grids around the computational geometry (b) boundary layer grids (c) grids at the blade tip (d) grids at the blade root

It should be noted that, for the cases studied in this thesis, stall was expected to happen at high angle of attack. Thus it is necessary to generate a fine grid capturing both the far field and the near wall boundary layer, as this is essential to the accurate prediction of the forces and the separation phenomena. The grid was well resolved near to the wall, where a first layer thickness of  $5 \cdot 10^{-6}$  m and 28 inflation layers were used with a growth ratio of 1.15 for all the simulations. These settings were estimated to assure an acceptable expansion factor between inflation layer and domain-elements and  $y^+$  less than 1 with more than 10 nodes within the boundary layer at all times. Figure 4.11 shows the real wall  $y^+$  values distributed on the blade surfaces along the inflow direction, which was calculated from an unsteady inflow case and was plotted by ANSYS Fluent. It is shown that  $y^+$  is under 0.6 for much of the surface, with the maximum value of 1.3.

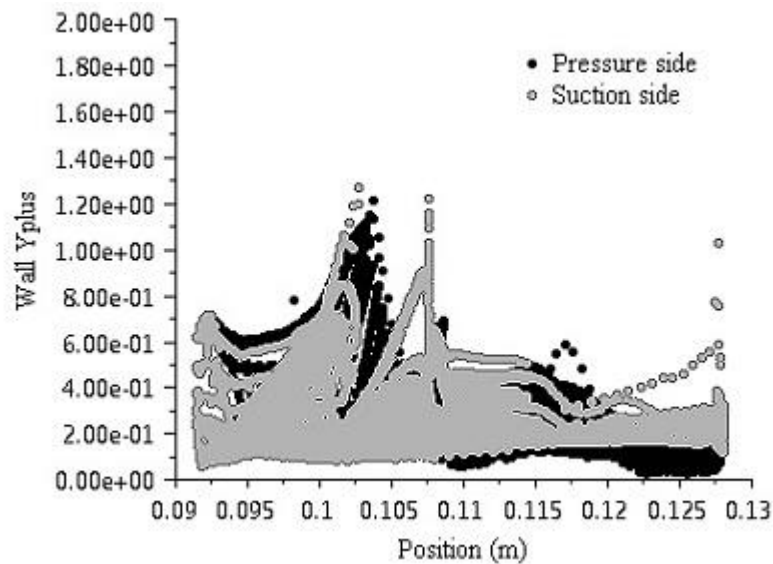


Figure 4-11 Wall  $y^+$  calculated by ANSYS Fluent from an unsteady inflow case of the model turbine

## 4.6 CFD Solver Setup

The numerical results presented in this work were obtained from time-dependent incompressible Reynolds averaged Navier–Stokes (RANS) simulations performed

with the commercial CFD software ANSYS Fluent by a finite-volume method. The rotation of the system was accomplished using a non-inertial rotational reference frame. The rotational speed was set in the frame motion at constant values of 73 rpm and 84 rpm, and the flow velocity ranging from 0.47-1.06 m/s was set in the velocity inlet boundary condition. The pressure based solver was employed and the segregated algorithm which solves the governing equations sequentially was chose to reduce the memory demand.

Table 4-1 Computational Conditions

Blade	The reference turbine using S814 airfoil	
Solver	Pressure-Based Transient Solver	
Fluid Material	Water liquid	
Flow Type	Incompressible Flow	
Temperature	298k	
Viscosity	0.001 kg/m-s	
Density	1000 kg/m <sup>3</sup>	
Flow Speed	0.47~1.06 m/s	
Moving Reference Frame	Frame motion (Constant rotational velocity of 73 rpm)	
Grid interfaces	Side (Periodic Boundary Condition), Circle (Default)	
Pressure-Velocity Coupling	SIMPLE	
Turbulent model	SST k – $\omega$	DDES
Spatial Discretization	<i>Gradient</i> Last Squares Cell Based <i>Pressure</i> PRESTO! <i>Momentum</i> Second Order Upwind <i>Turbulent Kinetic Energy</i> Second Order Upwind <i>Specific Dissipation Rate</i> Second Order Upwind	<i>Gradient</i> Last Squares Cell Based <i>Pressure</i> PRESTO! <i>Momentum</i> Bounded Central Differencing <i>Turbulent Kinetic Energy</i> Second Order Upwind <i>Specific Dissipation Rate</i> Second Order Upwind
Transient Formulation	Bounded Second Order Implicit	
Boundary condition	Velocity Inlet, Pressure Outlet, Periodic, Symmetry Stationary Wall with No Slip Shear Condition	

In terms of the settings of solution methods, the SIMPLE algorithm is employed for pressure-velocity coupling. The convective terms in the URANS equations are discretized with a second-order upwind scheme. The gradients of solution variables are discretised with the default Least-Squares Cell-Based approach, and the PRESTO! scheme is chosen for calculating cell-face pressures when using the pressure-based solver in FLUENT. The temporal term has been discretized with a Bounded Second Order Implicit scheme, with special care taken to make sure the time-step employed is small enough to obtain accurate numerical solutions. For DDES, the *SST k –  $\omega$*  model and the delayed DES option is applied for RANS calculation, the default Bounded Central Differencing scheme is adopted for momentum discretization. The computational conditions are summarized in table 4-1. To reduce the required time for transient simulations to reach a quasi-steady state, the simulations were initialized using the steady flow solution.

## **4.7 Summary**

This chapter discusses the pre-processing steps for the current CFD simulation, including preparing the geometry, defining the computational domain, specifying the boundary conditions, grid generation and the setup of CFD solver. The consideration of the CFD methodology was discussed in detail. It should be noted that the size of current computational domain caused high blockage ratio, which should be considered as one of the reasons for the inaccurate prediction of power extraction and hydrodynamic blade loads.



# Chapter 5 Methodology Validation

---

Before performing the CFD simulations over large amount of case studies, validation investigations were performed to give an impression of the accuracy of the applied methodology, namely, a grid refinement study, a time-step size study, and an evaluation of different turbulence models.

## 5.1 Grid Refinement Study

A grid independent test was carried out to verify that the grid resolution is sufficiently fine to give consistent results. Due to the complexity of the cases being studied, it is not easy to perform a strict grid refinement study, and the present check is more of a qualitative check. Both the hybrid and fully structured grid were used in performing the grid resolution study, each using three levels of grid resolution: a fine grid with 8.7 million nodes for hybrid grid and 4.8 million nodes for structured grid, a medium grid of 6.2 million nodes for hybrid grid and 1.6 million nodes for structured grid, and a coarse grid of 1.3 million nodes for hybrid grid and 0.7 million nodes for structured grid. The five turbine operating conditions presented in Table 5-1 were simulated under a steady inflow assumption using each computational grid. The turbulence model used for grid refinement study was the DDES model. And adaptive time step size for each simulation case has been used, allowing a Courant-Friedrichs-Lewy (CFL) number less than to 1. The results from these simulations were then compared with experimental data to study the influence of the grid resolution on the numerical solution.

To quantitatively evaluate the effect of grid resolution on the numerical solution, the blade in-plane bending moment coefficient  $C_{Mx}$  and out-of-plane bending moment coefficient  $C_{My}$  were calculated for each grid. Figures 5-1 and 5-2 present these quantities plotted verses tip-speed ratio. The relative differences between  $C_{Mx}$  and  $C_{My}$  predicted by the six grids with respect to the experimental results were presented in Table 5-2 and Table 5-3.

Both the hybrid grids and structured grids exhibit better results with increasing grid resolution. For the blade in-plane bending moment coefficient  $C_{Mx}$  predictions as is illustrated in Figure 5-1 and Table 5-2, the fine hybrid grid and fine structured grid results agree with experimental results well, with the error rates less than 20%. Since the value of  $C_{Mx}$  is in a small numerical range, the 20% error rate can be recognized as a small numerical error. It can also be concluded that further increasing the grid resolution would not bring many benefits for the blade in-plane bending moment coefficient  $C_{Mx}$  prediction, because tiny improvement of the  $C_{Mx}$  value will cause large computational load in CFD calculations. Although other grids do not perform very well in the simulation results, e.g., with highest error rate of 65.10%, they show results with good agreements in trends with experimental data.

Predictions of the blade root out-of-plane bending moment  $C_{My}$  are also sensitive to the grid resolution (see Figure 5-2 and Table 5-3). The fine hybrid grid and fine structured grid give the best performance here by having the largest absolute error rate of 9.57%. The results also show that the medium and coarse hybrid grids are under predicting the blade root out-of-plane bending moment  $C_{My}$ , while other grids are over predicting  $C_{My}$ .

Above all, for the steady inflow case, the current fine hybrid and fine structured grids appear to be sufficient to give good results. The fine hybrid grid has the advantage of its convenient grid generation scheme but is computationally demanding. The fine structured grid has reduced workload, however extensive experience in grid generation method is required.

A further refinement study for the unsteady oscillatory inflow case is necessary as the flow structure during operation is much more complicated than that in the steady inflow case. The oscillating inflow velocity causes variations of the angle of attack in the blade section, which give rise to dynamic stall on the blade and significantly affect the blade load. It has been reported in Chapter 3 that in 2-D pitching airfoil simulation, the post-stall flow structure consisting of vortex rolling and shedding is



hard to be capture well, thus grid refinement is especially important in 3-D simulation.

Table 5-1 Operating conditions with steady inflow

Operating condition	Rotor speed (rpm)	Flow velocity (m/s)	Blade pitch (deg)
Case 1	84	1.06	0
Case 2	84	0.943	0
Case 3	84	0.827	0
Case 4	84	0.709	0
Case 5	84	0.59	0
Case 6	84	0.471	0

Table 5-2 The relative difference of  $C_{Mx}$  to the experimental results

Grid	Case 1	Case 2	Case 3	Case 4	Case 5	Case 6
<b>Fine hybrid</b>	8.68%	6.15%	10.46%	17.68%	19.86%	-13.82%
<b>Medium hybrid</b>	-10.87%	-13.08%	-1.66%	19.83%	47.13%	-28.84%
<b>Coarse hybrid</b>	-19.97%	-18.48%	-3.37%	18.41%	61.54%	-34.08%
<b>Fine structured</b>	-5.36%	-7.81%	-1.62%	-5.93%	-17.14%	4.77%
<b>Medium structured</b>	-14.52%	-13.28%	-8.95%	-9.26%	-65.10%	23.83%
<b>Coarse structured</b>	-31.82%	-26.47%	-15.16%	-17.20%	-42.32%	40.58%

Table 5-3 The relative difference of  $C_{My}$  to the experimental results

Grid	Case 1	Case 2	Case 3	Case 4	Case 5	Case 6
<b>Fine hybrid</b>	4.19%	2.27%	5.71%	5.54%	2.48%	-4.14%
<b>Medium hybrid</b>	3.99%	-5.32%	-4.69%	-6.19%	-7.47%	-9.57%
<b>Coarse hybrid</b>	-4.56%	-7.17%	-6.18%	-5.94%	-8.29%	-7.74%
<b>Fine structured</b>	1.41%	0.38%	2.03%	2.58%	0.74%	-1.20%
<b>Medium structured</b>	2.10%	1.36%	3.70%	4.21%	2.40%	-1.93%
<b>Coarse structured</b>	2.08%	1.47%	5.60%	5.89%	3.57%	1.35%

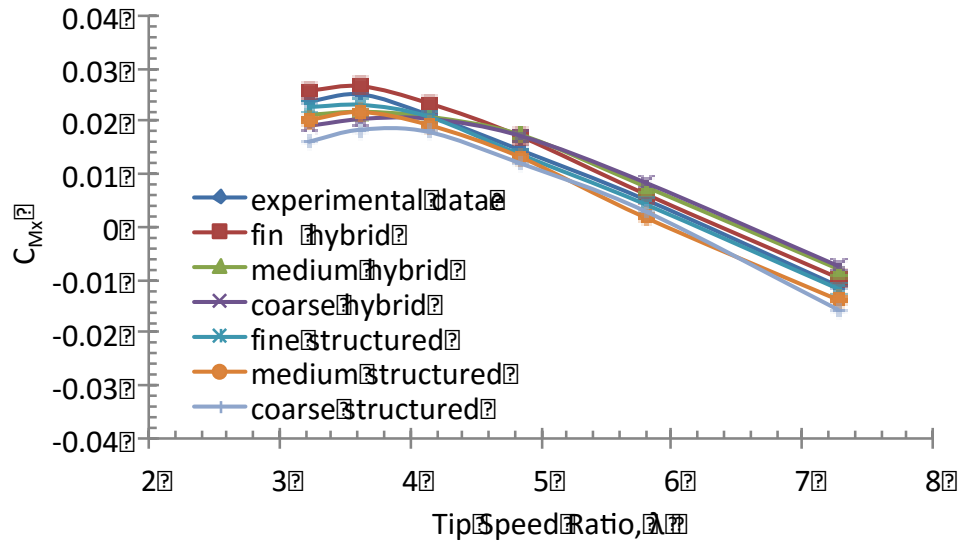


Figure 5-1 Blade in-plane bending moment coefficient  $C_{Mx}$  for steady inflow case

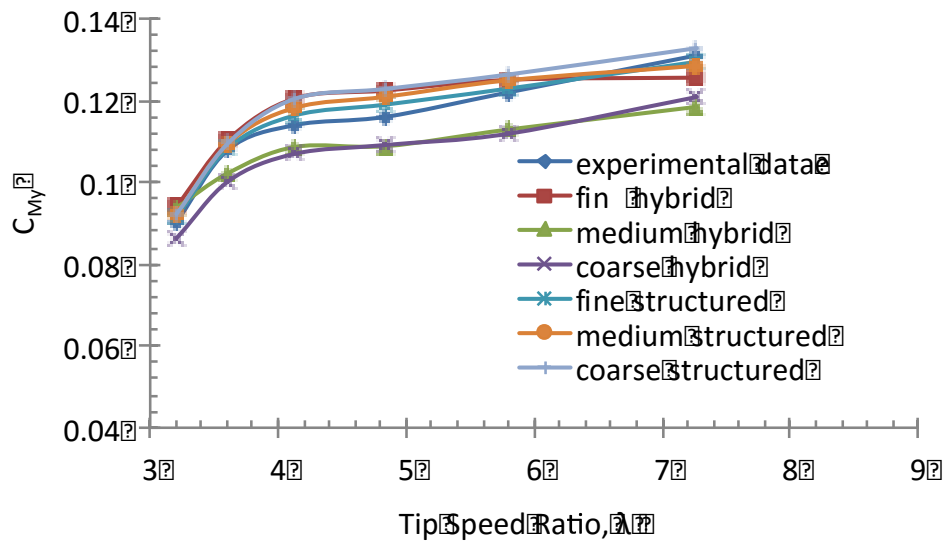


Figure 5-2 Blade out-of-plane bending moment coefficient  $C_{My}$  for steady inflow case

A finer structured grid with 6.1 million hexahedral nodes was generated and applied in the grid refinement study of oscillatory inflow case, results were compared with experimental data and the results obtained by the fine structured grid and fine hybrid grid. In the case studied, the rotating velocity was 73 rpm, the mean flow speed was

$U = 0.78$  m/s, the oscillating frequency was  $f = 0.5$  Hz, and the current number was  $\mu = 0.2$ .

Figure 5-3 shows the comparison of out-of-plane bending moment coefficient  $C_{My}$  in a non-dimensional time cycle. It was indicated by Leishman (2006) and Milne (2013) that, the bending moment responses exhibit phenomena associated with separated flow and dynamic stall with three key stages involved in the process, as highlighted by 1–3 in the experimental data in Figure 5-3: at stage 1, the bending moment exceeds the point of stall observed for steady flow conditions, and there is a delay in the onset of flow separation. Stage 2 indicates the point of full separation, and the onset of flow reattachment is illustrated as stage 3. All of the three test grids successfully captured the characteristic of the three stages during dynamic stall. However, the fine hybrid grid under predicted  $C_{My}$  with a relatively large difference. Both of the fine structured grid and finer structured grid can predict the onset of flow separation at stage 1 accurately. In stage 2, the fine structured grid captures the timestamp of full separation accurately but with an under-predicted  $C_{My}$ . The finer structured grid reveals an under-predicted  $C_{My}$  as well and catches the timestamp of full separation a little earlier. In Stage 3, both of the fine structured grid and finer structured grid capture the flow reattachment state earlier than experimental result, but the predicted  $C_{My}$  values are in good agreement with experiment. Since the rotor is operating at constant speed, the contribution from the forces out of phase with velocity alone can be inferred qualitatively by plotting the bending moment as a function of tip-speed ratio  $\lambda$ , in the form of hysteresis loops. The hysteresis loops in Figure 5-4 clearly demonstrate that at high tip-speed ratio, the fine structured grid and finer structured grid can predict  $C_{My}$  at a good degree of agreement, however, at low tip-speed ratio, the fine structured grid gives relatively better result although both of the grids exhibit under predictions of the  $C_{My}$ .

According to the aforementioned grid refinement test results, the fine structured grid with 4.8 million hexahedral nodes is assumed to be enough to capture the flow physics for both of the steady inflow case and unsteady oscillatory inflow case.

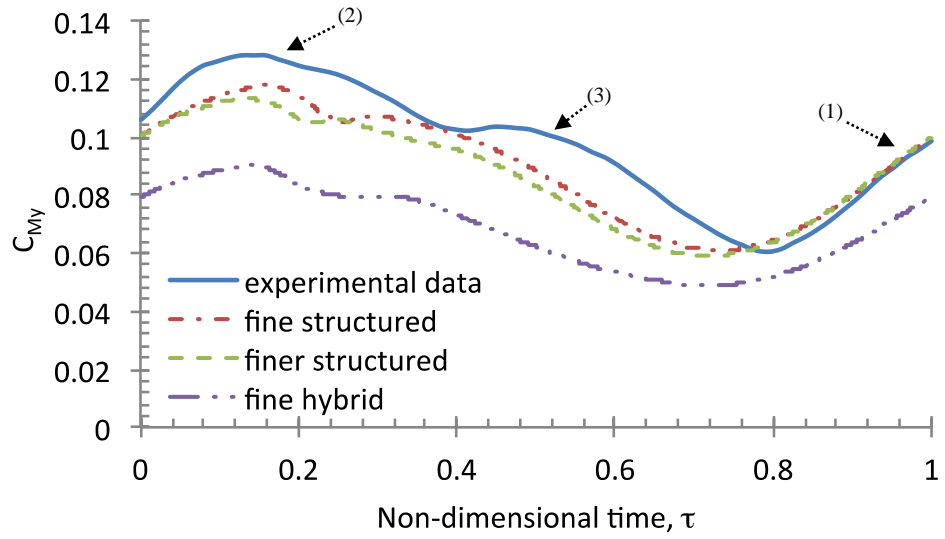


Figure 5-3 Non-dimensional time history of the out-of-plane bending moment  $C_{My}$  for oscillatory inflow case (operating condition:  $n = 73$  rpm,  $U = 0.78$  m/s,  $f = 0.5$  Hz,  $\mu = 0.2$ )

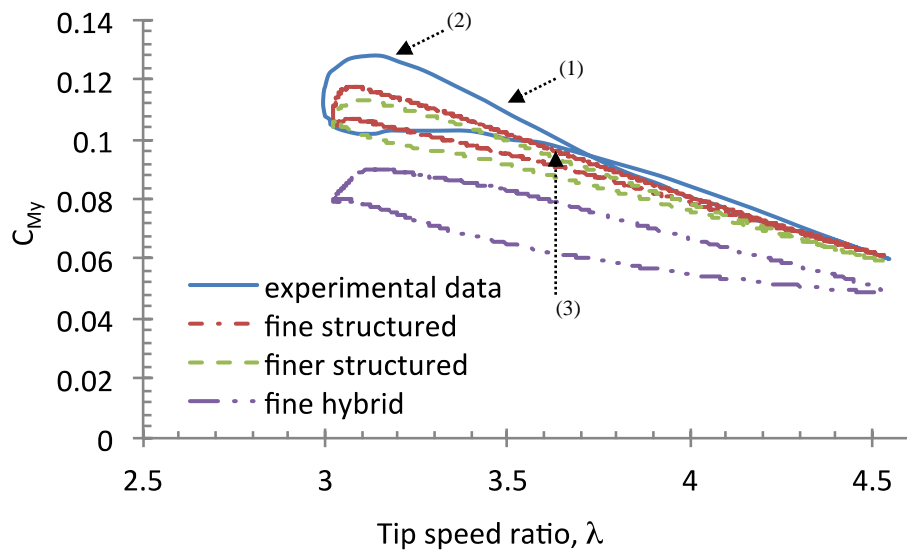


Figure 5-4 Out-of-plane bending moment coefficient  $C_{My}$  as a function of instantaneous tip-speed ratio for oscillatory inflow case (operating condition:  $n = 73$  rpm,  $U = 0.78$  m/s,  $f = 0.5$  Hz,  $\mu = 0.2$ )

## 5.2 Time Step Investigation

After having examined the influence of the grid resolution, the effect of changing the time step is studied. The steady inflow operating condition where the rotational speed is 84 rpm, and inflow velocity is 0.827 m/s was investigated for the time step study. With the hydrofoil chord varying from 0.064 m at the blade root to 0.035 m at the tip, a 0.827 m/s free stream velocity would give a time scale of 0.04 s for a chord passage at the tip and 0.08 s at the root. With a resolution of approximately 150 cells along the chordwise direction, a time step of 1/150 approximate a Courant-Friedrichs-Lewy (CFL) number of 1 in the critical region close to the hydrofoil, resulting in a time step of 0.0005 s. In the following simulations, computations were performed using time step sizes of 0.001 s, 0.0005 s, 0.0002 s, and 0.0001 s. These time steps correspond to 714, 1429, 3571, and 7143 time steps per rotor revolution, respectively. The DDES model and the fine structured grid were used for all the time step investigations. Table 5-4 shows the results from the time step study. The sizes of the larger computational time steps are found to have very little effect on the magnitude of out-of-plane bending moment  $C_{My}$  generated by the turbine. Computations using different time step sizes are also carried out for the same oscillatory inflow case as in the grid refinement study, the result by using the time step of 0.0005 s is shown in Figure 5-3, the results by using larger time step sizes of 0.0002 s and 0.0001 s do not make any apparent difference so are not shown here. Considering the lower computations cost of the smaller time step, it was decided to use a time step of 0.0005 s in all the computations in the following chapters.

Table 5-4 The results from the time step study

Time step size (s)	$C_{My}$
Experiment	0.114
0.001	0.1176
0.0005	0.1163
0.0002	0.1163
0.0001	0.1164

## 5.3 Turbulence Models

Having established the necessary grid resolution and time resolution to get sufficiently independent results, the turbulence modelling method was also studied to obtain the closest possible agreement with the experimental data. From the review of the 2-D dynamic stall study for the pitching NACA0012 airfoil in chapter 3, the SST  $k - \omega$  model, Transition SST model and the DDES model were reported to have the ability to accurately reveal the instantaneous cyclical aerodynamic forces and associated flow structure around the hydrofoil including boundary layer transitions. It was pointed in particular that with refined grid the SST  $k - \omega$  model could perform well in simulating dynamic stall. In the 3-D turbine blade simulations, the SST  $k - \omega$  model is expected to perform as well as the aforementioned DDES test results, so the turbulence modelling tests were only carried out for the oscillatory inflow case in this section.

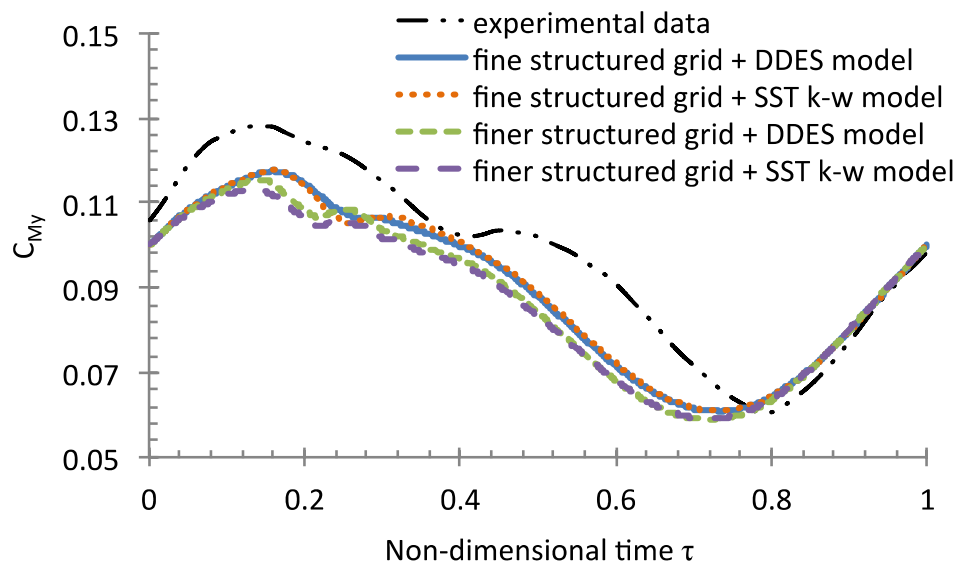


Figure 5-5 Non-dimensional time history of the out-of-plane bending moment coefficient  $C_{My}$  for oscillatory inflow case (operating condition:  $n = 73$  rpm,

$$U = 0.78 \text{ m/s}, f = 0.5 \text{ Hz}, \mu = 0.2)$$

With the same case as studied in the grid refinement test, the computational results by using the SST  $k - \omega$  model coupling with a low-Reynolds number correction are

shown in Figure 5-5. The computations were applied on both of the fine structured grid and finer structured grid in order to check the grid refinement effect on the SST  $k - \omega$  model results, and the calculating time step size was 0.0005 s. By comparing with the experimental result and DDES results, it is clearly to find the SST  $k - \omega$  model is capable of simulating the 3-D dynamic stall in agreement with the DDES results especially when the grid is reasonably refined. However, considering the DDES model was well tested in the grid refinement study and time step study, and it is more recommended for simulating the complex flow structure including continuous generating and shedding of vortices, in the following chapters the DDES model will be used in the numerical studies.

## 5.4 Summary

In this chapter, a series of grids, of which the density of the grid was further refined in turn in the near-blade flow region of greater importance, were assessed to examine the grid convergence. On the other hand, the time step size in the unsteady simulations, which is pertinent to the truncation error of the unsteady terms, has been carefully examined to ensure that a proper time step size is implemented. As a result, a fully structured grid with 4.8 million hexahedral nodes and a time step size of 0.0005 s are preferred for further case study. Although the present investigation failed to provide fully grid and time-step independent results, it was shown that the overall behaviour of the results were preserved even on finer grid and even for smaller time step. Based on these facts, we believe that the present results are representative for the current capability of state of the art CFD predictions. Moreover, even though the computations showed that changing the turbulence model from SST  $k - \omega$  to DDES only generated minor changes for the present configuration, all investigations in the following chapters were performed with the DDES model.

The steady flow cases were continued for approximately 4500 iterations and took approximately 30 hours per case on 4 CPUs, the simulations results were obtained from average value when computation perturbation were negligible. The unsteady flow computation took approximately 30 hours using 5 CPUs to complete one

oscillation cycle. The simulation results of the unsteady flow computation were obtained from the last periodic cycle. Due the complexity of the cases studied, the computational costs are considered acceptable.



# Chapter 6 Steady Flow Study

---

After the 3-D validation including the grid refinement study, time step study and turbulence modelling study, a number of cases were investigated to characterize the performance of the rotor and blade loads for steady inflow velocities. As stated earlier, stall is apparently to occur during the rotor operating cycles, thus these cases can be taken as an initial understanding of the role of flow unsteadiness. Furthermore, scaling effects of the model HATT were also investigated under the steady inflow velocities.

## 6.1 Performance Characteristics

The steady inflow cases studied in this chapter were performed at constant rotor speeds of 73 rpm, 84 rpm and 90 rpm and inflow velocity speed at  $U = 0.45-1.06$  m/s. Using the methodology discussed previously, the dimensionless coefficients of power  $C_p$ , thrust  $C_T$ , in-plane bending moment  $C_{Mx}$ , out-of-plane bending moment  $C_{My}$  as a function of tip-speed ratio  $\lambda$  were calculated as shown in Figure 6-1, Figure 6-2, Figure 6-3 and Figure 6-4, respectively. To reduce computational cost for the parametric test of tip-speed ratios, each simulation were performed in turn restarting from the previous results.

It is clearly to find that the optimum power coefficients are attained at the tip-speed ratio between approximately  $\lambda = 3$  and 4, with the value of  $C_p \approx 0.4$ , which is conform to the Betz limit. The performance of the rotor is characterized by a relatively steep decay in all the coefficients at low tip-speed ratios. While with the tip-speed ratio increases, the power and in-plane bending moment coefficients are experiencing a reduction trend, the thrust and out-of-plane bending moment coefficients are exhibiting an increasing tendency. The characteristics of the coefficients curves can be explained by analyzing the flow structures: Milne (2013) has reported that the stall effects are dominant within the low tip-speed ratios. The appearance of stall will cause reductions in lift and drag coefficient and thus

significantly reduce the power coefficient. At higher tip-speed ratios, a considerable amount of kinetic energy of the incoming flow is converted into large-scale turbulent motion, leading to the turbulent wake state, where the drag forces are dominant and causing the thrust increasing and power decreasing. Leishman (2006) has also indicated that this turbulent wake state is characterized by an enhancement in wake turbulence and aperiodicity, and the onset flow perceives the rotor as an increasingly solid disc.

At constant rotational speed, stall occurs at the lower tip-speed ratio means higher inflow velocity will induce stall. The turbine blades must not be run during flow speeds that are too high, since this may cause vibration that can shake the turbine into pieces. On the other hand, with lower flow velocities the turbine is not able to generate optimum power. The ways to solve these problems are using a pitch-controller on the blades or a stall-controller (which can be active or passive).

The coefficients also exhibit sensitivity to the rotational speed. The mean Reynolds number for a blade section at  $0.75R$  is predicted to vary from approximately 100,000 to 70,000 between rotor speeds of 90 rpm and 73 rpm. In lieu of airfoil data for these Reynolds numbers, it is postulated that the lift and drag performance of the foil would have reduced as the rotor speed is slowed, and the boundary layer nears a laminar flow regime. Laminar separation bubbles are also expected to be present on the airfoil surface, which will result in increased drag. The increase in the thrust and out-of-plane bending moment coefficients at high tip-speed ratios for the low rotor speed cases may be due to the influence of the turbulent wake state, where the thrust forces are more sensitive to global drag effects, rather than to the flow over the blade section.

Another discovery from the coefficients curves is that the magnitude of the out-of-plane bending moment coefficient is considerably larger than the in-plane component, which indicating that the dominance of the thrust forces over the gravitational and centrifugal inertia forces. The out-of-plane loads are hence only considered hereafter in the unsteady analysis presented in this thesis.

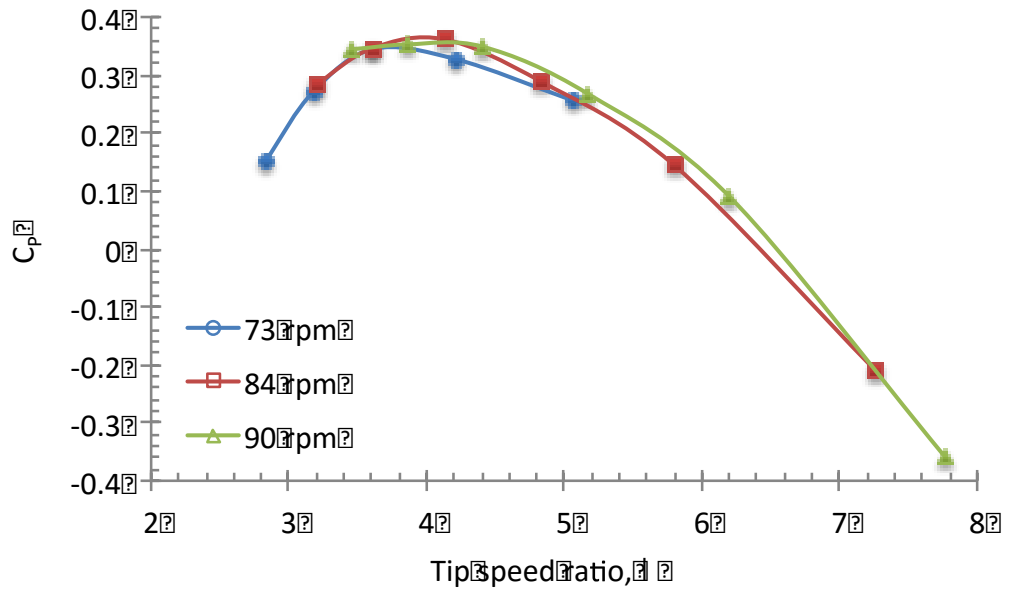


Figure 6-1 Power coefficients as a function of tip-speed ratio for steady inflow case

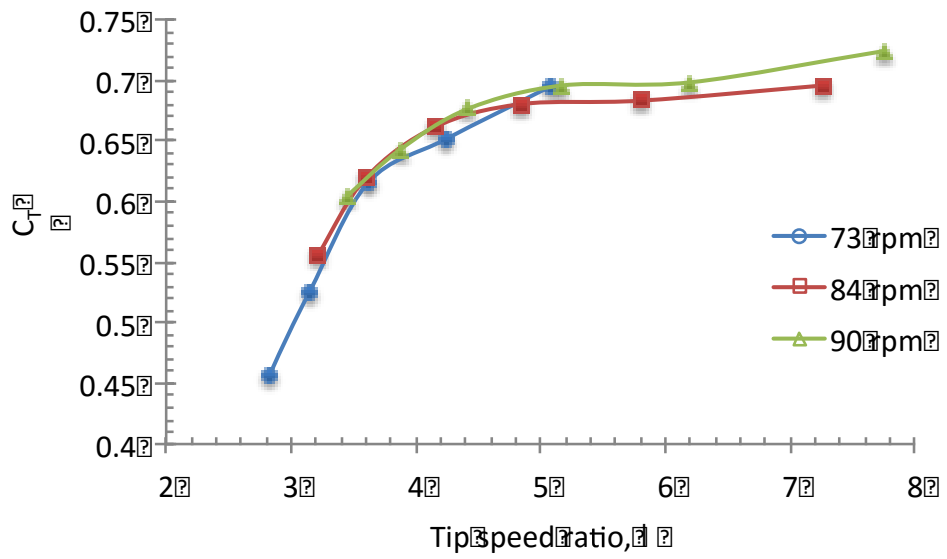


Figure 6-2 Thrust coefficients as a function of tip-speed ratio for steady inflow case

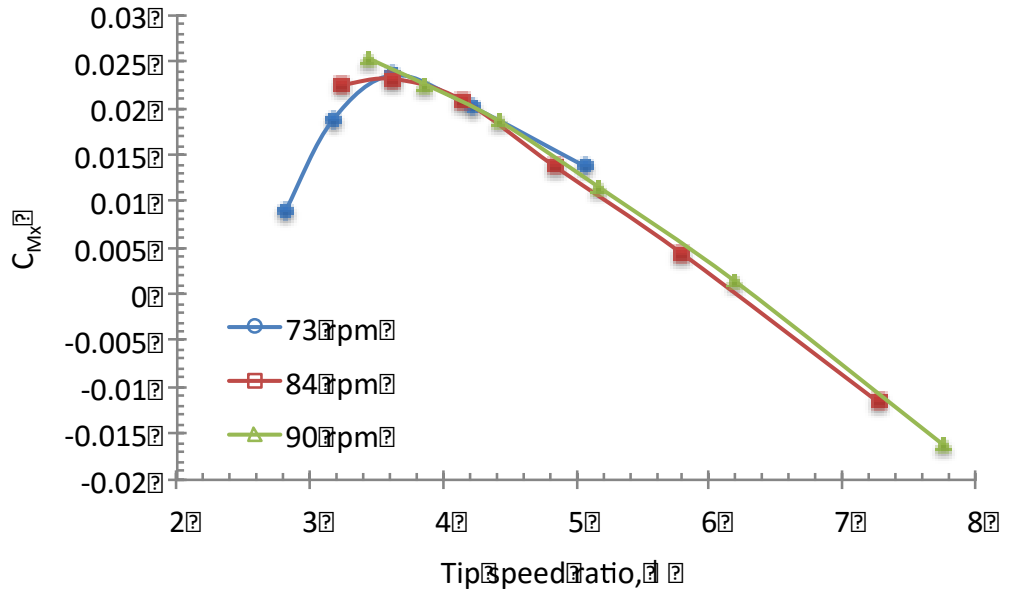


Figure 6-3 In-plane bending moment coefficients as a function of tip-speed ratio for steady inflow case

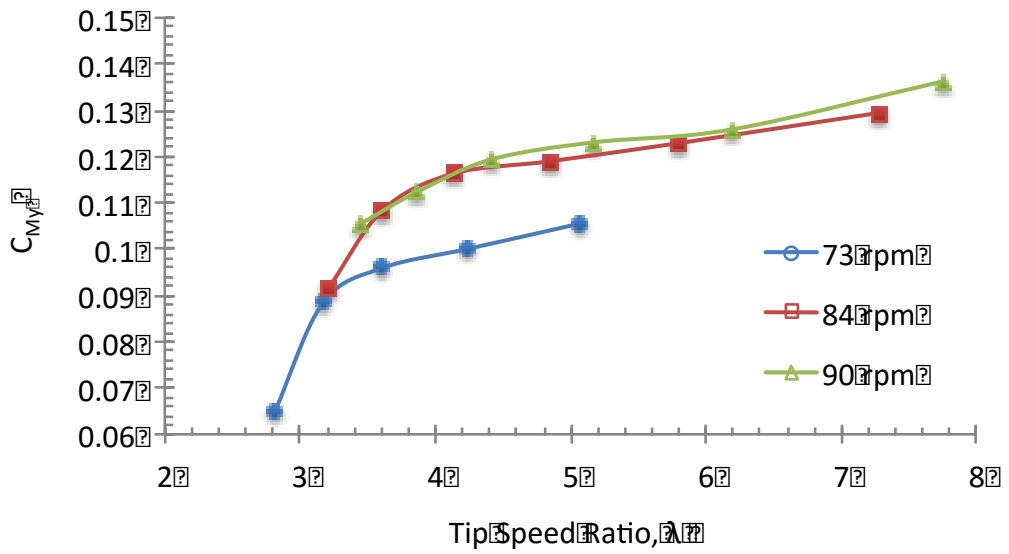


Figure 6-4 Out-of-plane bending moment coefficients as a function of tip-speed ratio for steady inflow case

## 6.2 Investigation of Blade Stall

One of the advantages of using CFD is its ability to reveal the complex flow field characteristics. In order to analyze in more detail of the wall-bounded flow field, the simulated wall shear stress on the suction side is visualized as limiting streamlines in Figure 6-5 for the rotational speed of 73 rpm.

It can be observed that at  $\lambda = 5.08$  as shown in Figure 6-5 (e), the direction of the flow near blade suction surface is almost parallel to the chord-wise direction, which means most of the blade is covered by attached flows. As the flow speed increases, it can be seen from Figure 6-5 (d) that some streamlines from  $r/R=0.2$  onward have started to deviate from the leading edge to trailing edge by turning from about  $45^\circ$  to  $135^\circ$  and back to  $45^\circ$  till  $r/R=0.5$ . The location of turning which indicated the flow separation, in Figure 6-5 (c) started from about the trailing edge to the upstream of about half of the blade in the figure. It can also be observed in Figure 6-5 (b) that the blade is almost dominated by full span-wise flow except for small chord-wise flows appearing at the tip locations. For  $\lambda = 2.82$  as shown in Figure 6-5 (a), almost the whole blade is covered by span-wise flow, which means deep-stall occurs and strong flow separation happens. The flow remains smoothly attached to the blade surface at larger radial position i.e. from  $r/R=0.6$  to 1 and  $r/R=0.5$  to 1 at  $\lambda = 2.82$  and  $\lambda = 3.15$  as shown in Figures 6-5 (a) and (b) respectively. This is due to the effect of centrifugal force which pushing the separated flow radially outward. The radial motion of separated flow is expected to affect the behavior of the boundary layer and to increase the lift force (Breton, 2008). According to Lindenburg (2003), motion of separated flow gives an additional negative pressure on the blade surface that has a stabilizing effect on the boundary layer. Therefore, the radially moving separated flow reattached back to the blade at larger radial positions.

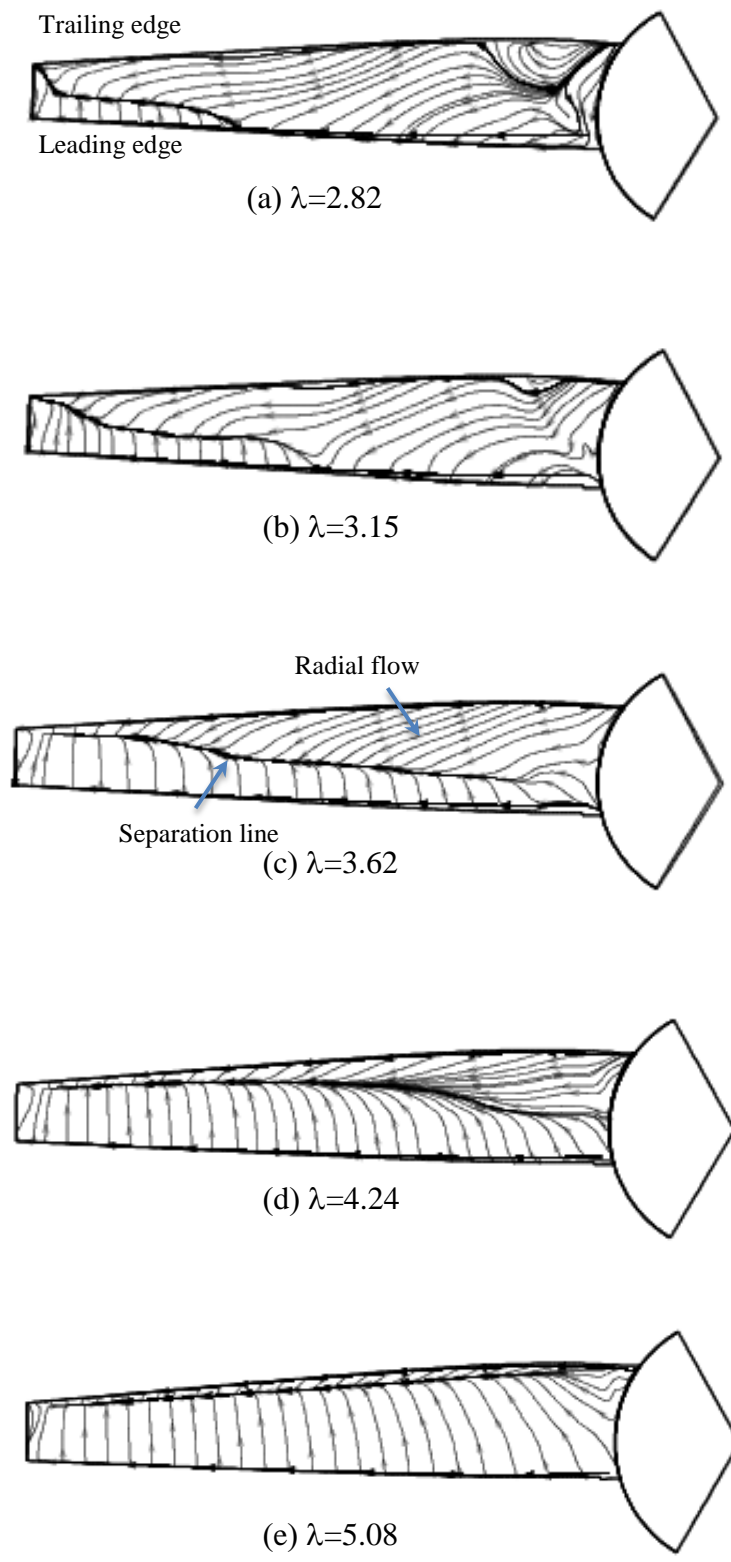


Figure 6-5 Visualization of the surface limiting streamlines for steady flow cases

## 6.3 Investigation of Scaling Effects

To observe the scaling effect of the HATT in detail, the performance of various scale models of the HATT were analyzed by the CFD techniques described in the previous chapter. The blade was scaled geometrically and Froude scaling was applied to the incident flow velocity. Table 6-1 shows the virtual scale of models and compares the Reynolds number range corresponding to the foils at 75% radial span for the different geometric scales of relevance. In the table, 100% scale means full scale of the HATT, while 5% scale is particularly the same size of the model HATT that was experimentally tested by Milne et al. (2013) and previously numerically investigated in this thesis. The chord based Reynolds number at the 0.75R foil of the 5% scale model is in the range of  $9e4$  to  $1.5e5$ . As discussed by Lissaman (1983) in his review of low Reynolds number airfoils,  $Re = 7e4$  is identified as close to transition between laminar flow and turbulent flow. With the scale increases, the chord based Reynolds number at the 0.75R foil also increases and is greater than  $1e6$ , indicates that the flow is fully turbulent. Having in mind that flow conditions of the boundary layer at different scales are different, possible scale or Reynolds numbers effects may occur when testing the turbines at a different size than in the real operating condition.

Table 6-1 Chord based Reynolds number prediction at 0.75R using geometric scaling

Scale	Radius (m)	Chord (m)	Turbine Speed (rpm)	Flow Speed (m/s)	Reynolds Number ( $\times 10^6$ )
100%	7.8	0.80	16.32	2.01-13.42	8.11-13.31
75%	5.85	0.60	18.85	1.74-11.62	5.27-8.64
50%	3.9	0.40	23.08	1.42-9.49	2.87-4.71
25%	1.95	0.20	32.65	1.01-6.71	1.01-1.66
5%	0.39	0.04	73	0.45-3	0.09-0.15

For the calculations at different scales, the grids were adapted in order to decrease the first layer cell height. However, due to restrictions in the structured grid generation method (i.e., the limits of geometry tolerances, the requirements of

minimum orthogonality), the maximum  $y^+$  value could not be decreased to lower than 1 for cases with much higher Reynolds number. Figure 6-6 shows the  $y^+$  values distributed along the inflow direction in the full scale calculation, it is clearly that the average  $y^+$  value is 12.4 and the maximum value 50, on such occasions the scalable wall functions are then activated, as this wall function virtually displaces the grid to a  $y^+ \approx 11.225$  (transition to the log-law composite layer) irrespective of the level of refinement, thereby avoiding the erroneous modelling of the laminar sub-layer and buffer region.

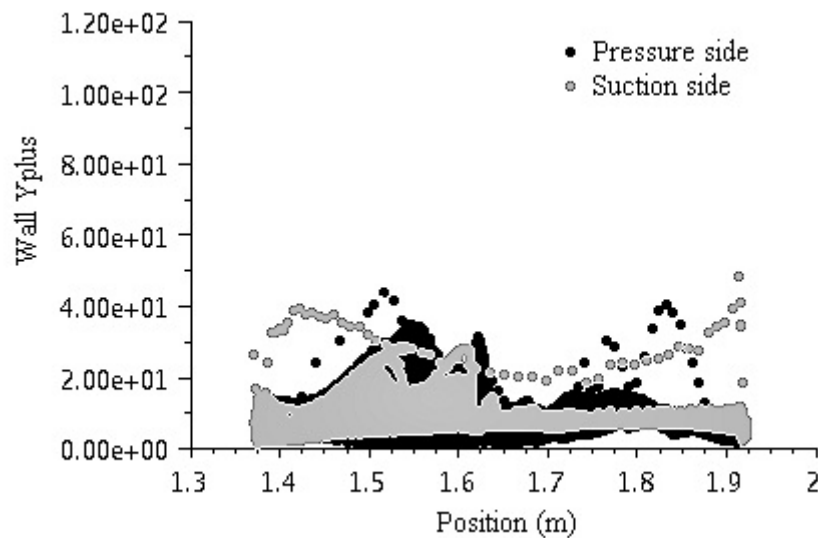


Figure 6-6 Wall  $y^+$  calculated by ANSYS Fluent from a steady inflow case of the full scale turbine

The calculations were processed for seven different tip-speed ratio conditions ranging from 0.99 to 6.63 according to the variation of flow speed. In Figures 6-7 to 6-10, the dimensionless coefficients of power  $C_p$ , thrust  $C_T$ , in-plane bending moment  $C_{Mx}$ , and out-of-plane bending moment  $C_{My}$  as a function of tip-speed ratio  $\lambda$  plotted to investigate scaling effects. The figures clearly show that these dimensionless coefficients increase with the Reynolds number. Meanwhile, as long as the Reynolds number is sufficiently high (scale of the model turbines are close to full scale), a weak dependence on Reynolds number can be detected. Similar results has been reported by Wright (1999) in his study of turbomachines, as well as



experimental investigations by Tedds et al. (2011) and numerical studies by Mason-Jones et al. (2012). In such situations, the dimensionless coefficients can be assumed to be functions of tip-speed ratio alone, data on model turbines can be used directly for estimations of full-scale turbines even in the absence of exact Reynolds number matching (which is necessary for full dynamic similarity). Moreover, the figures also demonstrated that at low tip-speed ratios, the results differences among the various scales are negligible, while as the tip-speed ratio increases, the differences become more significant, indicating scaling effects are more important when tip speed ratio is high.

The limiting streamlines at the suction side of the blades are presented in figure 6-11 for the 5% model scale and full-scale cases. For the full-scale condition at which the flow can be considered fully turbulent, the flow stays longer attached to the blade, separation occurs at low tip-speed ratios only due to heavily loaded blades and large local angles of attack.

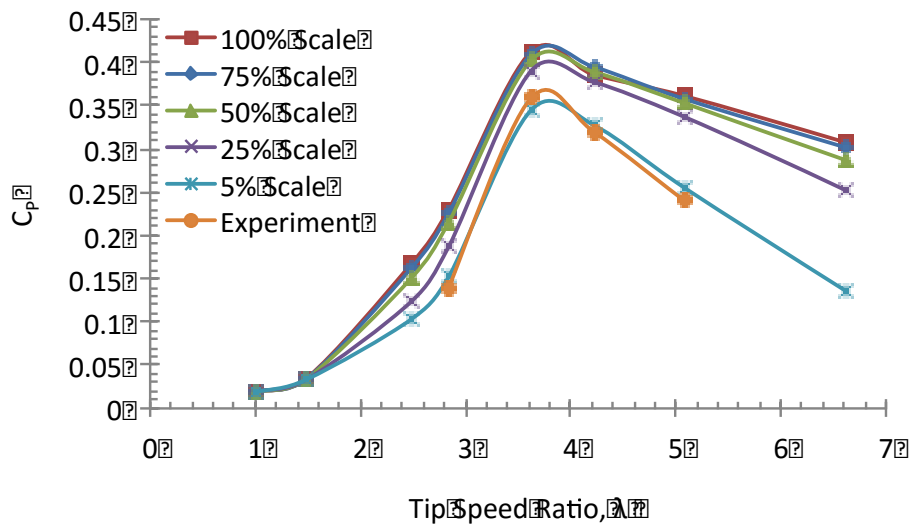


Figure 6-7 Power coefficients as a function of tip-speed ratio for different turbine scales

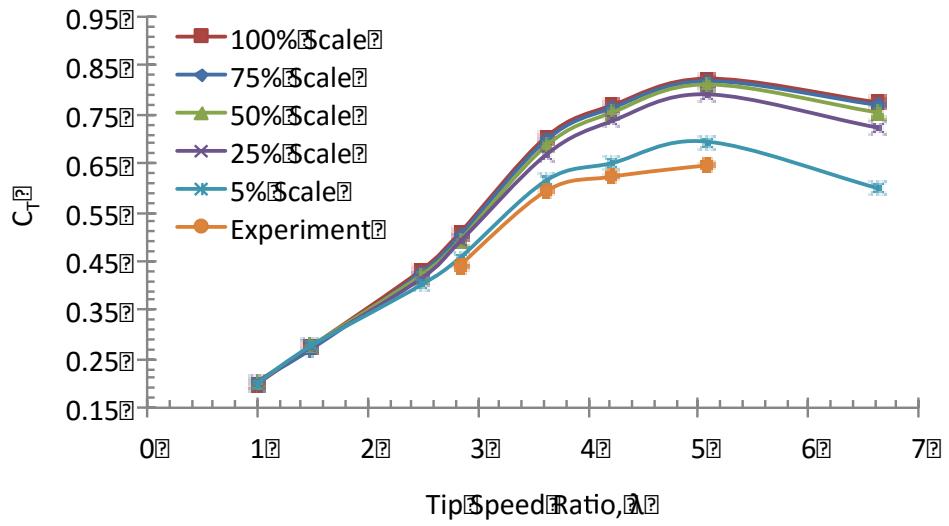


Figure 6-8 Thrust coefficients as a function of tip-speed ratio for different turbine scales

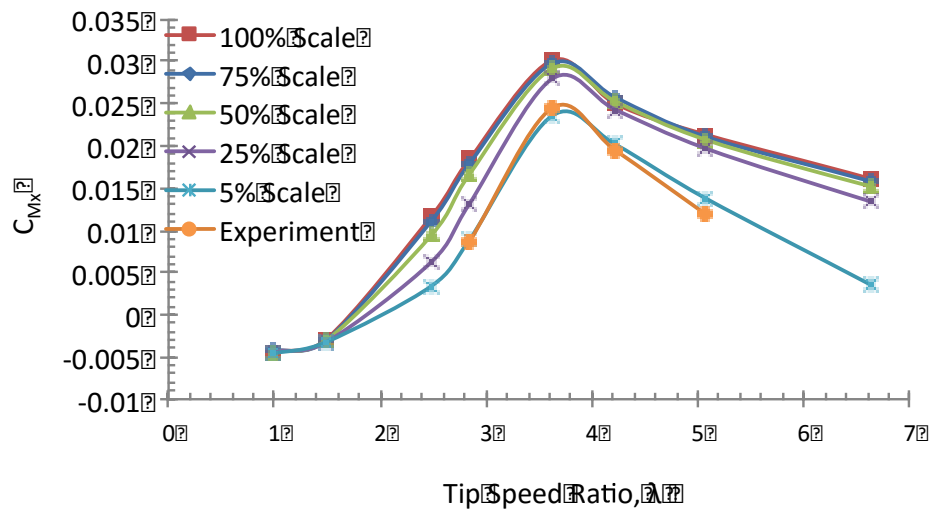


Figure 6-9 In-plane bending moment coefficients as a function of tip-speed ratio for different turbine scales

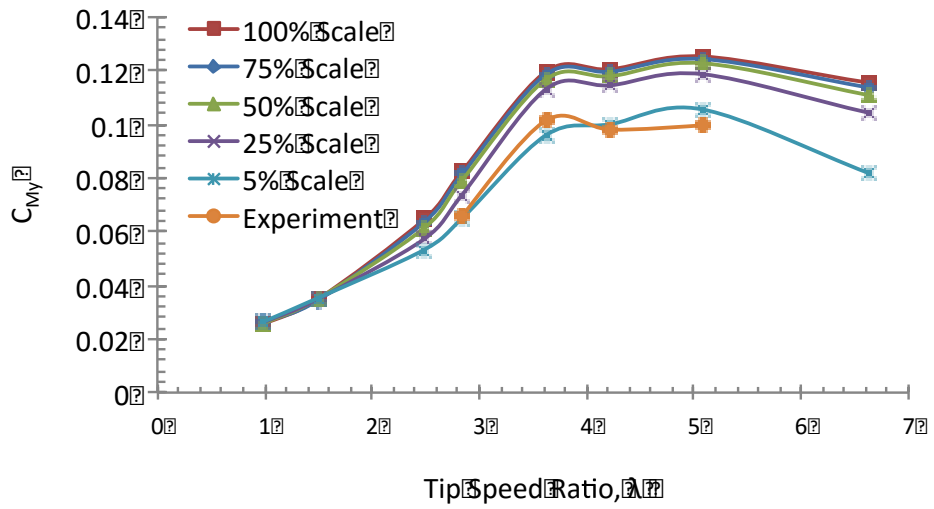


Figure 6-10 Out-of-plane bending moment coefficients as a function of tip-speed ratio for different turbine scales

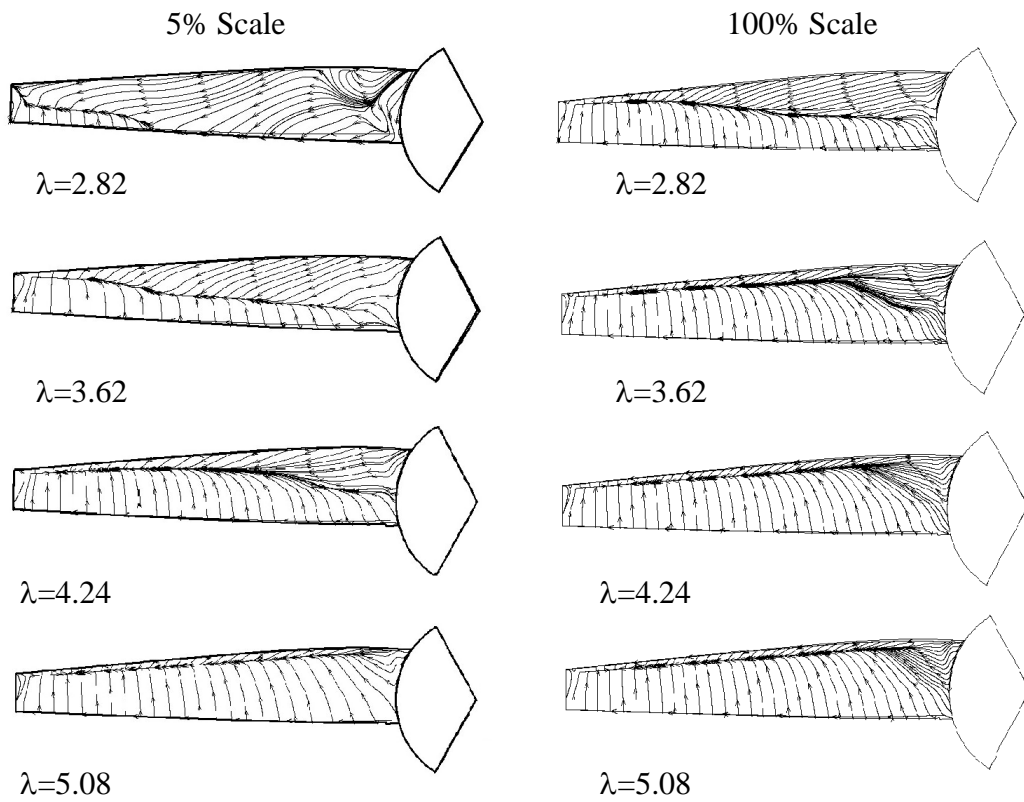


Figure 6-11 Comparison of surface limiting streamlines between 5% and full scale turbine blade at the suction side

## 6.4 Summary

Analyses in the steady velocity study are documented for a broad range of rotor speeds and flow velocities. The time-step, grid configuration and turbulence model as discussed in chapter 5 was used for the calculations. Results showed that stall effects are dominant within the low tip-speed ratios, while at higher tip-speed ratios the flow is in a turbulent wake state.

Furthermore, investigations of scaling effects on blade loads are also performed. The scalable wall functions were activated for large scale calculation, as this wall function virtually displaces the grid to a  $y^+ \approx 11.225$  (transition to the log-law composite layer) irrespective of the level of refinement, thereby avoiding the erroneous modelling of the laminar sub-layer and buffer region. It has been demonstrated that the performance characteristics of a HATT can be uniquely quantified by non-dimensional parameters and, for sufficiently high Reynolds numbers (approximately  $Re > 1e6$  for the particular geometry and flow conditions used in this study), the non-dimensional characteristics are independent of Reynolds number. However at the scale of the experiments, Reynolds number effects are significant.

# Chapter 7 Periodic Unsteady Flow Study

---

An improved characterisation of the unsteady hydrodynamic loads on tidal turbine blades is necessary to enable more reliable predictions of their fatigue life and to avoid premature failures. However, the real world unsteadiness in the onset flow of a tidal turbine is too complicated to be appropriately represented for both experimental and numerical investigations. It was discussed in section 4.1 that Milne et al. (2013) has studied the hydrodynamic blade root out-of-plane bending moment response to axial planar oscillatory forces in a towing tank. This periodic unsteady flow was proposed as an idealized representation of the unsteadiness imparted by waves and turbulence, which simplifies the problem enough to allow an insight into the unsteady flow physics, as well as without losing all connection with reality. It then allows studies to investigate further via numerical approaches.

This chapter presents a series of CFD simulation results from investigations on the hydrodynamic blade root out-of-plane bending moment response to axial planar oscillatory flow conditions. The dependency of the transient dynamic stall phenomena on the amplitude and frequency of periodic oscillations is discussed. Detailed flow analyses from the CFD studies are also performed.

## 7.1 Sensitivity to Time-Varying Velocity

Investigations on the sensitivity to both the oscillation frequency and the amplitude of oscillation velocity were conducted by varying one parameter at a time whilst maintaining the others nominally constant, to aid the inference of the underlying hydrodynamic phenomenon. As the resultant velocity varies in space and time over the rotor plane, all of the simulations were performed at mean-tip-speed ratio of  $\lambda = 3.6$ , which lies near the point of maximum power in steady flow referring to Figure 6-1. This tip speed ratio is therefore deemed to be of most interest for tidal turbine designers. Unsteady blade section hydrodynamics is typically characterized

by the reduced frequency  $\kappa$ , with values ranging from 0.01 to 0.07 likely to be experienced by a full-scale turbine at 0.75R.

### 7.1.1 Effect of Varying the Amplitude of Oscillation

Shown in Figure 7-1, 7-2, 7-3 are the velocity, acceleration and out-of-plane bending moment coefficient time histories for a variation in oscillatory frequency at  $f = 0.50$ , 0.64 and 0.89 Hz, respectively. These are cycle median-averaged histories and plotted as a function of non-dimensional time  $\tau$  ( $\tau = t/T$ ). Comparisons are made using both the experimental data and quasi-steady predictions. For these cases the current number is fixed at  $\mu = 0.2$ , with mean flow velocity at  $U = 0.78$  m/s, and mean rotor speed at  $n = 73$  rpm. It should be noted that the acceleration of the experimental oscillatory motion at higher frequency of  $f = 0.64$  Hz and  $f = 0.89$  Hz tend to exhibit irregularities, caused by physical limitations with the linear actuator which drives the auxiliary carriage. This kind of irregularity can be considered as one of the reasons for simulation discrepancies compared to experimental data.

Flow separation and dynamic stall are presented for the oscillatory simulations at mean tip-speed ratio of  $\lambda = 3.6$  here. All of the simulation results can successfully capture the characteristic of the three key stages (highlighted as 1-3 in Figure 7-1, 7-2 and 7-3) during dynamic stall, as discussed in the grid refinement test. At the beginning of flow separation, the out-of-plane bending moment coefficient  $C_{My}$  agree with quasi-steady predictions and experimental data well, highlighting that the unsteady contribution is much smaller compared to that due to full separated flow. At stage 1, the simulation result of  $C_{My}$  can be observed to exceed the point of stall observed for steady flow, but with a relatively smaller value compared to the experimental result. A delay in the onset of flow separation can also be observed in the simulation result, which may be caused by the induced camber, the influence of the shed wake and the unsteady boundary layer response, as discussed by Leishman (2006). The point of full separation at stage 2 is well captured in each of the simulation cases at the same non-dimensional timestamp as shown in the

experimental result. This stage occurs after the flow separation point has shifted from the trailing edge to the leading edge. Although the magnitude of the simulated  $C_{My}$  is a little smaller than the experimental data, it can also be observed to be significantly greater than that for steady stall, and being approximately 10% greater for the highest frequency, indicating that unsteadiness significantly increases the blade load. All of the CFD results simulated the onset of flow reattachment in advance compared to experimental data in stage 3, and showing under-prediction of  $C_{My}$  compared to experimental data and quasi-steady prediction in this stage. For the highest frequency case, the reattachment occurs near the point of minimum velocity, suggesting the flow separation can be present for a significant portion of the load cycle.

The under-prediction of blade load during flow separation in 3-D simulation is also mentioned with similar performance in the 2-D dynamic stall simulation of pitching NACA0012 airfoil in chapter 5, where the stall point is under predicted by CFD simulations compared to experimental data. Another similarity between the 3-D and 2-D CFD performance is that, the 3-D CFD results simulated the onset of flow reattachment in advance compared to experimental data, while it is also observed in the 2-D simulation that the predicted lift stall seems occur earlier than the experimental results and the lift force in the down-stroke phase seems fluctuating compared with experimental data. Such inaccurate predictions in both 3-D and 2-D CFD simulations are likely due to the complex separated flow structures and wake properties, where the vortex rolling, shedding and interaction with the structure are hard to be accurately captured by the turbulence models. Despite all these, the simulation results can still be considered as good predictors of the blade load and dynamic stall phenomena, and provide a useful insight into assessing the effect of unsteadiness.

Investigations from the velocity, acceleration and out-of-plane bending moment coefficient time histories also qualitatively implied the contribution from the blade load out of phase with velocity. For all the frequencies analyzed, the dynamic bending moment is observed to lead the velocity during full flow separation. The instantaneous phases can also be found to be frequency dependent. For the two

lowest frequency cases, the dynamic bending moment is observed to lead the velocity when the flow is attached. As the frequency is increased, the relative magnitude of the load in phase with acceleration significantly reduces and for the highest frequency case a lag can be observed when the flow is attached. It is postulated that this lag signifies a dominance of shed wake circulation over unsteadiness due to true added mass and the trailed wake associated with dynamic inflow, both of which imply a lead over the velocity (Milne, 2013).

Figure 7-4 comprises the simulated out-of-plane bending moment time histories for the variation in oscillatory frequency at  $f = 0.50, 0.64$  and  $0.89$  Hz. It can be observed that an increase in oscillatory frequency delays the movement of the separation point, and subsequently the point in the cycle at which full separation occurs. An increase in frequency can also be observed to delay the onset of flow reattachment. The magnitude of out-of-plane bending moment  $C_{My}$  seems increasing with oscillatory frequency when the flow is in the separation condition.

Comparison of the simulated hysteresis loops for the aforementioned cases is shown in Figure 7-5. The hysteresis loops are achieved by plotting the bending moment as a function of tip-speed ratio, which clearly demonstrate the complex time dependent nature of flow separation with significant variations in the instantaneous phase. The phase lag for the highest frequency case can easily be observed by the hysteresis loops. The difference between the magnitudes of  $C_{My}$  at the same tip-speed ratio signifies the extent of flow unsteadiness, the higher the oscillatory frequency, the more significant of the unsteady flow affect the blade load.



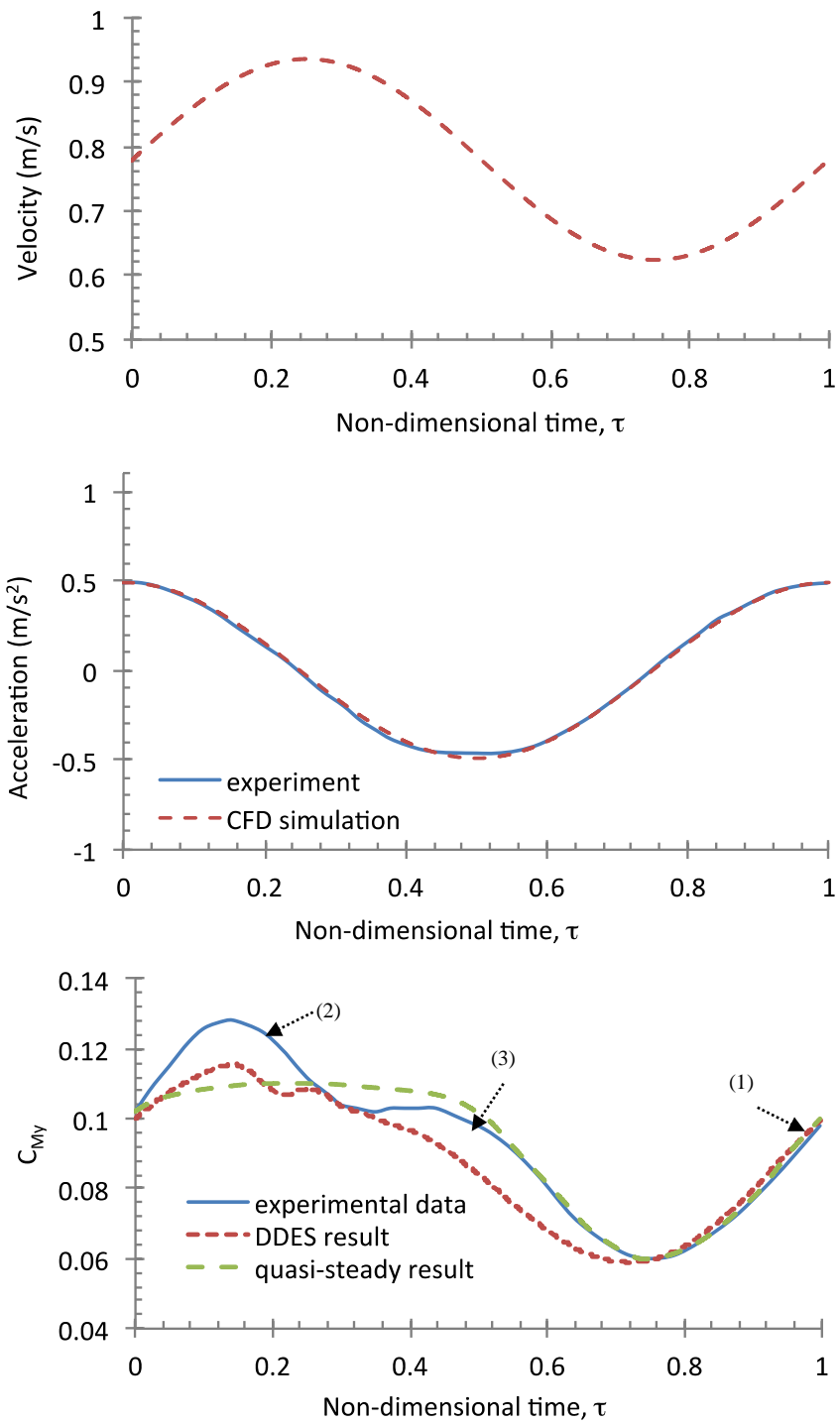


Figure 7-1 Time histories of the velocity, acceleration, and out-of-plane bending moment coefficient ( $\lambda = 3.6$ ,  $n = 73$  rpm,  $U = 0.78$  m/s,  $f = 0.5$  Hz,  $\mu = 0.2$ )

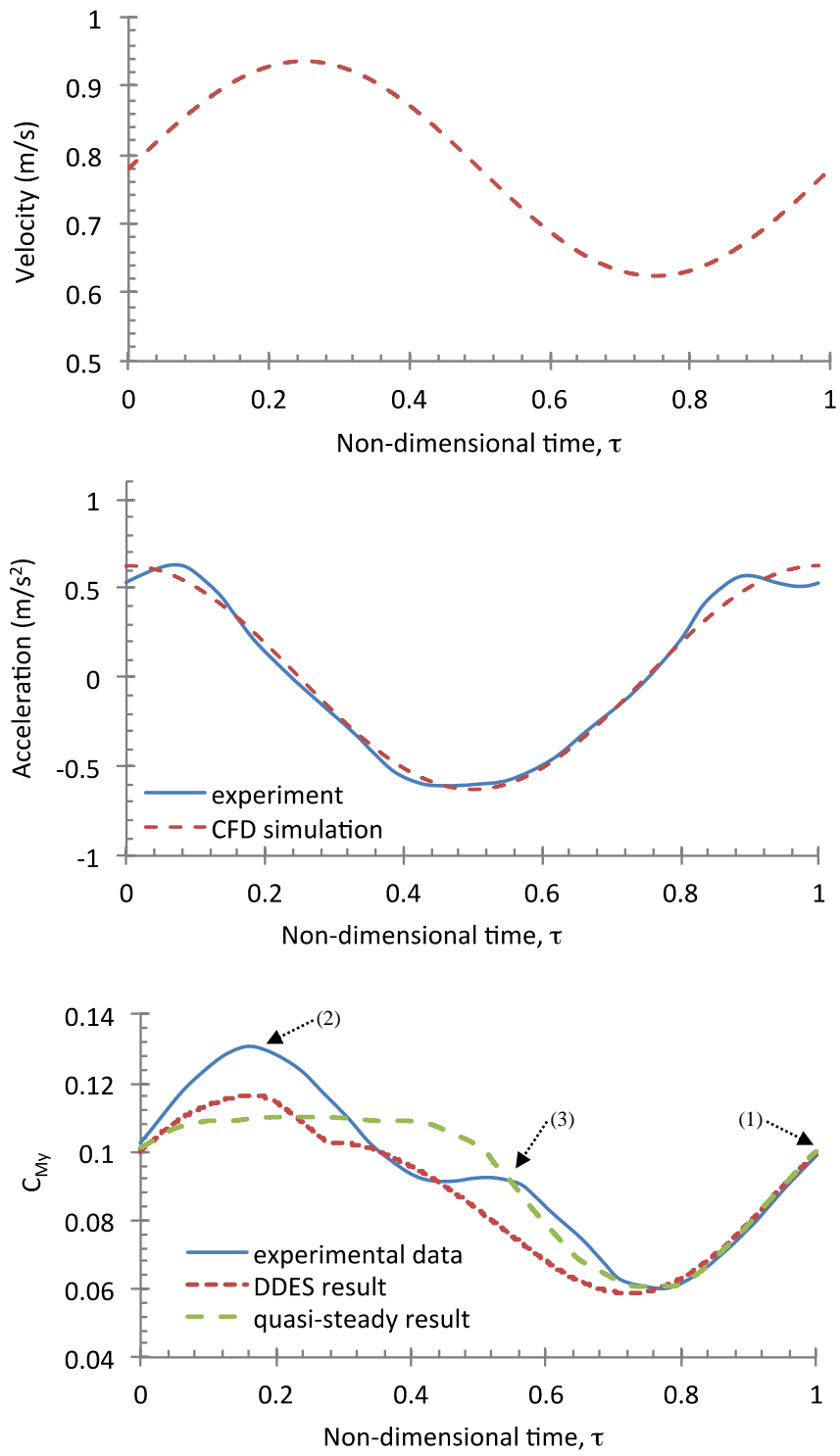


Figure 7-2 Time histories of the velocity, acceleration, and out-of-plane bending moment coefficient ( $\lambda = 3.6$ ,  $n = 73$  rpm,  $U = 0.78$  m/s,  $f = 0.64$  Hz,  $\mu = 0.2$ )

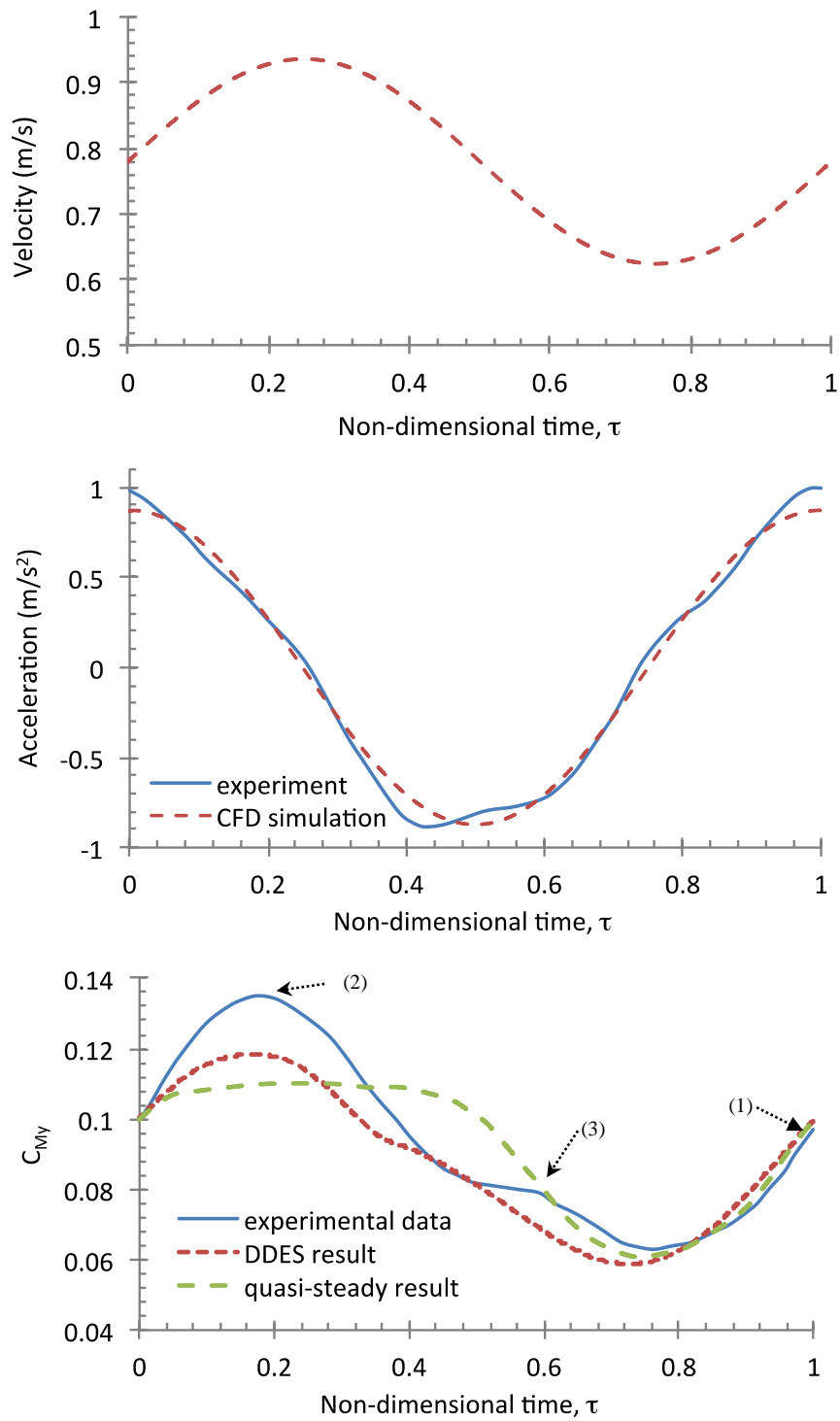


Figure 7-3 Time histories of the velocity, acceleration, and out-of-plane bending moment coefficient ( $\lambda = 3.6$ ,  $n = 73$  rpm,  $U = 0.78$  m/s,  $f = 0.89$  Hz,  $\mu = 0.2$ )

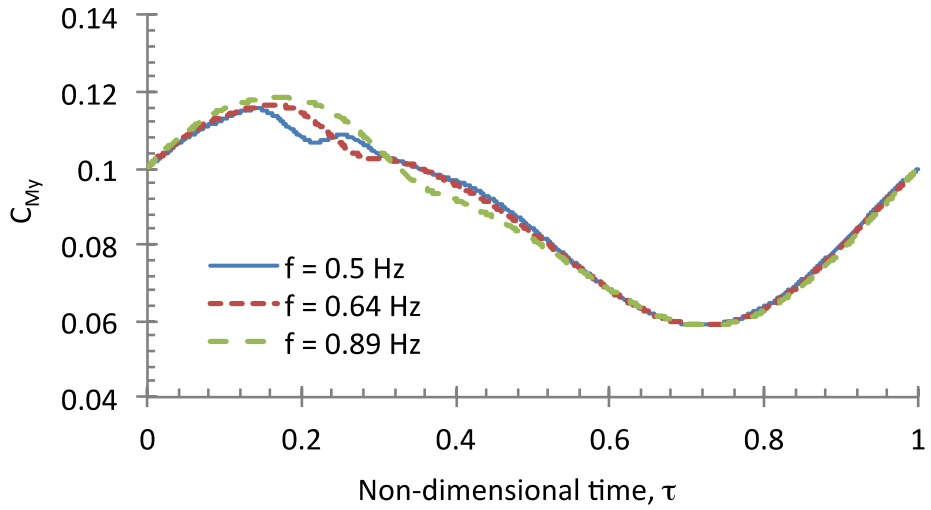


Figure 7-4 Comparison of the out-of-plane bending moment at different oscillatory frequencies

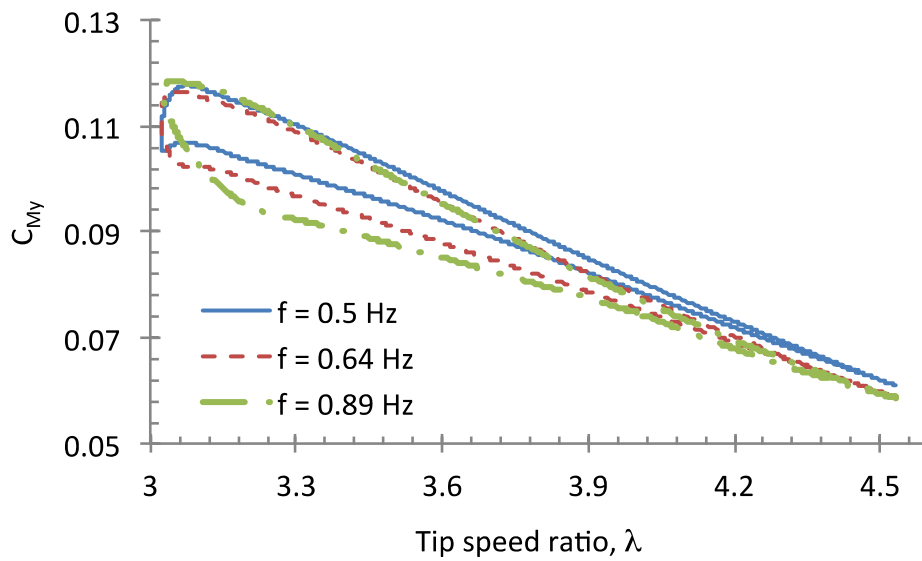


Figure 7-5 Comparison of the out-of-plane bending moment coefficients as a function of instantaneous tip-speed ratio at different oscillatory frequencies

## 7.1.2 Effect of Varying the Oscillatory Amplitude

The sensitivity of the out-of-plane bending moment to velocity amplitude is studied in this section. Figure 7-6, 7-7 and 7-8 shows the velocity, acceleration and out-of-plane bending moment coefficient time histories for a variation in current number at  $\mu = 0.1, 0.2$  and  $0.3$ , respectively. For these cases the oscillatory frequency is fixed at  $f = 0.5$ , with mean flow velocity at  $U = 0.89$  m/s, and mean rotor speed at  $n = 84$  rpm. As discussed in relation to the oscillatory frequency variation cases, the acceleration of the experimental oscillatory motion here at all the current number cases tend to exhibit irregularities, which induces part of the simulation errors compared to experimental data.

Although all the simulation results demonstrate under-prediction of  $C_{My}$  compared to quasi-steady prediction and experimental data, they all successfully capture the characteristic of the three key stages during dynamic stall. For the smallest current number case, the magnitude of  $C_{My}$  is very close between the experimental data and quasi-steady prediction, indicating that significant flow separation is not occurring at low velocity amplitude. This may be a reason that the CFD result at  $\mu = 0.1$  do not obviously exhibit a flow reattachment stage. The CFD results also simulated the onset of flow reattachment in advance compared to experimental data at higher current number of  $\mu = 0.2$  and  $0.3$ . A delay of full separation is observed for the simulation results of the two larger current number cases compare to the experimental data and quasi-steady prediction.

For all the current numbers analyzed, the dynamic bending moment is observed to lead the velocity during the complete oscillation cycle. By comparing the simulated out-of-plane bending moment time histories at different current numbers as shown in Figure 7-9, it is observed that the magnitude of out-of-plane bending moment  $C_{My}$  seems increasing with velocity amplitude when the flow is in the separation condition, and decreasing with velocity amplitude when the flow is attached.

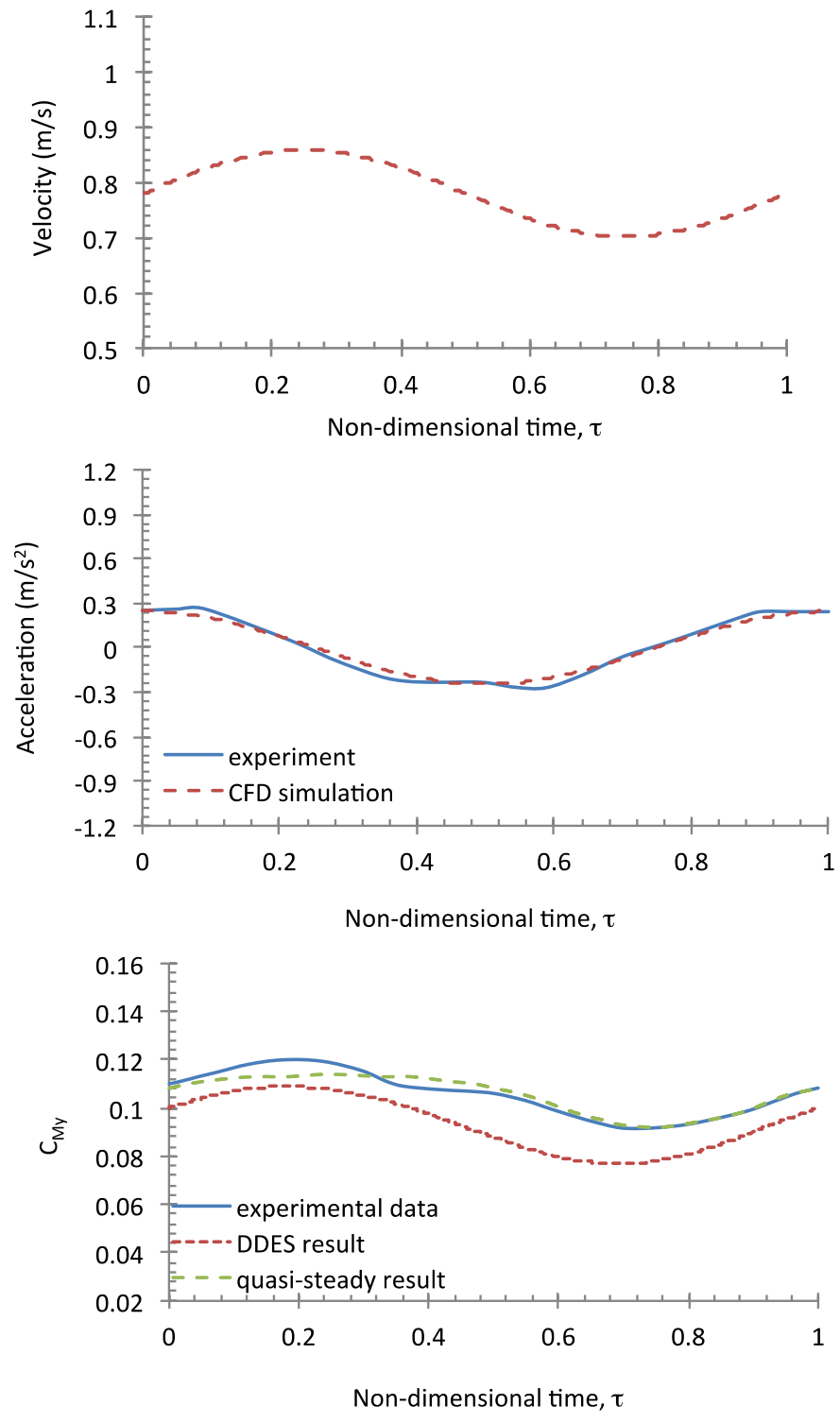


Figure 7-6 Time histories of the velocity, acceleration, and out-of-plane bending moment coefficient ( $\lambda = 3.6$ ,  $n = 84$  rpm,  $U = 0.89$  m/s,  $f = 0.5$  Hz,  $\mu = 0.1$ )

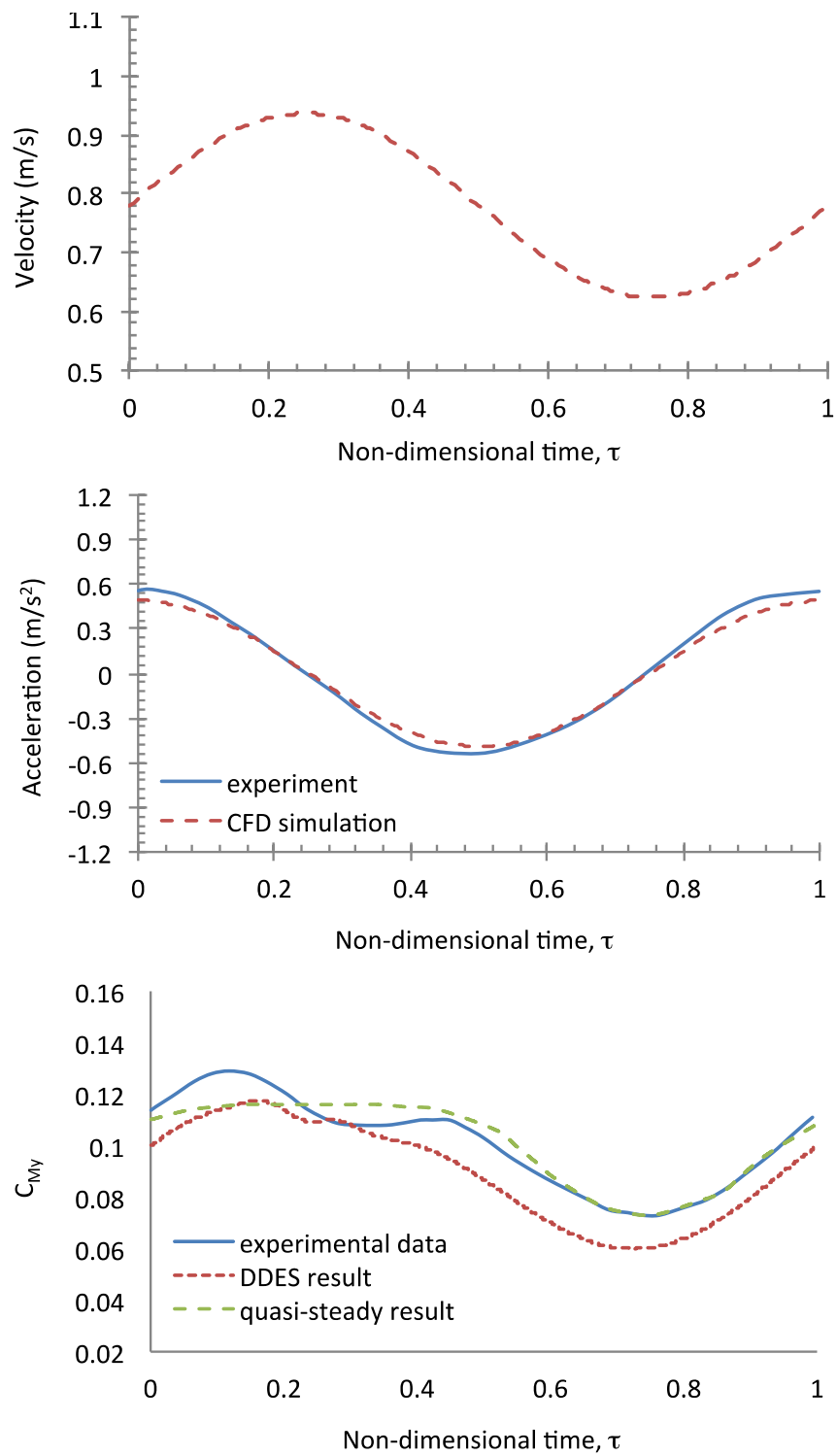


Figure 7-7 Time histories of the velocity, acceleration, and out-of-plane bending moment coefficient ( $\lambda = 3.6$ ,  $n = 84$  rpm,  $U = 0.89$  m/s,  $f = 0.5$  Hz,  $\mu = 0.2$ )

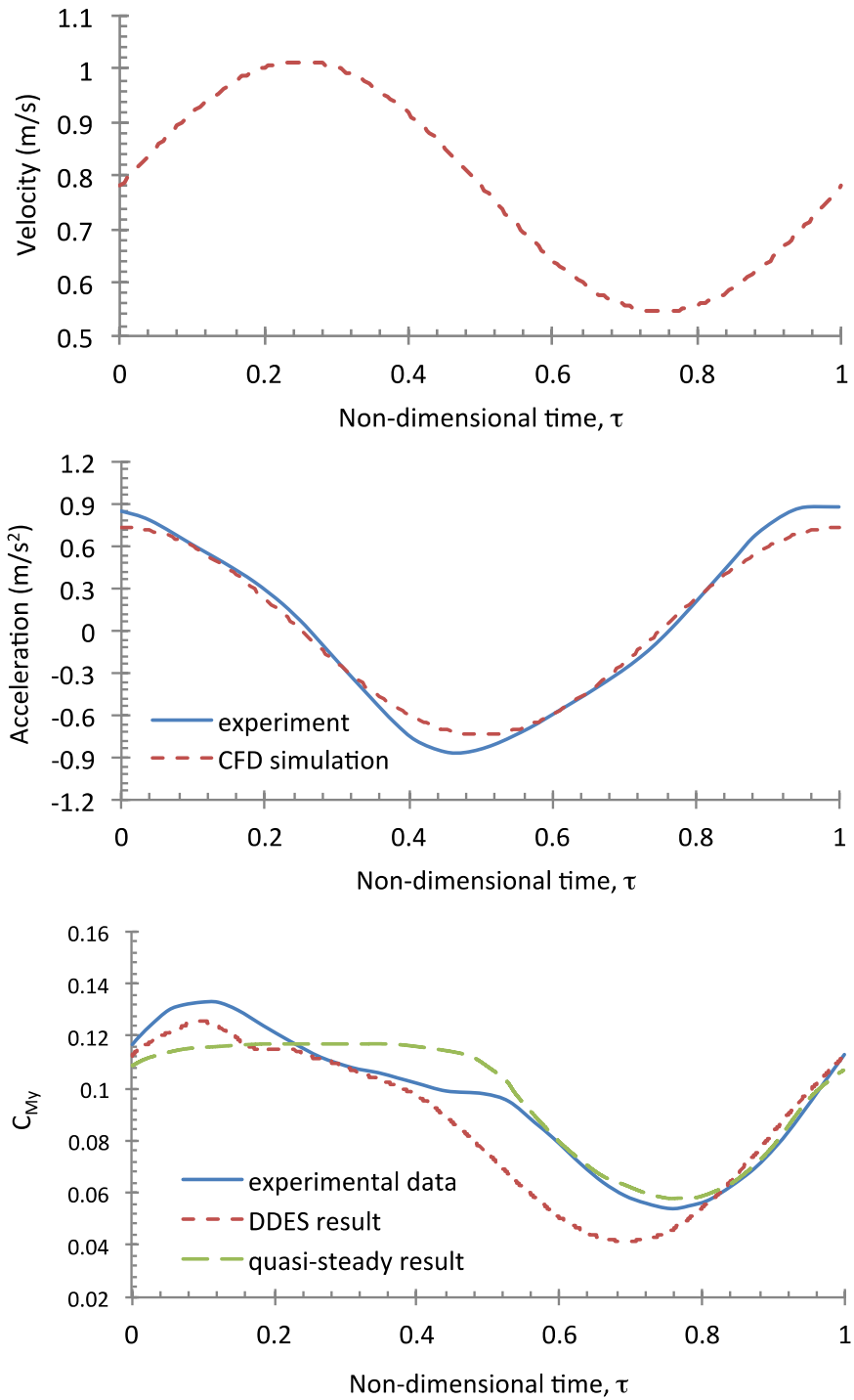


Figure 7-8 Time histories of the velocity, acceleration, and out-of-plane bending moment coefficient ( $\lambda = 3.6$ ,  $n = 84$  rpm,  $U = 0.89$  m/s,  $f = 0.5$  Hz,  $\mu = 0.3$ )



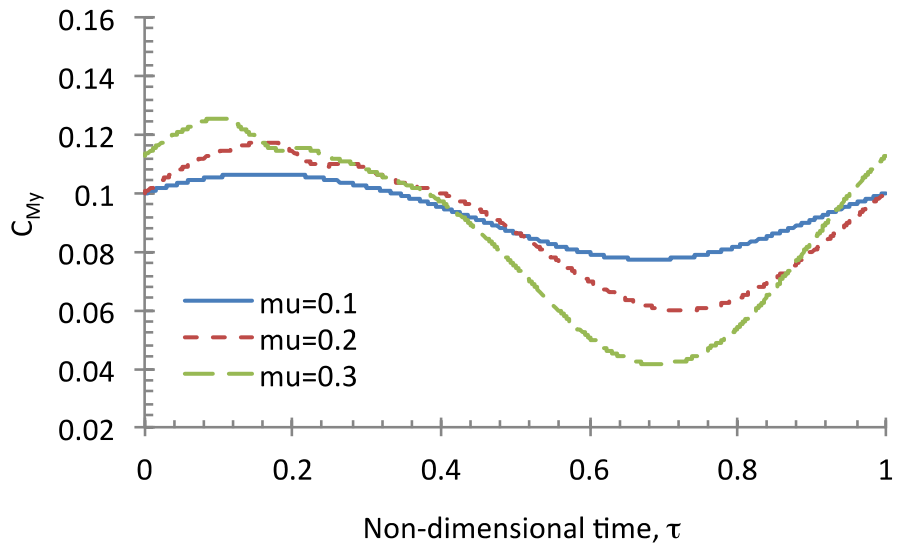


Figure 7-9 Comparison of the out-of-plane bending moment at different current numbers

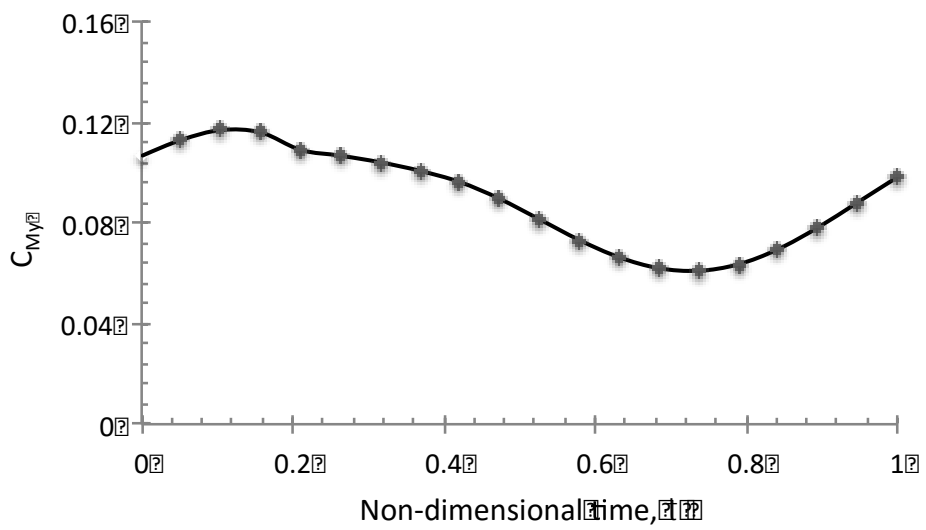


Figure 7-10 The selected flow visualization points for the case of  $f = 0.5$ ,  $\lambda = 3.6$ ,  $\mu = 0.2$ ,  $U = 0.78$  m/s,  $n = 73$  rpm

## 7.2 Dynamic Stall Characteristics Investigation

Dynamic stall process achieved from the simulation results is analyzed using various approaches in this section. The result of the case as stated in the grid refinement test using the DDES model and fine structured grid is selected here for the flow visualization study. The points selected in one oscillation cycle are shown in Figure 7-10. The commercial software TECPLOT is used to collect data from the ANSYS Fluent output and provides visual information of the flow field to support the understanding of relationship between blade load and dynamic stall.

### 7.2.1 Dynamic Stall Near Wall

Figure 7-11 shows the limiting streamlines at each timestamp during one oscillating cycle, which is achieved by calculating the wall shear stress in different Cartesian coordinates. Detailed information of the wall-bounded flow field can be revealed clearly through checking the direction of flow.

When the flow is attached to the blade, the direction of the flow near blade suction surface is almost parallel to the chord-wise direction. Flow separation is observed by the growth of span-wise flow. When almost the whole blade is fully covered by span-wise flow, deep-stall and strong flow separation happens. With the changing of angle of attack the flow will recover smoothly attached to the blade surface again which is recognized as flow reattachment.

It can be seen from Figure 7-11 that at  $\tau = 0.26, 0.31$  and  $0.35$ , flow separation is dominant in the flow field and causes the maximum magnitude of out-of-plane bending moment. At about  $\tau = 0.4$ , the chord-wise flow increases, indicating the flow is begin to reattach to the blade. At  $\tau = 0.65$ , almost the whole blade is covered by chord-wise flow, meaning the flow is attached to the blade. The magnitude of  $C_{My}$  is proved to be agreeing with the quasi-steady prediction when the flow is attached as shown in Figure 7-1.

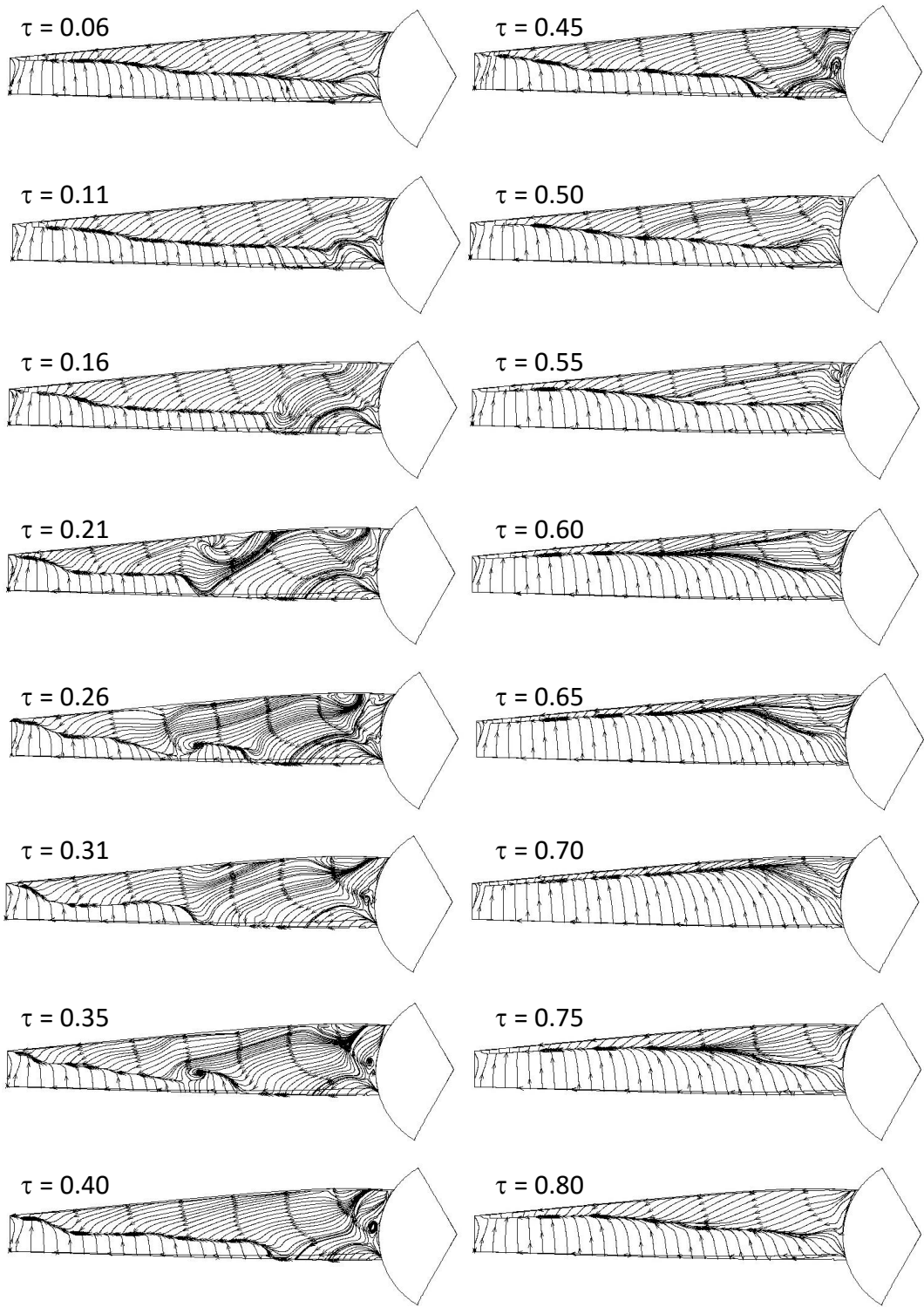


Figure 7-11 Visualization of the limiting streamlines during one oscillating cycle

## 7.2.2 Vortex Structure

The Q-criterion is a scalar used to visualize 2-D or 3-D turbulent fields (Hunt et al, 1988). It is sometimes preferred over the contours of vorticity components or the pressure field. When large pressure gradients are present in the flow local low-pressure areas (e.g. due to the presence of a vortex) may be difficult to see. Similarly the use of the vorticity to visualize the structures in the flow is not always a good idea. For instance, in a boundary layer flow (or a mixing layer) we expect to see occurrences of vorticity in the spanwise direction. But since the velocity gradient in the y-direction is large near the wall (boundary layer) and in the mixing region (mixing layer), any vorticity due to vortex motion will be overshadowed.

To help solve this problem the Q-criterion has been introduced and is defined by:

$$Q = \frac{1}{2} (\|\Omega\|^2 - \|S\|^2) \quad (7.1)$$

Where  $\|\cdot\|$  is the Euclidean (or Frobenius) matrix norm.  $\Omega$  and  $S$  are the symmetric and antisymmetric part of the velocity derivative tensor respectively.

When the Q-criterion is positive, it represents the rotation is dominant and region determines a vortex tube. Note that the local vortex refinement is made using cells with high Q-criterion values, higher than a certain positive values chosen by the user.

Figure 7-12 shows the iso-surfaces of Q-criterion as a means to depict the differing flow environments that arose from the presence of the rotating turbine at an instantaneous time step. For all of the simulation results, the iso-surface of Q-criterion indicates two turbulent structures: the vortices structures originating over the blades and spiral-like vortices tubes generated by the rotating blade tips. From the former one, we can clearly see the flow separation progress at each instantaneous time step.

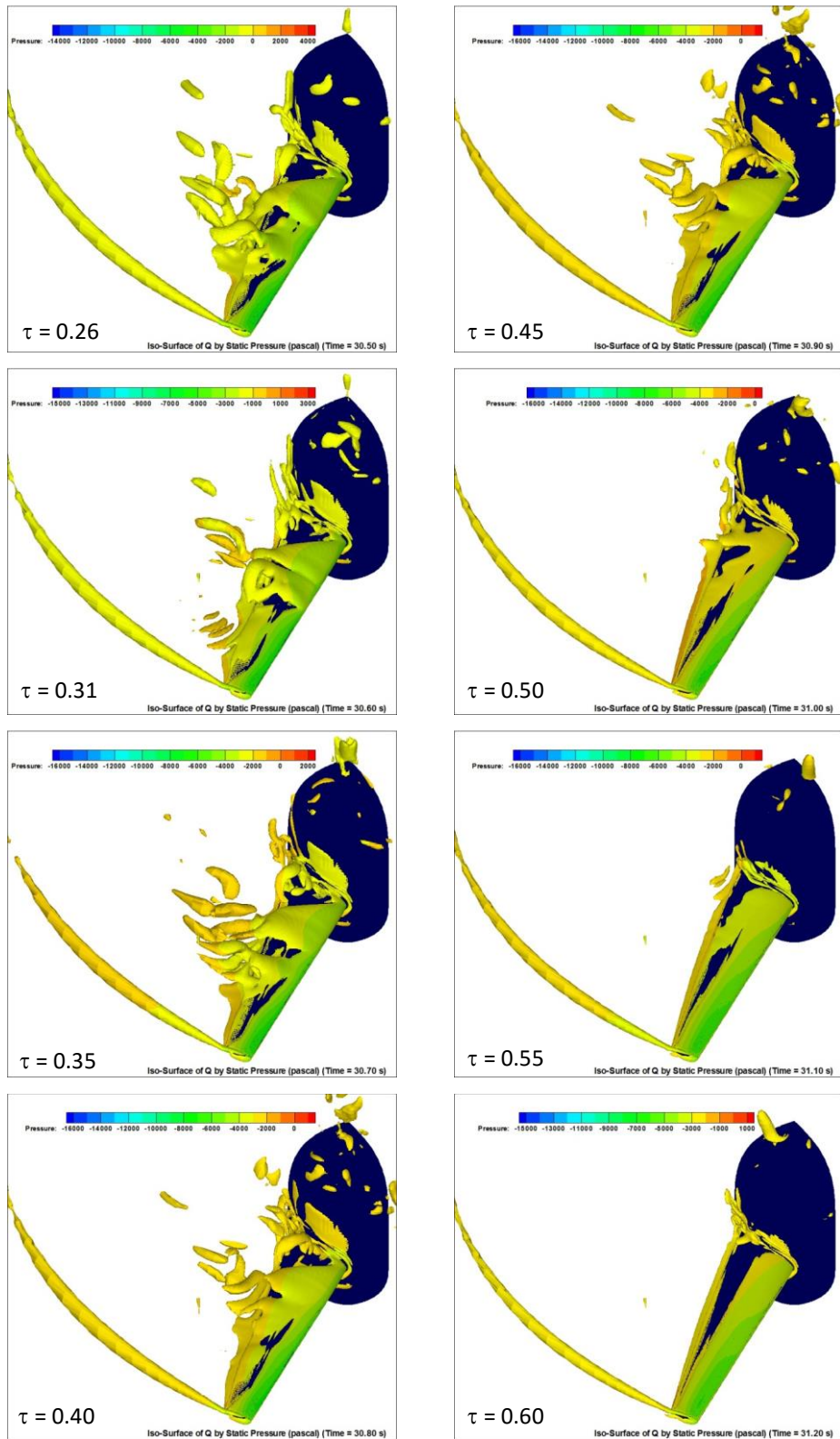


Figure 7-12 Iso-surface of Q-criterion during one oscillating cycle

At  $\tau=0.26$  where the full separation occurs, the vortices move away from the blade surface especially at the trailing edge. With increasing of the time during one oscillating cycle, the vortices appear to reattach to the blade surface gradually from the leading edge to trailing edge, at  $\tau=0.26$  the vortices are almost fully attached to the blade surface.

## 7.3 Summary

In this chapter, the CFD simulation results of the hydrodynamic blade root out-of-plane bending moment  $C_{My}$  response to axial planar oscillatory motion are validated by experiment of Milne (2013). Although the magnitude of the simulated  $C_{My}$  is a little smaller than the experimental data, and the simulated onset of flow reattachment is in advance compared to experiments, the simulation results are considered acceptable by well captured all the flow features that may occur during turbine operation, as well as provide a useful insight into assessing the effect of unsteadiness.

The transient dynamic stall phenomena are found to be dependant to the amplitude and frequency of periodic oscillations. The magnitude of the unsteady hydrodynamic contribution is found to be relatively small compared to the loads measured in steady flow at the beginning of flow separation. For attached flow a phase lead is observed at low frequencies, and for which it is postulated that the dynamic inflow effects associated with circulation in the trailed wake dominates the shed wake circulation, and added mass. At higher frequencies the unsteady loads in phase with acceleration are, however, observed to be comparatively much smaller. For all the current numbers analyzed, the dynamic bending moment is observed to lead the velocity during the complete oscillation cycle.

Flow visualization of limiting streamlines and iso-surface of Q-criterion are also performed to illustrate the effect of dynamic stall on the blade load. It was obviously

observed that the blade load time histories are consistent with the dynamic stall progress.





# Chapter 8 Conclusions and Future Work

---

Based on the current work, the aims and objectives of the research project have been achieved. The significant findings are summarized below.

## 8.1 Conclusions

A number of state-of-the-art reviews have been made in the area of modelling HATT unsteady blade loads. The BEM approach was not used in the current study due to its inaccuracy in modelling complicated flow physics. Although previous experimental and numerical studies of unsteady blade loading are very rare, they gave a general understanding on hydrodynamic performance of HATT and CFD turbulence modelling, which was enhanced by further discussions of relevant theory involves the hydrodynamic blade loads and the CFD solver.

The dynamic stall phenomenon is an important reason for the unsteady hydrodynamic loading on turbine blades. In this thesis we pay special attention in simulating and analyzing this phenomenon. A 2-D deep dynamic stall case was firstly studied to understand this complex phenomenon and to validate the numerical method and the choice of turbulence models. Both the URANS and the DDES turbulence modelling approaches were employed. The URANS was coupled with two advanced turbulence models, namely the SST  $k - \omega$  model and the Transition SST model, and the DDES was coupled with the SST  $k - \omega$  model. Computational results show that all of these turbulence models were capable of reproducing important hydrodynamic characteristics, such as the hysteresis loops of blade load coefficients. The SST  $k - \omega$  based DDES approach does not show much improvement in 2-D application. Experience from 2-D dynamic stall analysis also benefits the grid refining process in 3-D simulation, e.g. local grid refinement will be applied on the blade surface near the leading edge and trailing edge on the suction side for high fidelity turbine performance prediction.

3-D computations of a rotating scale-model HATT rotor were presented for steady and periodic unsteady inflow situations, respectively, to study the steady and dynamic stall. The methodology for numerical simulation was discussed in detail. Validation investigations of grid, time-step size and turbulence models were performed to give an impression of the accuracy of the applied methodology. It is necessary to generate a fine grid capturing the near wall boundary layer, as this is essential to the accurate prediction of the forces and the separation phenomena.

Analyses in the steady velocity study are documented for a broad range of rotor speeds and flow velocities. Computational results and flow visualization via post processing software TECPLOT showed good agreement with experimental results. Results showed that stall effects are dominant within the low tip-speed ratios, while at higher tip-speed ratios the flow is in a turbulent wake state. Investigations of scaling effects on blade loads were also performed. It has been demonstrated that the performance characteristics of a HATT can be uniquely quantified by non-dimensional parameters and, for sufficiently high Reynolds numbers (approximately  $Re > 1e6$  for the particular geometry and flow conditions used in this study), the non-dimensional characteristics are independent of Reynolds number. However, for the small-scale tests used for validation here, there are clear indications of scale effects.

The periodic unsteady velocity study analysed the out-of-plane blade-root bending moment response to harmonically-varying motion in the axial direction, chosen as an idealised representation of the free-stream velocity perturbations induced by the unsteady flow. Although the magnitude of the simulated  $C_{My}$  is a little smaller than the experimental data, and the simulated onset of flow reattachment is in advance compared to experiments, the simulation results are considered acceptable by well captured all the flow features that may occur during turbine operation, as well as provide a useful insight into assessing the effect of unsteadiness. Parametric tests on oscillatory frequencies and amplitudes were carried out in order to analyse the HATT blade hydrodynamics behaviour under different flow patterns. The simulation results were considered acceptable as they captured all the flow features that may occur

during turbine operation, as well as provide a useful insight into assessing the effect of unsteadiness. The transient dynamic stall phenomena were found to be dependant to the amplitude and frequency of periodic oscillations. The magnitude of the unsteady hydrodynamic contribution is found to be relatively small compared to the loads measured in steady flow at the beginning of flow separation. For attached flow a phase lead was observed at low frequencies, and for which it is postulated that the dynamic inflow effects associated with circulation in the trailed wake dominates the shed wake circulation, and added mass. At higher frequencies the unsteady loads in phase with acceleration are, however, observed to be comparatively much smaller. For all the current numbers analyzed, the dynamic bending moment is observed to lead the velocity during the complete oscillation cycle.

In summary, the results by the present study provide designers of tidal turbines with valuable insights into the flow physics occurring around the HATT rotor blades under various flow conditions and reliable strategies for the CFD modelling of the operating HATTs, as well as an understanding of the level of complexity required in predicting the unsteady hydrodynamic blade loads. In order to eliminate the inaccuracy problem, improvements of the CFD method (computational domain, mesh, turbulence model) are required to obtain better quantitative results; the study thus demonstrated that this is a good test case for further development. The CFD method can be used for designing more advanced HATT rotors in both steady and unsteady flow conditions; it also can be used to fine tune the computationally faster lower order BEM methods for parametric design studies where experimental data is not available, particularly at the challenging rotor operating conditions involving flow separation and dynamically varying hydrodynamic behaviours.

## **8.2 Future Work**

The test cases examined in this thesis was based on an assumption that the flow was uniform and free of cavitation, and varied in axial planar oscillatory motion to be an idealized representation of the unsteadiness imparted by waves and turbulence. By operating in this way, the problem was simplified enough to allow an insight into the

unsteady flow physics, as well as without losing all connection with reality. Based on the current CFD methodology for HATT blade hydrodynamics modelling, one of the future works will be at putting the simulation under more realistic flow velocity profiles, e.g., by considering the real wave-current interaction effects and depth-wise shear effects.

On the other hand, the LES turbulence modeling approach will also be studied in the future. Although LES is more computationally expensive than CFD based on the RANS equations, it yields a detailed, time-dependent solution that contains all of the large eddies within the flow. Such simulations could be used to develop improved RANS turbulence models for tidal turbine array calculations. Furthermore, boundary conditions such as the Synthetic Eddy Method (Jarrin et al., 2006) in LES can be used to finely tune the turbulence at the inlet. This has already been implemented in wind farm CFD models to match atmospheric conditions (Creech, 2015).

# References

---

- Anderson, J. D., 1995. *Computational Fluid Dynamics: the Basics with Applications*. McGraw-Hill, Singapore.
- Bahaj, A. S., Molland, A. F., Chaplin, J. R., and Batten, W. M. J., 2007. Power and thrust measurements of marine current turbines under various hydrodynamic flow conditions in a cavitation tunnel and a towing tank. *Renewable Energy*, 32(3), 407-426.
- Bahaj, A. S., Batten, W. M. J., and McCann, G., 2007. Experimental verifications of numerical predictions for the hydrodynamic performance of horizontal axis marine current turbines. *Renewable Energy*, 32(15), 2479-2490.
- Bartrop, N., Varyani, K. S., Clelland, A., Pham, D., and Grant, X. P., 2006. Wave-current interactions in marine current turbines. *Proceedings of the Institution of Mechanical Engineers, Part M: Journal of Engineering for the Maritime Environment*, 220(4), 195-203.
- Bartrop, N., Varyani, K. S., Clelland, A., Pham, D., and Grant, X. P., 2007. Investigation into wave-current interactions in marine current turbines. *Proceedings of the Institution of Mechanical Engineers, Part A: Journal of Power and Energy*, 221(2), 233-242.
- Batten, W. M. J., Bahaj, A. S., Molland, A. F. and Chaplin J. R., 2008. The prediction of the hydrodynamic performance of marine current turbines. *Renewable Energy*, 33(5), 1085-1096.
- Batten, W. M. J., Bahaj, A. S., Molland, A. F. and Chaplin J. R., 2007. Experimentally validated numerical method for the hydrodynamic design of horizontal axis tidal turbines. *Ocean Engineering*, 34(7), 1013-1020.
- Boussinesq, J., 1878. Équilibre d'élasticité d'un sol isotrope sans pesanteur, supportant
- Bredberg, J., 2001. On two-equation eddy-viscosity models. Technical Report 01/8, Chalmers University of Technology.

- Breton, S. O., Coton, F. N., Moe, G. A., 2008. Study on rotational effects and different stall delay models using a prescribed wake vortex scheme and NREL Phase VI experiment data. *Wind Energy*, 2008, 11, 459–482.
- Broeren, A. P., and Michael, B. B., 2001. Spanwise variation in the unsteady stalling flowfields of 2-D airfoil models. *AIAA Journal*, 39(9), 1641-1651.
- Brydges, B. E., 1989. Flow Visualization of Dynamic Stall on an Oscillating Airfoil. Naval Postgraduate School, Monterey, California, Thesis.
- Burton, T., Jenkins, N., Sharpe, D., and Bossanyi, E., 2011. *Wind Energy Handbook*. Wiley.
- Carr, L. W., 1988. Progress in analysis and prediction of dynamic stall. *Journal of Aircraft*, 25(1), 6-17.
- Carr, L. W., 1995. An Assessment of the Impact of Compressibility on Dynamic Stall. AIAA Paper 95-0779.
- Carr, L. W., McAlister, K. W., and McCroskey, W. J., 1977. Analysis of the Development of Dynamic Stall Based on Oscillating Airfoil Experiment. NASA TN D-8982.
- Carta, F. O., 1979. A Comparison of the Pitching and Plunging Response of an Oscillating Airfoil. NASA CR-3172.
- Carta, F. O., 1960. Experimental Investigation of the Unsteady Aerodynamic Characteristics of an NACA 0012 Aerofoil. United Aircraft Research Laboratories Report M-1281-1.
- Catalano, P., Wang, M., Laccarino, G., Moin, P., 2003. Numerical simulation of the flow around a circular cylinder at high Reynolds numbers. *International Journal of Heat and Fluid Flow*, 24(4), 463-469.
- Chester, H., Wolowicz, J. S., Bowman, Jr., and William, P. G., 1979. Similitude Requirements and Scaling Relationships as Applied to Model Testing. NASA Technical Paper 1435.
- Chime, A. H., Malte, J. S., 2014. Hydrokinetic turbines at high blockage ratio. 2<sup>nd</sup> Marine Energy Technology Symposium (METS2014).
- Clarke, J., Connor, G., Grant, A. D., and Johnstone, C. M., 2007. Design and testing of a contra-rotating tidal current turbine. *Proceedings of the Institution of*

- Mechanical Engineers, Part A: Journal of Power and Energy, 221(2), 171-179.
- Crimi, P., 1973. Analysis of Stall Flutter of a Helicopter Rotor Blade. AIAA Paper
- Digraskar, D. A., 2010. Simulation of flow over wind turbines. University of Massachusetts Amherst.
- Fraenkel, P. L., 2007. Marine current turbines: Pioneering the development of marine kinetic energy converters. Proceedings of the Institution of Mechanical Engineers, Part A: Journal of Power and Energy, 221(2), 159-169.
- Frisch, U., 1995. Turbulence: The Legacy of A. N. Kolmogorov. Cambridge University Press.
- Fröhlich, J., Mellen, C. P., Rodi, W., Temmerman, L., and Leschziner, M. A., 2005. Highly resolved large-eddy simulation of separated flow in a channel with streamwise periodic constrictions. Journal of Fluid Mechanics, 526, 19-66.
- Gad-el-Hak, M., 2000. Flow Control: Passive, Active, and Reactive Flow Management. Cambridge University Press, London, United Kingdom.
- Galbraith, R. A. McD and Leishman, J. G. A, 1983. Micro-Computer Based Test Facility for the Investigation of the Dynamic Stall. International Conference on the 'Use of Micros in Fluid Engineering, Paper E3'.
- Galbraith, R. A. McD, Jiang, D., Green, R. B., Gracey, M. W., and Gilmour, R., 1992. Collected Data for Tests on a NACA 0015 Aerofoil with Chord length 0.275m. G. U. Aero Report: 9209, University of Glasgow.
- Galbraith, R. A. McD. 1984. A Data Acquisition System for the Investigation of Dynamic Stall. Proceedings of the 2nd International Conference on Computational Methods and Experimental Measurements.
- Galloway, P. W., 2013. Performance quantification of tidal turbines subjected to dynamic loading, University of Southampton.
- Gasch, R. and Tvele J., 2012. Wind Power Plants: Fundamentals, Design, Construction and Operation. Berlin, Heidelberg, Springer.
- Gatski, T. B., Hussaini, M. Y., and Lumley, J. L., 1996. Simulation and modeling of turbulent flows. Elsevier.

- Geissler, W., Chandrasekhara, M., Platzer, M., Carr, L., 1997. The effect of transition modelling on the prediction of compressible deep dynamic stall. 7th Asian congress of fluid mechanics.
- Gerasimov, A., 2006. Modelling Turbulence Flows with Fluent. Europe ANSYS Inc.
- Gharali, K., and Johnson, D. A., 2013. Dynamic stall simulation of a pitching airfoil under unsteady freestream velocity. *Journal of Fluids and Structures*, 42, 228-244.
- Hansen, M. O. L., Sørensen, J. N. N., and Flay, R. G. J., 2000. Effect of placing a diffuser around a wind turbine. *Wind Energy*, 3(4).
- Hansen, M. O. L., Sørensen, J. N. N., Voutsinas S., Sørensen N., Madsen H. A. and Sørensen H. A., 2006. State of the art in wind turbine aerodynamics and aeroelasticity. *Progress in Aerospace Sciences*, 42(4), 285-330.
- Harrison, M. E., 2011. The accuracy of the actuator disc-RANS approach for modelling performance and wake characteristics of a horizontal axis tidal stream turbine. University of Southampton.
- Hau, E., and Renouard H., 2006. *Wind Turbines: Fundamentals, Technologies, Application, Economics*. Springer Berlin Heidelberg.
- Holst, M. A., Dahlhaug, O. G., and Faudot, C., 2015. CFD analysis of wave-induced loads on tidal turbine blades. *IEEE Journal of Oceanic Engineering*, 40(3).
- Houghton, E.L. and Carpenter, P.W., 1993. *Aerodynamics for Engineering Students*. Fourth Edition, Edward Arnold Publisher.
- IEA (International Energy Agency), 2015. *World Energy Outlook 2015*. <https://www.iea.org/Textbase/npsum/WEO2015SUM.pdf>
- IRENA (International Renewable Energy Agency), 2014. *Ocean energy technology: Innovation, Patents, Market Status and Trends*. [http://www.irena.org/DocumentDownloads/Publications/IRENA\\_Ocean\\_Energy\\_report\\_2014.pdf](http://www.irena.org/DocumentDownloads/Publications/IRENA_Ocean_Energy_report_2014.pdf)
- Jacobs, E., and Sherman A., 1937. *Airfoil Characteristics As Affected by Variations of The Reynolds Number*. Technical report, N.A.C.A. [Report no 586].
- Jamieson, P., 2009. Beating betz-Energy extraction limits in a uniform flow field. *European Wind Energy Conference and Exhibition*, 131(3).



- JRC (Joint Research Center), 2013. JRC annual report 2013.  
[https://ec.europa.eu/jrc/sites/default/files/jrc\\_ar\\_2013.pdf](https://ec.europa.eu/jrc/sites/default/files/jrc_ar_2013.pdf)
- Kang, D. J., and Fringer, O., 2012. Energetics of barotropic and baroclinic tides in the Monterey Bay area. *J. Phys. Oceanogr.*, 42, 272–290.
- Kelecy, F. J., 2008. ANSYS Advantage. Volume II(2).
- Kolmogorov, A. N., 1941. The local structure of turbulence in incompressible viscous fluid for very large Reynolds numbers. *Proceedings of the USSR Academy of Sciences (in Russian)*, 30, 299–303.
- Kundu, P. K., and Cohen I. M., 2012. *Fluid Mechanics*. Elsevier Science & Technology.
- Lanchester, F. W., 1915. A contribution to the theory of propulsion and the screw propeller. *Journal of the American Society for Naval Engineers*, 27(2), 509-510.
- Lanzafame, R., Messina, M., 2010. Horizontal axis wind turbine working at maximum power coefficient continuously. *Renewable Energy*, 35, 301–306.
- Lartiga, C., and Crawford C., 2010. actuator disk modelling in support of tidal turbine rotor testing. 3rd International Conference on Ocean Energy.
- Lee, J. H., Park, S., Kim, D. H., Rhee, S. H., Kim, M. C., 2012. Computational methods for performance analysis of horizontal axis tidal stream turbines. *Applied Energy*, 98, 512-523.
- Lee, T., and Gerontakos, P., 2004. Investigation of flow over an oscillating airfoil. *Journal of Fluid Mechanics*, 512, 313-341.
- Leishman, J. G., 2006. *Principles of Helicopter Aerodynamics*. Cambridge University Press, chapter 9.
- Leishman, J. G., 2002. Challenges in modelling the unsteady aerodynamics of wind turbines. *Wind Energy*, 5(2-3), 85-132.
- Leishman, J. G., and Nguyen, K. Q., 1990. State-space representation of unsteady airfoil behaviour. *AIAA Journal*, 8(5), 836-844.
- Leishman, J. G., 2006. *Principles of Helicopter Aerodynamics*. Second edition, Cambridge University Press, Cambridge Aerospace.

- Leishman, J. G., 2000. Principles of Helicopter Aerodynamics. Cambridge University Press, Cambridge.
- Lindenburg, C., 2003. Investigation into rotor blade aerodynamics. ECN-C-03-025, Netherlands.
- Lissaman, P. B. S., 1983. Low-Reynolds number airfoils. Annual Review of Fluid Mechanics, 15, 223-239.
- Liu, P., and Veitch B., 2012. Design and optimization for strength and integrity of tidal turbine rotor blades. Energy, 46(1), 393-404.
- Maganga, F., Germain, G., Maganga, J., Pinon, G., Germain, E., King, E., and Rivoalen E., 2010. Experimental characterisation of flow effects on marine current turbine behaviour and on its wake properties. IET Renewable Power Generation, 4(6), 498-509.
- Manwell, J. F., McGowan, J. G., Rogers, A. L., Manwell, A. L. and McGowan, A. L. 2010. Wind Energy Explained: Theory, Design and Application. Elsevier.
- Martinat, G., Braza, M., Hoarau Y., and Harran, G., 2008. Turbulence modelling of the flow past a pitching NACA0012 airfoil at  $10^5$  and  $10^6$  Reynolds numbers. Journal of Fluids and Structures, 24(8), 1294-1303.
- Mason-Jones, A., O'Doherty, D. M., Morris, C. E., O'Doherty, T., Byrne, C. B., Prickett, P. W., Grosvenor, R. I., Owen, I., Tedds, S., and Poole, R. J., 2012. Non-dimensional scaling of tidal stream turbines. Energy, 44(1), 820-829.
- McAlister, K., Carr, L., McCroskey, W., 1978. Dynamic stall experiments on the NACA0012 airfoil. TP 1100, NASA.
- McCann, G. N., 2008. Tidal current turbine fatigue loading sensitivity to waves and turbulence-a parametric study. 7th EWTEC.
- McCroskey, W. J., 1981. The phenomenon of dynamic stall. TM 81264, NASA
- McCroskey, W. J., 1982. Unsteady Airfoils. Ann. Rev. Fluid Mech., 1., 185-311.
- McCroskey, W. J., McAlister, K. W., and Carr, L. W., 1976. Dynamic Stall Experiments on Oscillating Airfoils. AJAA Journal, 1-1(1), 57-69.
- McCroskey, W. J., and Pucci, S. L., 1980. Viscous-Inviscid Interaction on Oscillating Airfoils in Subsonic Flow. AIAA J., 20, 167.

- McCroskey, W. J. and Pucci, S. L., 1982. Viscous-inviscid interaction on oscillating airfoils in subsonic flow. *AIAA journal*, 20(2), 167-174.
- McCullough, G. B., and Gault, D. E., 1951. Examples of Three Representative Types of Airfoil-Section Stall at Low Speed. NACA Tech. Note 2502.
- Mcsherry, R., Grimwade, J., Jones, I., Mathias, S., Wells, A., Mateus, A., 2011. 3D CFD modelling of tidal turbine performance with validation against laboratory experiments. 9th European Wave and Tidal Energy Conference.
- Menter, F. R., 1994. Two-equation eddy-viscosity turbulence models for engineering applications. *AIAA journal*, 32(8), 1598-1605.
- Menter, F. R., Langtry, R., and Völker, S., 2006. Transition Modelling for General Purpose CFD Codes. *Flow, Turbulence and Combustion*, 77(1), 277-303.
- Miley, S. J., 1982. Catalog of low-Reynolds-number airfoil data for wind-turbine applications. Elsevier.
- Milne, I. A., Day, A. H., Sharma, R. N., and Flay, R. G. J., 2013. Blade loads on tidal turbines in planar oscillatory flow. *Ocean Engineering*, 60, 163-174.
- Milne, I. A., Day, A. H., Sharma, R. N., and Flay, R. G. J., 2015. Blade loading on tidal turbines for uniform unsteady flow. *Renewable Energy*, 77, 338-350.
- Myers, L., and Bahaj, A. S., 2005. Simulated electrical power potential harnessed by marine current turbine arrays in the Alderney Race. *Renewable Energy*, 30(11), 1713-1731.
- Myers, L., and Bahaj, A. S., 2006. Power output performance characteristics of a horizontal axis marine current turbine. *Renewable Energy*, 31(2), 197-208.
- Myers, L., and Bahaj, A. S., 2007. Wake studies of a 1/30th scale horizontal axis marine current turbine. *Ocean Engineering*, 34(5), 758-762.
- Ng, K. W., Lam W. H. and Ng K. C., 2013. 2002–2012: 10 Years of Research Progress in Horizontal-Axis Marine Current Turbines. *Energies*, 6(3), 1497-1526.
- Nicholls-Lee, R. F., Turnock, S. R., and Boyd, S. W., 2013. Application of bend-twist coupled blades for horizontal axis tidal turbines. *Renewable Energy*, 50, 541-550.

- Oman, R. A., Foreman K. M., and Gilbert B. L., 1977. A progress report on the diffuser augmented wind turbine. Third biennial conf. & workshop on wind energy conversion systems, WASHINGTON D.C., U.S.A., MASSAC, 2, 819-828.
- Otto, W., Rijpkema, D., and Vaz, G., 2012. Viscous-flow calculations on an axial marine current turbine, Proceedings of the International Conference on Offshore Mechanics and Arctic Engineering, 7, 369-382.
- Park, S. W., Park, S., Rhee, S. H., 2013. Performance predictions of a horizontal axis tidal stream turbine considering the effects of blade deformation. 3rd International Symposium on Marine Propulsors, Launceston.
- Pelc, R., Fujita, R. M., 2002. Renewable energy from the ocean. Marine Policy, 26(6), 471–479
- Peters, D. A, Boyd D. D., He C. J., 1989. Finite-state induced-flow model for rotors in hover and forward flight. J Am Helicopter Soc, 34, 5-17.
- Pope, S. B., 2000. Turbulent Flows, Cambridge University Press. Cambridge, U.K..
- Ragheb, M., 2008. Dynamics and structural loading in wind turbines. <http://mragheb.com/NPRE%20475%20Wind%20Power%20Systems/Dynamics%20and%20Structural%20Loading%20in%20Wind%20Turbines.pdf>
- Starzmann, R., Baldus, M., Groh, E., 2013. A Stepwise Approach Towards The Development and Full-Scale Testing of A Marine Hydrokinetic Turbine. Proceedings of the 1st Marine Energy Technology Symposium METS13, Washington, D.C.
- Reynolds, O., 1894. On the dynamical theory of incompressible viscous fluids and the determination of the criterion. Proceedings of the Royal Society of London, 56, 40-45.
- Rodi, W., Ferziger, J.H., Breuer, M., Pourquiée, M., 1997. Status of Large Eddy Simulation: Results of a Workshop. Journal of Fluids Engineering, 119(2), 248.
- Salter, S. H., 1998. Proposal for a large, vertical-axis tidal-stream generator with ring-cam hydraulics. Proc Third European Wave Energy Conference.
- Schlichting, H., Gersten, K., 2000. Boundary Layer Theory. 8th Edn, Springer.

- Schubel, P., and Crossley, R., 2012. Wind Turbine Blade Design. *Energies*, 5, 3425-3449.
- Shiple, D. E., Miller, M. S., Robinson, M. C., 1995. Dynamic Stall Occurrence on a Horizontal Axis Wind Turbine Blade. National Renewable Energy Lab, Golden, United States.
- Somers, D. M., 1997. Design and experimental results for the S814 airfoil. Subcontractor Report NREL/SRe440e6919. Pennsylvania: Airfoils Incorporated. State College.
- Spalart, P. R., 2001. Young person's guide to detached-eddy simulation grids. NASA CR-2001-211032.
- Spellman, F., Bieber, R., 2011. The science of Renewable Energy. CRC Press. International Standard Book Number-13: 978-1-4398-2503-7 (Ebook-PDF)
- Spentzos, A., Barakos, G. N., Badcock, K. J., Richards, B. E., Wernert, P., Schreck, S. and Raffel, M. 2005. Investigation of 2-D Dynamic Stall Using Computational Fluid Dynamics. *AIAA Journal* 43(5): 1023-1033.
- Sreenivasan, K., and Stolovitzky, G., 1995. Turbulent cascades. *Journal of Statistical Physics*, 78(1), 311-333.
- Sultanian, B., 2015. Fluid Mechanics: An Intermediate Approach. CRC press.
- Tedds, S. C., 2011. Experimental investigation of horizontal axis tidal stream turbines. 9th EWTEC, Southampton.
- Versteeg, H., and Malalasekera W., 2007. Introduction to Computational Fluid Dynamics. The Finite Volume Method, Prentice Hall.
- Wang, S., Ingham, D. B., Ma, L., Pourkashanian, M., and Tao, Z., 2010. Numerical investigations on dynamic stall of low Reynolds number flow around oscillating airfoils. *Computers and Fluids*, 39(9), 1529-1541.
- Wang, S., Ingham, D. B., Ma, L., Pourkashanian, M., and Tao, Z., 2012. Turbulence modeling of deep dynamic stall at relatively low Reynolds number. *Journal of Fluids and Structures*, 33, 191-209.
- Wang, S., Tao, Z., Ma, L., Ingham, D., and Pourkashanian, M., 2010. Numerical investigations on dynamic stall associated with low Reynolds number

- flows over airfoils. 2nd International Conference on Computer Engineering and Technology, 5, 308-312.
- Waters, S., Aggidis G., 2016. Tidal range technologies and state of the art in review. *Renewable and Sustainable Energy Reviews*, 59, 514-529.
- Wernert, P., Geissler, W., Raffel, M., Kompenhans, J., 1996. Experimental and numerical investigations of dynamic stall on a pitching airfoil. *AIAA Journal*, 34, 982–989.
- Whelan, J. I., 2010. A fluid dynamic study of free-surface proximity and inertia effects on tidal turbines. Imperial College London.
- Whelan, J. I., Stallard, T., 2011. Arguments for modifying the geometry of a scale model rotor. 9th European Wave and Tidal Energy Conference (EWTEC2011), Southampton.
- Wilcox, D. C., 1993. *Turbulence modeling for CFD*. DCW Industries.
- Wright, T., 1999. *Fluid Machinery: Performance, Analysis and Design*. Florida: CRC Press.
- Zahle, F., and Sørensen, N. N., 2007. On the influence of far-wake resolution on wind turbine flow simulations. *J. Phys., Conf Series* 75 012042.